RCA Review

June 1972 Volume 33 No. 2
RCARCI 33(2) 325-479 (1972)

RCA Review, published quarterly in March, June, September and December by RCA Research and Engineering, RCA Corporation, Princeton, New Jersey 08540. Entered as second class matter July 3, 1950 under the Act of March 3, 1879. Second-class postage paid at Princeton, New Jersey, and at additional mailing offices. Effective Jan. 1, 1971, subscription rates as follows: United States and Canada: one year $6.00, two years $10.50, three years $13.50; in other countries, one year $6.40, two years $11.30, three years $14.70. Single copies (except for special issues) up to five years old $3.00.

RCA Review

A technical journal published quarterly by RCA Research and Engineering in cooperation with the subsidiaries and divisions of RCA.

Contents

June 1972 Volume 33 Number 2

Noise Sources in Charge-Coupled Devices

J. E. Carnes and W. F. Kosonocky

RCA Laboratories, Princeton, N. J.

Abstract—Potential noise sources in charge-coupled devices are analyzed and their contributions to the rms fluctuation in the number of charge carriers in a signal packet are evaluated. The noise sources considered are (1) transfer loss noise, (2) background charge generation noise, (3) output amplifier noise, and (4) fast interface state trapping noise. The comparison of the relative contribution of these sources shows that for a reasonable number of transfers (> 100) fast state trapping should dominate the noise behavior of conventional interface channel CCD's.

1. Introduction

To date, most of the analytical and experimental work on charge-coupled devices (CCD's)[1] has centered around maximum achievable transfer efficiency (η), since this performance parameter is the most important in determining the practical maximum number of stages between signal refreshing. However, recent announcements of experimentally observed η values[2] of up to 99.99% at 1 MHz have demonstrated CCD practicality, confirmed transfer efficiency analyses, and, in addition, resulted in increased attention to other CCD performance characteristics such as noise, which so far has received only minimal coverage in the CCD literature.[3] The assessment of CCD

noise is important in establishing the minimum size of CCD memory elements, the noise figure of CCD analog delay lines, and the dynamic range and low-light-level sensitivity of CCD image sensors.

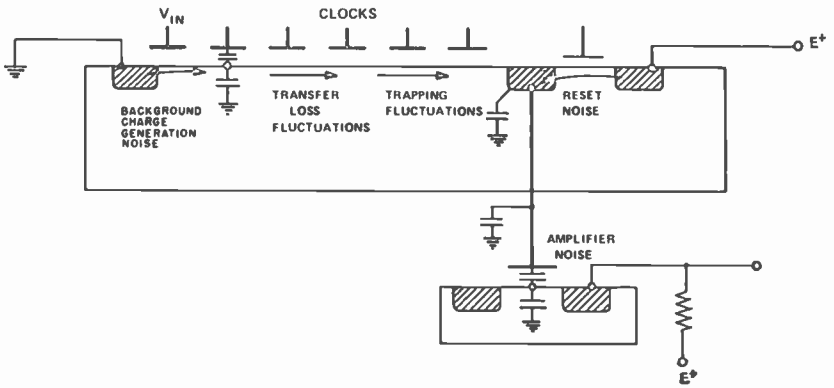

Fig. 1—Cross-sectional view of charge-coupled device showing origin of various noise sources.

This paper, which is essentially analytical in nature, discusses the various noise sources expected in typical CCD operation. Every effort has been made to use simple physical ideas, probability concepts, and noise models, and to avoid complicated mathematical procedures. Since CCD's are basically charge-packet shift registers with no gain mechanism (so that the same carriers remain essentially intact in the same packets throughout the entire transfer process), the rms fluctuation in the number of carriers in each packet has been used to quantify and compare the various noise sources. This quantity is denoted by $\overline{N}_n$, the rms fluctuation in the total number of carriers in each charge packet being transferred by the CCD.

Fig. 1 is a schematic cross-section of a CCD labeled with the various noise sources we have considered. These sources are (1) transfer loss fluctuations; (2) background charge generation noise; (3) output amplifier noise, including reset noise for floating diffusion and floating gate voltage-sensing and MOS field-effect transistor (MOSFET) noise; and (4) fast interface state noise. It is shown that the largest fluctuation will result from fast state trapping in conventional surface channel CCD's. This mechanism should limit the sensitivity of CCD image sensors and the minimum gate area and packing density of CCD digital memories.

2. CCD Noise Sources

2.1 Transfer Loss Fluctuations

For CCD's operating in the "complete" charge-transfer mode a small fraction ϵ of the charge is left behind at each transfer. If N_s is the total number of carriers in the signal packet, then on the average ϵN_s will be left behind at each transfer. There will, however, be fluctuations about this average with mean-squared value of $2\epsilon N_s$, i.e., shot noise introduced into the signal packet once upon entering and a second time upon leaving the potential well. If ϵ is independent of the amount of charge being transferred, as it is for incomplete free charge transfer and small signal fast interface state trapping losses, the fluctuations at each transfer will be independent of one another and the mean-squared fluctuations will add.

Both signal carriers and background carriers will fluctuate because of this mechanism. Thus,

$$\overline{N}_{n,\,\text{Transfer Loss}} = [2\epsilon N_g\,(N_s + N_{s,o})\,]^{1/2}, \qquad [1]$$

where ϵ is the fractional loss per gate or transfer

N_g is the number of gates or transfers

N_s is the number of signal carriers per charge packet

$N_{s,o}$ is the number of background carriers ("fat zero") per charge packet.

2.2 Background Charge Generation Noise

Background charge may either be electrically generated at the input as fat zeros to suppress fast interface state losses or it may be generated thermally or optically via bias light. In any case, this background charge will be noisy. If it is introduced thermally or optically (both processes are stochastic with Poisson-distributed arrival times), the variance in the average number of carriers in each packet will be that average number, i.e., shot noise.

$$\overline{N}_{n\,,\text{Background Charge, Thermal}} = (N_{s,o})^{1/2} \qquad [2]$$

If the device is cooled, thermal generation can be suppressed and the background charge or fat zero may be introduced electrically at the input with less than shot noise. If a MOSFET is used to introduce background charge into the first potential well once during

each cycle, then the analysis of Appendix 1 indicates that the rms fluctuation would be:

$$\overline{N}_{n,\ \text{Background Charge, Electrical}} = 400\ (C_{pf})^{1/2} \qquad [3]$$

where C_{pf} is the capacitance of the potential well in picofarads.

2.3 Output Amplifier Noise

In an amplifier whose bandwidth is limited by the RC time constant at the input, the thermal noise associated with the input resistance is the major noise source. This resistance is in parallel with the input capacitance of the amplifier, and, as shown in Appendix 1, the rms carrier fluctuation at the input is given by

$$\overline{N}_{n,\ \text{Amp}\ RC} = \frac{1}{q}\ (kTC)^{1/2} = 400\ (C_{pf})^{1/2} \qquad [4]$$

However, the above analysis applies only for the case where the bandwidth is determined by the input RC time constant. In a CCD this is not necessarily the case. In the voltage-sensing amplifier shown in Fig. 1, the voltage on the input gate is proportional to the signal charge in the floating diffusion. Since the floating diffusion is reset to a reference potential once each clock period, the bandwidth is determined by the Nyquist criterian ($\Delta B = f_c/2$) and is not RC limited. Thus, the input resistance can be arbitrarily large and the noise will be determined by the resetting of the floating diffusion.

a. *Floating Diffusion Reset Noise*

In this voltage-sensing scheme, the floating diffusion is directly connected to the gate of the output transistor, and the potential of floating diffusion controls the output current. The floating diffusion is also conncted to a fixed voltage source E_o via an MOS channel, which is periodically turned on to reset the floating diffusion to E_o. Alternately stated, the signal charge is removed from the floating diffusion once each cycle by the MOS channel. Several methods for resetting the floating diffusion are discussed in Ref. [4]. The noise introduced by this resetting will be the thermal noise of the MOS channel resistance in parallel with the floating diffusion capacitance. As shown in Appendix 1, the rms carrier fluctuation will be

$\sim 400\sqrt{C_{pf}}$, where C_{pf} is the total capacitance associated with the floating diffusion and amplifier input gate in picofarads.

$$\overline{N}_{n,\ \text{Reset Diffusion}} = 400\ (C_{pf})^{1/2}. \qquad [5]$$

b. *Floating Gate Reset Noise*

In the floating gate sensing scheme, a gate above the channel oxide can be set to a fixed potential E_o through a large resistance, or reset to E_o through an MOS transistor at a frequency less than the clock frequency. Since the capacitance between the substrate and this floating gate C_g is the series combination of the oxide capacitance C_o and depletion layer capacitance C_d, it will increase when signal charge is present. Because this gate is floating and has fixed charge, its voltage will decrease as C_g increases, i.e., when signal charge is present at the Si-SiO_2 interface. The sensitivity of the floating gate method can be comparable to that of the floating diffusion. The floating gate is connected directly to the gate of the MOSFET amplifier.

The noise introduced by this scheme will again be the thermal noise of the resistance through which the floating gate is reset. This resistance can be large enough so that the time constant RC (where C is the sum of the floating gate and amplifier gate) is large compared to the operating period of the CCD. The current through R need only be large enough to restore charge lost by leakage. Thus, while the thermal noise of the resetting resistor will be large up to frequencies of approximately $(\pi RC)^{-1}$, it will not be large in the bandwidth of interest, and appropriate filtering will eliminate it. Alternatively, if the floating gate is reset once each frame time by an MOS transistor, the reset noise will again be below the video bandpass and can be removed by filtering.

Thus, by this alternate approach to voltage sampling, the resetting noise of the output amplifier can be essentially eliminated.

c. *MOSFET Noise*

There are, however, other noise sources in a MOSFET amplifier, namely thermal channel noise[5] and $1/f$ surface noise.[6] Both these sources create fluctuations in the drain current that can be referred back to the input as fluctuations in the number of electrons on the input gate. As proposed by Klaassen and Prins,[5] this thermal noise of the channel is equivalent to an input noise resistance R_n given by

$$R_n = \frac{\alpha}{g_{mo}}, \qquad [6]$$

where g_{mo} is the transconductance of the device and α varies between ⅔ and 10 and depends upon gate and drain voltage, oxide capacitance, and substrate doping.

The other well-known source of noise in MOSFETs is the $1/f$ noise usually associated with fast interface state trapping. $1/f$ noise has a noise power spectrum proportional to $1/f$ and can be related to the thermal noise if the frequency where they are equal f' is known.

$$\overline{v_n^2}_{\text{MOSFET}} = \overline{v_n^2}_{\text{THERMAL}} \left(1 + \frac{f'}{f}\right). \qquad [7]$$

Klaassen[6] reports f' values ranging between 10^4 Hz for low current levels to 10^5 Hz at high current levels. Work at this Laboratory on low-noise silicon-gate MOSFET's has also produced cross-over frequencies of 10^4 Hz[7]. For many CCD applications, appropriate filtering of the output signal can, therefore, eliminate most $1/f$ noise, and the input-referred mean-squared thermal noise voltage of the channel will be thermal white noise:

$$\overline{v_n^2} = \frac{4kT\Delta B\alpha}{g_{mo}}. \qquad [8]$$

Thus, the rms carrier fluctuation at the input will be

$$\overline{N}_{n,\,\text{MOSFET}} = \frac{C_{\text{gate}}}{q}\,\overline{v}_n \qquad [9]$$

$$\overline{N}_{n,\,\text{MOSFET}} = 60\, C_{\text{gate}} \left[\left(\frac{\Delta B}{5\text{MHz}}\right)\left(\frac{1000\ \mu\text{mho}}{g_{mo}}\right)\right]^{1/2} \qquad [10]$$

where C_{gate} is measured in pf.

Thus for a C_{gate} value of 0.1 pf or less, the fluctuation introduced by the output amplifier MOSFET itself is anticipated to be negligible compared with other sources.

2.4 Fast Interface State Noise

Fast interface states[8] will generate noise in CCD's even in the absence of signal charge. Suppose we have a CCD that is operating either in the bias charge* or the complete transfer with fat zero mode with no signal input. On the average, the fast state occupation will either remain constant for bias charge operation or fill and empty to the same level during each period for complete transfer. On the average, then, there will be no net loss of charge into fast states. However, there will be fluctuations in the total number of carriers trapped at any instant of time. These fluctuations will be reflected in the free charge in the potential well, and hence in the output. If the mean-squared fluctuation N_t^2 in the total trapped charge per unit area is independent of the free background charge levels, as it will be for background charge levels high enough to effectively suppress fast state losses, then the mean-squared fluctuations a particular charge packet encounters at each gate as the charge packet transits through the device must add. Further, the fluctuation in the number of carriers in the charge packet will reflect the fluctuations in the trapped charge twice at each gate—once when the packet is transferred in and once when it is transferred out. As shown in Appendix 2, the N_t^2 for bias charge operation is simply kTN_{ss}; while as shown in Appendix 3, for complete transfer operation with fat zero, it is $0.7\ kTN_{ss}$.

Thus, after N_g transfers, in the case of complete transfer with fat zero, the rms fluctuations will be:

$$\overline{N}_{n,\,\mathrm{Trap}} = [1.4\,kTN_{ss}N_gA_g]^{1/2} = 670\left[\frac{N_{ss}}{10^{10}}\,\frac{N_g}{10^3}\,\frac{A_g}{1.2\times10^{-6}}\right]^{1/2}, \qquad [11]$$

where A_g is the area of one gate in cm^2 and N_{ss} is in units of $(\mathrm{cm}^2\text{-}eV)^{-1}$.

3. Discussion

The degree to which this analysis of CCD noise agrees with actual CCD noise performance will depend upon the thoroughness with which we have identified all of the noise sources. For this reason a dis-

* The bias charge mode occurs when a certain amount of charge (bias charge) is held in each potential well continuously. The transfer-loss noise analysis discussed earlier, however, considered only the complete transfer mode of operation.

cussion of why certain potential noise sources have not been included is in order.

First, switching noise is expected to be minimal in CCD sensors and delay lines because all switching noise will be at least twice the maximum signal frequency and can be filtered out by various techniques.[9]

Another possible candidate for a CCD noise source is $1/f$ noise in the CCD channel. $1/f$ noise is a generic term used to describe noise with a $1/f$ or close to $1/f$ power spectrum. It appears in many different electronic systems. $1/f$ noise in MOSFET transistors is often attributed to some type of interface trapping[10,11] and is observed to be proportional to the fast state density[6] and, therefore, might be expected to contribute in CCD's. There is no general agreement as to the exact mechanism which gives rise to $1/f$ noise in MOSFET's. The $1/f$ spectrum can be described by a set of nonconducting electronic states, equally-populated, that can communicate with the conducting channel with a wide range of response times τ. Carriers from the conducting channel are trapped in these states and detract from the output charge in the ratio τ/T_{tr} where T_{tr} is the transit time of carriers in the channel. The $1/f$ spectrum then arises because fluctuations in the long time constant states (low frequencies) contribute a greater fluctuation in the output than short time constant states (high frequencies) because of the τ/T_{tr} gain effect. However, in CCD's (assuming complete charge transfer), the trapped charge is part of the signal charge itself and there is no amplification or gain mechanism. Thus, long time constant states count no more than short time constant states and the $1/f$ mechanism should be absent in CCD's.

Table 1 shows the four basic noise sources considered, the expression for N_n, and finally the actual number for the rms fluctuation for typical values of the parameters involved. Clearly, fast interface state trapping will dominate the noise characteristics for a reasonable number of transfers (> 100). Transfer loss noise will not be a problem provided the ϵN_g product remains low. Even if ϵN_g were 1 or 2, the fluctuations would only increase to about 150 and still lie below the contribution from fast state trapping. For large signal levels ($N_s \sim 10^6$), the transfer loss noise approaches fast state noise, but the signal-to-noise ratio is correspondingly higher at the large signal levels. Likewise output-amplifier-associated noise and background-charge-generations noise are relatively small compared to trapping noise, provided capacitance levels remain in the 0.1 pf range.

The degree to which the fast state trapping will limit performance of CCD devices will depend upon the details of the specific application.

However, the present analysis suggests that other CCD-type devices in which transport does not occur at the interface and is not subject to fast interface state trapping (buried channel devices[12]) may be desirable where low-noise performance is at a premium.

Table 1—Charge-Coupled-Device Noise Sources

Source	$\overline{N_n^2}$	Typical Values for $\overline{N_n^2}$	
Transfer Loss	$[2\epsilon N_g(N_s + N_{s,o})]^{1/2}$	70	
Background Charge Generation			
Thermal or Optical	$\sqrt{N_{s,o}}$	100	
Electrically-introduced	$400\sqrt{C_{pf}}$	40	C_{pf}=0.01
Output Amplifier			
RC-limited bandwidth	$400\sqrt{C_{pf}}$	120	C_{pf}=0.1
Floating diffusion reset	$400\sqrt{C_{pf}}$	120	C_{pf}=0.1
Floating gate reset	filterable		negligible
MOSFET	$60C_{pf}\sqrt{\left(\frac{\Delta B}{5\text{MHz}}\right)\left(\frac{1000\mu\text{mho}}{g_{mo}}\right)}$	6	C_{pf}=0.1 ΔB=5MHz g_{mo}=1000μmho
Fast Interface State Trapping	$670\left[\frac{N_{ss}}{10^{10}}\frac{N_g}{10^3}\frac{A_g}{1.25\times10^{-6}}\right]^{1/2}$	670 for 1000 transfers	

$N_{s,o} = 1.25 \times 10^4$ $N_s = 1.25 \times 10^4$ $\epsilon N_g = 0.1$

$A_g = 1.25 \times 10^{-6}\text{cm}^2$ $N_{ss} = 10^{10}(\text{cm}^2\text{—eV})^{-1}$

Acknowledgments

The authors are grateful to A. Rose for his continuing interest and guidance in the development of the noise concepts reported here. We are also pleased to acknowledge R. Martinelli for his suggestion to use the Bernoulli trials approach and E. Ramberg for his help in evaluating the resultant integral. Stimulating discussions with B. Williams and R. Ronen also contributed to this work. The careful manuscript typing by Mrs. Mary Frances Pennington is also appreciated.

Appendix 1—Carrier Fluctuations for Parallel RC Circuit

Several of the noise sources associated with the CCD involve the thermal noise of a resistance that is in parallel with a capacitance.

Of interest is the rms fluctuation in the number of carriers on the capacitance. Fig. 2 shows the circuit diagram of the configuration to be analyzed along with the noise equivalent circuit. The resistance R is equivalent to a noise current source $\overline{i_n^2} = 4kT\Delta B/R$ in parallel

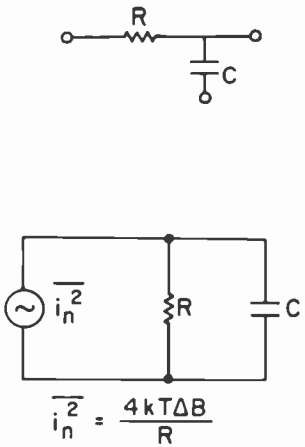

Fig. 2—*RC* circuit and noise equivalent circuit.

with R. The voltage fluctuations across the RC network will depend upon its frequency characteristics. The mean-squared noise voltage per unit bandwidth is given by:

$$\overline{v_n^2} = \frac{\overline{i_n^2}}{|G|^2} \qquad [12]$$

where

$$G = \frac{1}{R} + j\omega C \qquad [13]$$

$$|G|^2 = \frac{1}{R^2}(1 + \omega^2 R^2 C^2). \qquad [14]$$

The total mean-squared noise voltage will be the integral over frequency of $\overline{v_n^2}$:

$$\overline{V_n^2} = \int_0^\infty \overline{v_n^2}\, df = \frac{4kT}{2\pi C} \int_0^\infty \frac{\frac{1}{RC}\, d\omega}{\frac{1}{R^2C^2} + \omega^2}. \qquad [15]$$

Since the integral is just $\pi/2$,

$$\overline{V_n^2} = \frac{kT}{C}. \qquad [16]$$

The rms carrier fluctuation is then:

$$\overline{N_n} = \frac{1}{q} C\overline{V_n} = \frac{1}{q} (kTC)^{1/2} = 400\ (C_{pf})^{1/2}. \qquad [17]$$

Note that while the resistance is the source of the fluctuations, its value does not affect the total carrier fluctuations. This is so because, while larger values of R increase the mean-squared noise voltage per unit bandwidth, they decrease the effective bandwidth by the same factor. A large capacitance reduces the bandwidth by $1/\sqrt{C}$, thereby reducing the noise voltage, but increases the number of carrier fluctuations for a given rms noise voltage by C; thus the $\sqrt{C}$ dependence.

Appendix 2—Steady-State Mean-Squared Fluctuations in Number of Carriers Trapped in Fast Interface States

A. van der Ziel[13] has derived the probability distribution of the number of carriers in the conduction band of a semiconductor $P(N)$, where the probability of an electron being generated in the time dt is $g(N)dt$ and the probability of an electron recombining in time dt is $r(N)dt$ (dt is small enough that multiple electron processes are negligible). The derivation is quite general and assumes that g and r are functions only of N, not of time. Thus the results apply for any collection of particles whose number changes only via the probabilities $g(N)$ and $r(N)$.

Van der Ziel shows that the most probable value N_o will satisfy the following condition:

$$g(N_o) = r(N_o+1) \cong r(N_o), \text{ for large } N_o. \qquad [18]$$

Also, the mean-squared fluctuation about N_o is given by

$$\overline{\delta N^2} = -\left[\frac{g'(N_o)}{g(N_o)} - \frac{r'(N_o+1)}{r(N_o+1)}\right]^{-1} \cong \frac{g(N_o)}{r'(N_o)-g'(N_o)}, \qquad [19]$$

where the primes denote differentiation with respect to N.

To apply these results to find the fluctuations of the total number of trapped carriers under steady-state conditions, we must identify $g(N)$ and $r(N)$ for incremental energy intervals $d\mathcal{E}$ and then integrate Eq. [19] over the bandgap to determine the total mean-squared fluctuations.

The kinetic equation that has been assumed to describe changes in occupation of fast states in energy interval $d\mathcal{E}$ located $\mathcal{E}$ below the conduction band is given by[8]

$$\frac{d}{dt}(n_{ss}d\mathcal{E}) = k_1 n_s(N_{ss}-k_2 n_{ss}d\mathcal{E}\exp\ n_{ss})d\mathcal{E} - \left\{-\frac{\mathcal{E}}{kT}\right\}, \qquad [20]$$

where n_{ss} is the number of occupied fast states in $(\text{cm}^2\text{—eV})^{-1}$

N_{ss} is the density of fast states in $(\text{cm}^2\text{—eV})^{-1}$

k_1 and k_2 are constants ($k_1 \approx 10^{-2}$, $k_2 \approx 10^{11}$)

n_s is the density of free carriers in the conduction band (assumed constant)

Eq. [20] assumes that n_s is large enough that the number of carriers removed by trapping is small compared to n_s. Thus $n_{ss}d\mathcal{E}$ corresponds to N and

$$g(n_{ss}d\mathcal{E}) = k_1 n_s(N_{ss} - n_{ss})\,d\mathcal{E} \qquad [21]$$

$$r(n_{ss}d\mathcal{E}) = k_2 n_{ss}d\mathcal{E}\exp\left\{-\frac{\mathcal{E}}{kT}\right\}. \qquad [22]$$

Here, generation corresponds to the trapping of a free carrier from the conduction band, and recombination corresponds to emission of a trapped carrier into the band.

The most probable value n_{ss}^{o} is given by

$$n_{ss}^{o} = \frac{N_{ss}}{1 + \exp\left\{\dfrac{\mathcal{E}_Q - \mathcal{E}}{kT}\right\}}, \qquad [23]$$

where

$$\mathcal{E}_Q = kT \ln\left(\frac{k_2}{k_1 n_s}\right). \qquad [24]$$

Using Eq. [19], the mean squared fluctuation in each energy interval $d\mathcal{E}$ is given by

$$d(\overline{\delta N^2}) = \frac{k_1 n_s d\mathcal{E}\,(N_{ss} - n_{ss}^{o})}{k_2 \exp\left\{-\dfrac{\mathcal{E}}{kT}\right\} + k_1 n_s} = \frac{N_{ss} d\mathcal{E} \exp\left\{\dfrac{\mathcal{E}_Q - \mathcal{E}}{kT}\right\}}{\left[1 + \exp\left\{\dfrac{\mathcal{E}_Q - \mathcal{E}}{kT}\right\}\right]^2} \qquad [25]$$

Eq. [25] expresses the fluctuations in each interval $d\mathcal{E}$ only, and the total mean squared fluctuations N_t^2 is the integral over the forbidden gap:

$$\overline{N_t^2} = \int_0^{\mathcal{E}_g} d(\overline{\delta N^2}) = \int_0^{\mathcal{E}_g} \frac{N_{ss} \exp\left\{\dfrac{\mathcal{E}_Q - \mathcal{E}}{kT}\right\} d\mathcal{E}}{\left[1 + \exp\left\{\dfrac{\mathcal{E}_Q - \mathcal{E}}{kT}\right\}\right]^2}. \qquad [26]$$

Assuming N_{ss} is uniform in energy, $\mathcal{E}_Q/kT \gg 1$ and $\mathcal{E}_g - \mathcal{E}_Q/kT \gg 1$, and using the substitution $u = \exp\{(\mathcal{E}_Q - \mathcal{E})/kT\}$, we have

$$\overline{N_t^2} = kTN_{ss} \int_0^{\infty} \frac{du}{(1+u)^2} = kTN_{ss}. \qquad [27]$$

Thus, for steady-state conditions, the mean-squared fluctuation in the number of trapped carriers is simply kTN_{ss} per unit area.

Appendix 3—Mean-Squared Fluctuation of Trapped Carriers in Complete-Charge Transfer Mode with Fat Zero

For the complete charge transfer mode of CCD operation, the mean-squared fluctuation in the total number of trapped carriers $\overline{N_t^2}$ is no longer given by the steady-state value kTN_{ss}. A different approach must be used to find the fluctuations in the number of trapped carriers. During the transfer-in-period, $-1/2f < t < 0$, with the fat zero present, the fast states fill to the level

$$n_{ss}(0) = n_{ss}\left(-\frac{1}{2f}\right) + \left[n_{ss}(\infty) - n_{ss}\left(-\frac{1}{2f}\right)\right](1 - \exp\{-f_o/f\}) \qquad [28]$$

where $n_{ss}(t)$ is the density of occupied fast interface states in $(\text{cm}^2\ \text{eV})^{-1}$ and $f_o = k_1 n_{s,0}/2$. In the time from 0 to $1/(2f)$, the transfer-out period, the occupation decreases toward $n_{ss}\,[1/(2f)]$ which must be on the average the same as $n_{ss}\,[-1/(2f)]$.

The probability that any state will empty in time dt is dt/τ times the probability that it is still filled, $\exp\{-t/\tau\}$ [τ is the empty time given by $(1/k_2)\exp\{\mathcal{E}/kT\}$]. Thus the probability that a state will empty in time $1/(2f)$ is given by

$$p = \int_0^{1/2f} \frac{dt}{\tau} \exp\left\{-\frac{t}{\tau}\right\} = 1 - \exp\left\{-\frac{1}{2f\tau}\right\}. \qquad [29]$$

So, at $t = 0$, at each energy interval $d\mathcal{E}$, there are $n_{ss}(0)d\mathcal{E}$ states filled. They each have probability $p = 1 - \exp\{-1/(2f\tau)\}$ of emptying by time $1/(2f)$ and probability $q = 1 - p$ of not emptying. This is an example of Bernoulli trials[14] with $n = n_{ss}(0)d\mathcal{E}$, $p = 1 - \exp\{-1/(2f\tau)\}$, and $q = \exp\{-1/(2f\tau)\}$. The average number of states that have emptied at $t = 1/(2f)$ is

$$\text{Average Number of States to Empty} = pn = [1 - \exp\{-1/(2f\tau)\}]n_{ss}(0)d\mathcal{E}.$$

The variance, or mean-squared fluctuation about this average, is

$$\text{Variance} = pqn = n_{ss}(0)d\mathcal{E}\,[1 - \exp\{-1/(2f\tau)\}]\exp\{1/(2f\tau)\}. \qquad [30]$$

The total mean-squared fluctuations in the number of trapped carriers at $t = 1/(2f)$ is the integral of Eq. [30] over energy

$$\overline{N_t^2} = \int_0^{\mathcal{E}_g} n_{ss}(0)\, d\mathcal{E}\, [1 - \exp\{-1/(2f\tau)\}] \exp\{1/(2f\tau)\}$$

$$= \int_0^{\mathcal{E}_g} n_{ss}(\infty)\, d\mathcal{E}\, \frac{[1 - \exp\{1/(2f\tau)\}]\,[1 - \exp\{-f_o/f\}]}{\exp\{1/(2f\tau)\} - \exp\{-f_o/f\}}. \qquad [31]$$

$n_{ss}(\infty)$, the steady-state occupation with the fat zero present, can be replaced by N_{ss} in this integral because the factor $[1 - \exp\{-1/(2f\tau)\}] \exp\{-1/(2f\tau)\}$ is a sharply-peaked function at energy $\mathcal{E}_p = kT\ln[k_2/(2f\ln 2)]$. $n_{ss}(\infty)$ is just N_{ss} times the Fermi function with quasi-Fermi level $kT\ln[k_2/(k_1 n_{s,o})]$. Only for $n_{s,o}$ values less than approximately 10^9 will $n_{ss}(\infty)$ have a value less than N_{ss} at $\mathcal{E}_p$.

Even with this approximation, the integral in Eq. [31] cannot be evaluated in closed form, but a series solution is possible. By making appropriate substitutions, Eq. [31] can be written

$$\overline{N_t^2} = kTN_{ss}(1 - \exp\{-f_o/f\}) \int_{l_2}^{l_1} \frac{(1-x)\,dx}{[1 - x\exp\{-f_o/f\}]\ln x} \qquad [32]$$

where

$$l_1 = \exp\left\{\frac{-k_2}{2f}\right\}$$

$$l_2 = \exp\left\{-\frac{k_2}{2f}\left[\exp\left(-\frac{\mathcal{E}_g}{kT}\right)\right]\right\}.$$

By expanding $(1 - x\exp\{-f_o/f\})^{-1}$ as a series, we have

$$\overline{N_t^2} = kTN_{ss}(1 - \exp\{-f_o/f\}) \int_{l_2}^{l_1} dx \left[\sum_{j=0}^{\infty} \frac{(-1)^j \left(x\exp\left\{-\frac{f_o}{f}\right\}^j\right)}{\ln x} - \sum_{j=0}^{\infty} \frac{(-1)^j \left(\exp\left\{-\frac{f_o}{f}\right\}\right)^j x^{j+1}}{\ln x}\right]. \qquad [33]$$

This can be further reduced to a sum of logarithmic integrals $\mathrm{li}(y)$ where

$$\mathrm{li}(y) = \int_0^{e^y} \frac{dx}{\ln x}, \qquad [34]$$

which results in the following form:

$$\overline{N_t^2} = kTN_{ss}(1-e^{-f_o/f}) \sum_{j=1}^{\infty} (-1)^{j-1} (e^{-f_o/f})^{j-1} \ln\left(\frac{j+1}{j}\right). \qquad [35]$$

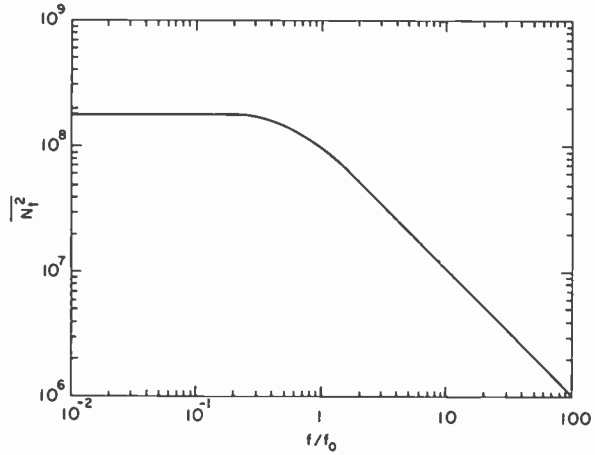

Fig. 3—Mean-squared fluctuation in total number of trapped carriers versus normalized frequency for complete charge transfer mode with fat zero.

Fig. 3 shows $\overline{N_t^2}$ as a function of f/f_o for $N_{ss} = 10^{10}$. Above $f/f_o = 1$ the fluctuations fall off as f/f_o. However, below $f/f_o = 1$, they are constant at $kTN_{ss} \ln 2$. Since as discussed earlier, f/f_o values must be less than 1 in order to suppress interface state losses, the mean-squared fluctuations due to fast state trapping in the complete charge transfer mode will be $0.7kTN_{ss}$.

References:

[1] W. S. Boyle and G. E. Smith, "Charge-Coupled Semiconductor Devices," **Bell Syst. Tech. J.**, Vol. 49, p. 587, (1970).
[2] W. F. Kosonocky and J. E. Carnes, "Two-Phase Charge-Coupled Shift Registers," **Digest Tech. Papers, IEEE International Solid State Circuit Conf.**, Philadelphia, Pa., p. 132, Feb. 1972.

[3] M. F. Tompsett, G. F. Amelio, W. J. Bertram, R. R. Buckley, W. J. McNamara, J. C. Mikkelsen, and D. A. Sealer, "Charge-Coupled Imaging Devices: Design Considerations," **IEEE Trans. Elec. Dev.**, Vol. ED-18, p. 992, Oct. 1971.
[4] W. F. Kosonocky and J. E. Carnes, "Charge-Coupled Digital Circuits," **IEEE J. Solid-State Circuits**, Vol. SC-6, p. 314, (1971).
[5] F. M. Klaassen and J. Prins, "Thermal Noise of MOS Transistors," **Phillips Res. Repts**, Vol. 22, p. 505, 1967.
[6] F. M. Klaassen, "Characterization of Low 1/f Noise in MOS Transistors," **IEEE Trans. Elec. Dev.**, Vol. ED-18, p. 10, Oct. 1971.
[7] R. Ronen, private communication.
[8] J. E. Carnes and W. F. Kosonocky, "Fast Interface State Losses in Charge-Coupled Devices," **Appl. Phys. Ltrs.**, Vol. 20, April 1, 1972, p. 261.
[9] M. G. Kocac, W. S. Pike, F. V. Shallcross and P. K. Weimer, "Solid State Imaging Emerges from Charge Transport," **Electronics**, p. 72, Feb. 28, 1972.
[10] S. Christensson, I. Lundstrom, and C. Svensson, "Low Frequency Noise in MOS Transistors," **Solid-State Electron.**, Vol. 11, p. 813, 1968.
[11] F. Berz, "Theory of Low Frequency Noise in Si MOST's," **Solid-State Electron.**, Vol. 13, p. 631, 1970.
[12] G. E. Smith, et. al., "A Buried Channel Charge Coupled Device," IEEE Device Research Conf., Ann Arbor, Mich., June, 1971.
[13] A. van der Ziel, "Semiconductor Noise," in **Noise in Electron Devices** ed. by L. D. Smullin and H. A. Haus, Wiley, New York, 1959, p. 320.
[14] William Feller, **An Introduction to Probability Theory and Its Applications**, Vol. 1, p. 146, Wiley, New York (1950).

A Solid-State Transponder Source Using High-Efficiency Silicon Avalanche Oscillators*

J. F. Reynolds, J. Assour, and A. Rosen

RCA Laboratories, Princeton, N. J.

Abstract—An all solid-state transmitter source using high-efficiency high-power silicon avalanche diodes is described. The small size (4 × 2 × 2.5 inches), frequency stability over a wide temperature range, and duty-cycle capability make these sources compatible with the requirements of military and commercial transponder systems. Sources operated at L-band in the transponder maximum pulse-reply code have delivered up to 350 watts.

Introduction

High-efficiency, high-power silicon avalanche diodes properly tuned in a variety of L-band microwave cavities[1-3] have delivered pulsed power levels up to 1.2 kW peak with efficiencies reaching 45%. Their long operating life,[4] frequency stability over a wide temperature range (−50°C to 120°C), high duty cycle capability, and low-cost fabrication make them compatible with the requirements of military and commercial communication systems. In this paper, the development of a prototype source for IFF transponder application is described. The source, shown in Fig. 1, consists of a pulsed high-efficiency silicon

* Partially supported by the U.S. Air Force Avionics Laboratory under Contract No. F33615-67-C-1981.

avalanche oscillator, a TEM coupled-bar microwave circuit, a transistorized modulator, and a ferrite circulator-isolator. It has been operated at L-band in the maximum pulse-reply transponder code and has delivered up to 350 watts peak.

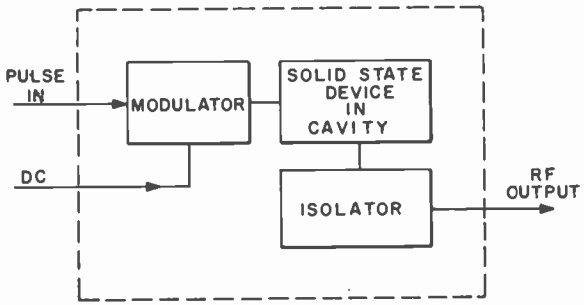

Fig. 1—Schematic of Transmitter module.

Characteristics and Fabrication of Avalanche Devices

The high-efficiency avalanche devices are narrow-base p+-n-n+ or (n+-p-p+) silicon diodes designed for L-band frequencies. To operate in the high-efficiency, high-power avalanche mode, the diodes are reverse-biased beyond their breakdown voltage by the application of high-current-density pulses.[5] During the plasma formation, the diode must sustain critical field values of about 3×10^5 Vcm^{-1}, and respond to peak current densities of the order of 10,000 Acm^{-2}. To prevent premature microplasma breakdown and burnout, the diodes were fabricated with minimum crystallographic defects and very low thermal resistances.

To prepare the devices, phosphorous-doped n-layers were first grown by epitaxy on antimony-doped <111> or <100> n+ substrates. The resistivity, thickness, impurity distribution, and crystallinity of the epitaxial layers were characterized, and only good quality n-layers were further processed. p+-n junctions were formed by diffusing boron into n-layers to achieve heavily-doped shallow p+-layers without defects due to dopant precipates. Low-temperature silicon dioxide films doped with boron were used as the diffusion source. The silicon diodes have a p+-layer typically 4 μm wide with an average resistivity of 0.01 ohm-cm. The n-layer width was varied from 3.5 to 6 μm with a resistivity of about 7 ohm-cm. Typical impurity distributions determined by capacitance–voltage measurements for the active n-layers

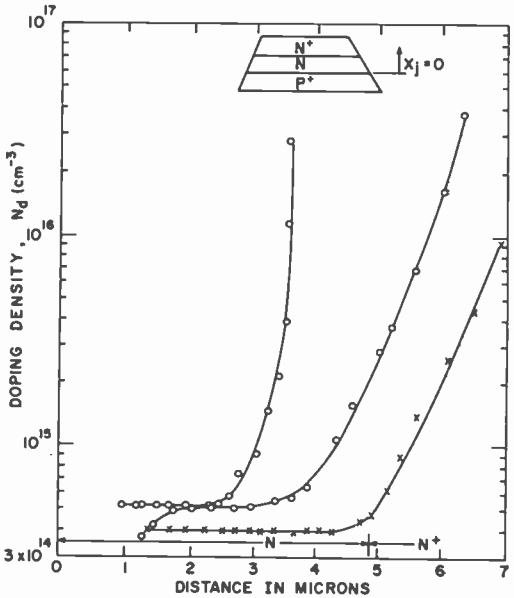

Fig. 2—Typical doping profiles of avalanche diodes.

are shown in Fig. 2. Diodes with abrupt, hyperabrupt, and graded junctions were fabricated and operated successfully.

To adequately dissipate the heat generated in the p+-n junction during high-duty-cycle operations, the diodes were flip-chip bonded to a copper heat sink. This is a thermocompression bonding technique and has been developed as an integral part of the fabrication process of these devices as discussed in detail elsewhere.[6] A typical structure of the device is shown in Fig. 3. The thickness of the semiconductor

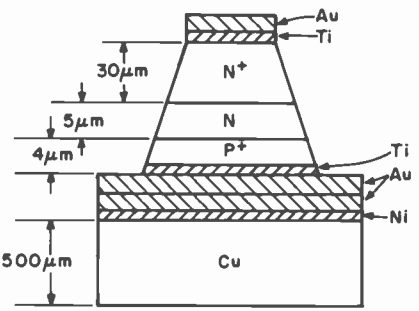

Fig. 3—Cross-section of high-power Trapatt diode with integral copper heat sink.

and metallic layers were minimized to reduce the total thermal resistance. This bonding technique has yielded measured thermal resistance values $R_{th} = 6.5$ (°C/W) for 0.020-inch-diameter diodes and $R_{th} = 9.7$ (°C/W) for 0.010-inch-diameter diodes.

To obtain large output powers, several diodes were mounted in a multichip package designed to connect the devices in series electrically and thermally in parallel on a BeO substrate as shown in Fig. 4. Packages of this type have delivered 650 watts at 1090 MHz with 20% efficiency.

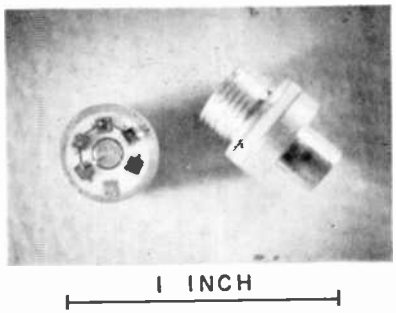

Fig. 4—Photograph of miltiple chip package. Four copper-mounted diodes are shown connected in series electrically.

Transmitter Design

RF Circuit

For high-efficiency operation a multi-resonant circuit was designed to support harmonic frequencies through the nominal IMPATT frequency of the diode (low X-band). These harmonic frequencies are necessary to trigger the initial plasma formation and to sustain the high-efficiency operation. The circuit must also provide an optimum impedance matching at the fundamental oscillation frequency (1090 MHz) for maximum output power. The coupled TEM-bar circuit shown schematically in Fig. 5 satisfies these requirements. Practical circuits in conventional stripline configurations have been built which occupy a $1 \times 7/8 \times 2$ inch volume. In addition, the circuit has been also fabricated[7] in a microstrip configuration for high-reliability performances. As shown in Fig. 5, the circuit consists of two bars of length $L = \lambda/8$ that are positioned between appropriate ground planes. The bars are terminated in variable capacitors (C_1, C_2, C_3, C_4). These capacitors provide the tuning necessary for harmonic loading. Single devices

operated in this type circuit have yielded over 200 watts with 40% efficiencies.

To improve the performance for a wider range of devices, the circuit concept proposed by Evans[8] was investigated. This consists of positioning the device at a distance approximately $\lambda/2$ from a low-pass filter and matching section. This was accomplished with the bar circuit

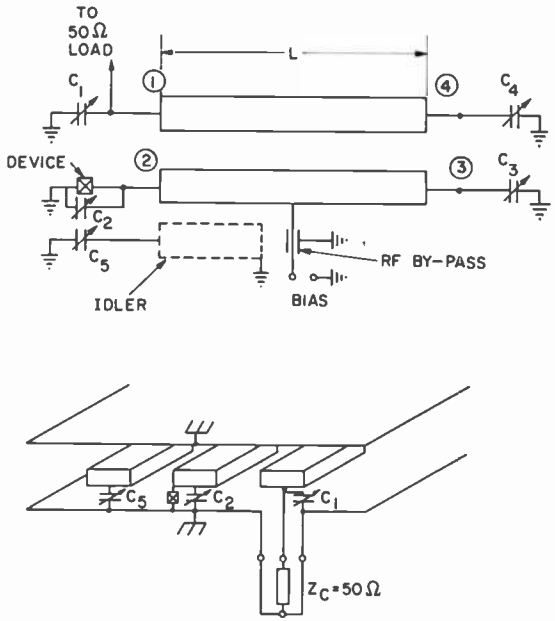

Fig. 5—Schematic of coupled TEM bar circuit.

by simply repositioning the device $\lambda/2$ away from its original position with a 50-ohm coaxial line. Also, an additional tuner for the IMPATT frequency was incorporated in the 50-ohm line near the device. With this circuit, over 220 watts with 46% efficiency was achieved.

Modulator

To achieve a practical and self-contained transmitter source, a solid-state pulse modulator was developed for biasing the silicon diodes into avalanche breakdown. The modulator is capable of delivering voltages up to 500 V, currents up to 10 A, and fast pulses with rise times on the order of 50 nsec.

In order to achieve the desired voltages and currents, a dc bias

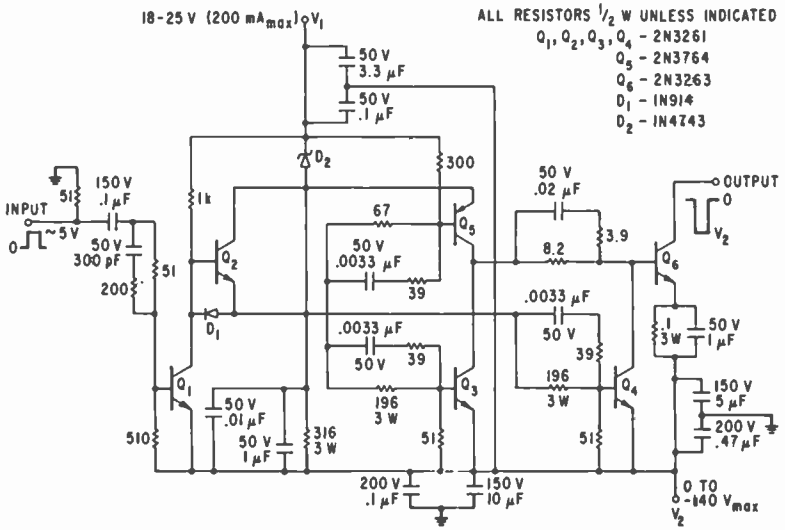

Fig. 6—Pulser circuit.

scheme was employed.[9] With this technique, the diode is continually reverse bias below breakdown with a dc voltage and then pulsed into the high-efficiency mode with a fast-rise pulse. This pulse is supplied by a driver circuit that consists of a high-voltage, high-current transistor switch. A schematic of the basic driver is shown in Fig. 6, and the full modulator is shown in Fig. 7.[10] The modulator has also been designed to operate over a temperature range of −54°C to +125°C in the full transponder burse mode at 1% duty cycle.

The characteristics of the high-efficiency mode of operation of avalanche diodes introduce another problem to the modulator design, that of modulator efficiency. All pulse schemes that are presently used, including the modulator described above, employ a flat-top pulse whose amplitude is equal to or greater than the breakdown voltage of the diode. When the device is operated in the high-efficiency mode, however, the voltage across the diode drops by 30% to 50%. This excess voltage must be taken up by the output impedance of the pulser. In

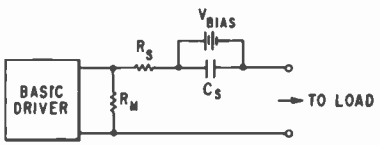

Fig. 7—Diagram of modulator for avalanche diodes.

the case of the modulator shown in Fig. 7, this is done by R_s. The efficiency of the modulator is then only 50% to 70%. This is a serious drawback in system applications and overrides one of the inherent advantages of the diode.

The approach that can be used in increasing the modulator efficiency is to make use of the property of the diode that leads to the problem in the first place, the drop in operating voltage once the diode goes into the high-efficiency mode. Instead of using a conventional flat-top pulse, the general idea is to use a pulse shape similar to that shown in Fig. 8. The pulse consists of a narrow high-voltage spike

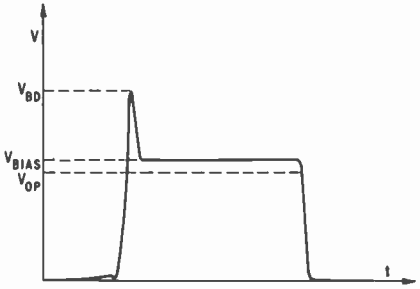

Fig. 8—Output waveform for ideal modulator for Trapatt diodes.

followed by a much longer low-voltage portion. The high-voltage spike serves to break the diode down and then switch it into the high-efficiency mode. When this occurs, the diode voltage drops to V_{op}, and at the same time the pulse voltage is dropped to V_{bias}. The diode is then sustained in the high-efficiency mode by a voltage V_{bias} that is only slightly greater than its operating voltage. Only a small series resistor is required and, since the high-voltage spike is of very short duration, the modulator efficiency approaches 100% and the overall system efficiency (modulator plus diode) becomes almost equal to the diode efficiency.

Modulators of this design have been successfully designed and tested. These modulators achieved between 80% and 90% efficiency when operating with avalanche diodes. This was only for single-pulse operation, and the design has not yet been adapted for operation in the pulse burst mode. It demonstrated, however, the feasibility of the approach and that it should be considered for use in refined versions of the transmitter modules.

Circulator

A commercial miniature circulator/isolator is used to prevent frequency pulling with VSWR changes. It has been found that an isolator with 20 dB isolation is sufficient to keep frequency changes below 1 MHz for VSWRs up to 2.0:1. A photograph of a complete experimental unit is shown in Fig. 9.

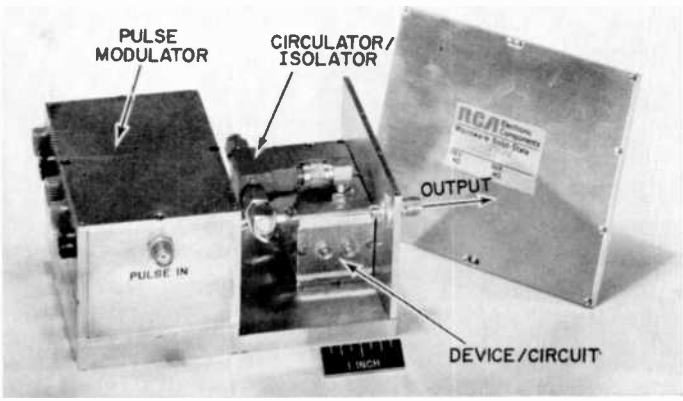

Fig. 9—Complete transmitter source.

Transmitter Performance

The results reported here have been obtained for sources operated at L-band in the maximum pulse-reply transponder code. Typical output power from sources containing a single avalanche diode varied from 120 to 150 watts. Sources containing three diodes in series have delivered up to 350 watts. Typical detected rf output, biasing current, and spectral output are shown in Figs. 10 and 11 for a 150-watt unit. The rise time of the rf output pulse is typically 50 nsec, while the leading edge jitter is less than 50 nsec. Note that the rf pulse follows closely the shape of the current pulse. The power variation over the length of the fourteen pulse train is 0.5 dB. The frequency variation is typically 1 MHz.

A summary of the results of system evaluation tests* on three

* Test data courtesy of Hazeltine Corporation, Plainview, New York.

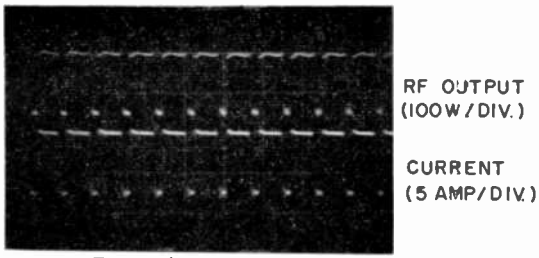

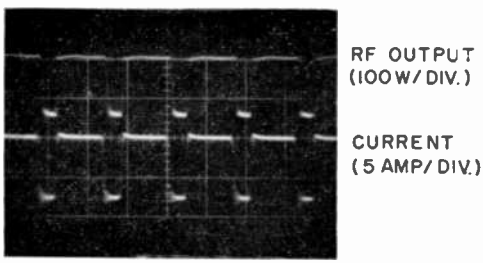

Fig. 10—Photograph showing operation of 150-watt Trapatt diode under pulse-burst conditions.

typical units is given in Table 1. The performance of the third unit as a function of temperature is given in Table 2 and Fig. 12. As can be seen, the total frequency variation is 7.7 MHz and the power variation is 1.2 dB.

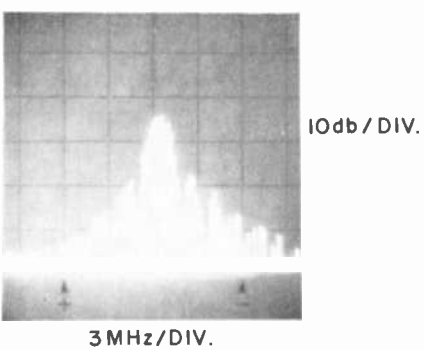

Fig. 11—Photograph showing pulse operation of 150-watt Trapatt diode.

Table 1—Test Data on Transmitter Sources. (Unless otherwise noted, all readings are for a train of 14 pulses, each 0.45 μs wide and spaced 1.45 μs; at room ambient temperature, altitude, and humidity; at nominal power supply voltages; at a 0.1% duty cycle and into a 50-ohm load.)

Basic Characteristics	Specification Limits	Readings
A. Power Output		
First Transmitter	29.0-31.0 dBW	25.6 dBW
Second Transmitter	29.0-31.0 dBW	21.0 dBW
Third Transmitter	29.0-31.0 dBW	22.2 dBW
B. Output Frequency		
Second Transmitter		
First Pulse	1090.0±3 MHz	1121.74 MHz
Last Pulse	1090.0±3 MHz	1120.78 MHz
Third Transmitter		
First Pulse	1090.0±3 MHz	1209.69 MHz
Last Pulse	1090.0±3 MHz	1208.19 MHz
C. Droop across train		
First Transmitter	1.0 dB (max)	0.4 dB
Second Transmitter	1.0 dB (max)	0.5 dB
Third Transmitter	1.0 dB (max)	0.7 dB
D. Pulse Characteristics		
Second Transmitter:		
Width (Widest Pulse)	.35-.55 μs	.50 μs
(Narrowest Pulse)	.35-.55 μs	.48 μs
Rise Time	.05-.10 μs	.05 μs
Fall Time	.05-.20 μs	.04 μs
Third Transmitter:		
Width (Widest Pulse)	.35-.55 μs	0.5 μs
(Narrowest Pulse)	.35-.55 μs	0.5 μs
Rise Time	.05-.10 μs	.04 μs
Fall Time	.05-.20 μs	.04 μs
E. Jitter		
Second Transmitter	0.1 μs (max)	0.11 μs
Third Transmitter	0.1 μs (max)	0.02 μs
F. Pulse-to-Pulse Movement (Effect on pulse in train when pulse preceding it is removed)		
Second Transmitter		
Change in position		-0-
Change in width		-0-
Third Transmitter		
Change in position		-0-
Change in width		-0-
G. VSWR Effects (1.5:1)		
Third Transmitter		
Power Range	28.0 dBW	20.0-21.6
Frequency Range	1090.0±3.0 MHz	1209.48-1210.25
H. Transmitter delay		
Second Transmitter	1.5 μs (max)	0.2 μs
I. Efficiency		
Second Transmitter		
Device & Modulator		7.6%
Device only		23.4%
J. Input Voltage Variations		
Second Transmitter		none
V_2		none
Bias		Could not
+21 (Modulator)		exceed +22 volts

Table 2—Temperature Testing (at 0.1% duty cycle) Third Transmitter

Temp	Power Output	Output Frequency		Droop	Pulse Width	Rise Time	Fall Time	Pulse Jitter	Notes
		1st Pulse	14th Pulse						
°C	dBW	MHz	MHz	dB	μs	μs	μs	ns	
+50	21.4	1208.02	1206.68	1.4	0.6	0.04	0.04	20	
−25	22.2	1211.93	1209.12	0.8	0.48	0.05	0.08	20	
−50	22.2	1212.49	1209.88	1.2	0.48	0.2	0.1	40	Last Pulse Rise Time = 0.3 μs Fall Time = 0.08 μs Width Time = 0.3 μs
72	21.0	1207.07	1204.79	2.1	0.49	0.1	0.07	30	Unit burned-out after 10 minutes of operation.

Conclusion

Solid-state transmitter sources using high-efficiency, high-power silicon avalanche diodes have been developed to meet the requirements of military transponder systems. Output powers of 850 watts have been obtained from multiple diodes in a coupled-bar circuit. Presently, complete transmitter sources with output powers ranging from 100 to 350 watts have been developed using single and multiple chips.

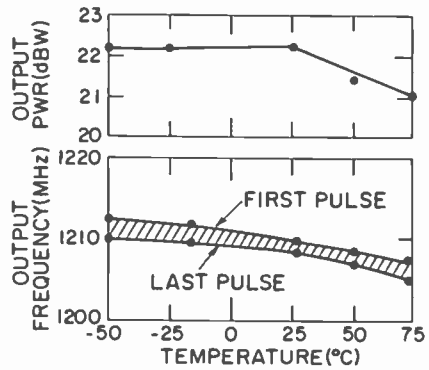

Fig. 12—Temperature characteristics of diode module.

While significant progress was made towards developing silicon avalanche diode sources for use in IFF transponders, work remains to be done in several areas to improve overall performance. These areas include, first, improvements in diode thermal properties in order for the diode to reliably operate at 125°C at 1% duty cycle in the pulse burst mode. Second, improvements in the rf circuit can be made in order to increase rf conversion efficiency and environmental stability. Third, work on diode, package and circuit redesign can be done to improve pulse jitter. Although the performance of the present units is well within specification limits for this system application, further reduction in pulse jitter would increase the usefulness of the source. Fourth, additional effort on the modulator is required in order to improve efficiency, reduce current droop across the burst, and, thereby, increase frequency stability and reduce cost.

Acknowledgment

The authors wish to express their appreciation to J. Murr, D. Tarangioli and V. Lawson for diode fabrication and to E. C. McDermott and L. Seminestow for circuit fabrication and device testing.

References:

[1] H. J. Prager, K. K. N. Chang, and S. Weisbrod, "High-power, high-efficiency silicon avalanche diodes at UHF and L-band," **Proc. IEEE,** Vol. 55, p. 586, (1967).
[2] S. G. Liu and J. J. Risko, "Fabrication and performance of kilowatt L-band avalanche diodes," **RCA Review,** Vol. 31, p. 3, (1970).
[3] J. F. Reynolds et al, "Coupled TEM bar circuit for L-band silicon avalanche oscillators," **Proc. IEEE,** Vol. SC-5, p. 347, (1970).
[4] Technical Report No. AFAL-TR-69-255, **Avalanche Diode Devices,** Aug. 1969.
[5] A. S. Clorfeine, R. J. Ikola, and L. S. Napoli, "A theory for the high-efficiency mode of oscillation in avalanche diodes," **RCA Review,** Vol. 30, p. 397, (1969).
[6] J. M. Assour, J. Murr, Jr., and D. Tarangioli, "On the fabrication of high-efficiency silicon avalanche diodes," **RCA Review,** Vol. 31, p. 499, (1970).
[7] A. Rosen and J. Assour, "Silicon avalanche diode miscrostrip L-band oscillator," **IEEE Trans.,** Vol., MTT-18, p. 979, (1970).
[8] W. J. Evans, "Circuits for high-efficiency avalanche-diode oscillators," **IEEE Trans. Microwave Theory Tech.,** MTT-17, p. 1060, (1969).
[9] A. Clorfeine, R. D. Hughes, and S. Weisbrod, "Low-cost pulsing of avalanche diodes," **RCA Review,** Vol. 32, p. 489 (1971).
[10] High Power L-Band Source, **Tech. Report,** No. AFAL-TR-71-108, June 1971.

Negative Resistance in Cadmium Selenide Powder—Comparison of Experiment and Theory

L. J. Nicastro

RCA Advanced Technology Laboratories, Camden, N. J.

E. L. Offenbacher

Temple University, Philadelphia, Pa.

Abstract—Cadmium selenide powder, after the incorporation of copper and chlorine impurities, exhibits negative resistance behavior when the voltage applied across a sample exceeds a certain threshold value. This threshold voltage is reduced when visible or near infrared light is incident on the sample. Experimental results for the variation of the threshold voltage (V_{th}) with light intensity (I) and frequency are reported in this paper. A theoretical model is described in which the threshold voltage is related to the incident light intensity, the absorption coefficient, the quantum efficiency for radiative recombination of current carriers, the mobility and recombination lifetime of conduction band electrons, and the thickness of the sample. The prediction of this model for the dependence of V_{th} on I is in good agreement with the experimentally observed behavior.

1. Introduction

Pure cadmium selenide (CdSe) is an insulator with a bandgap energy of 1.7 eV. Negative resistance in the current–voltage characteristic of CdSe powder was first reported by Nicoll.[1] The effect is observed only after copper and chlorine impurities are added to CdSe powder through a series of specialized processes described by Hinnenkamp.[2]

When the voltage applied across a sample of this CdSe powder exceeds a certain threshold value, V_{th}, negative resistance is observed as an abrupt increase in current while the voltage across the sample decreases. This threshold voltage is reduced by irradiating the sample with visible or near infrared radiation.[1] Smith[3] also observed that after the threshold voltage has been exceeded, the material emits radiation equivalent to the bandgap and lower frequencies. Based on the model described below, this emission of light is due to radiative recombination of conduction-band electrons both with unfilled acceptor levels and with holes in the valence band; the reabsorption of part of the recombination radiation within the material provides excess electrons to the conduction band. When external light is incident on the sample the production of excess electrons in the conduction band is enhanced, and thus the threshold voltage is reduced.

The results of an experimental investigation of the variation of threshold voltage with light intensity and frequency are presented in this paper. The results for CdSe powder are best interpreted by using a model based on the rate equation for the production of excess electrons in the conduction band in conjunction with the following assumptions. (1) The initial current density is proportional to the first power of the voltage. (2) The quantum efficiency for radiative recombination of current carriers is an increasing function of the current density. (3) The effective current density consists of the sum of the pre-breakdown current and a linear photocurrent generated by the absorption of electron–hole recombination radiation.

The above model is very similar to the model first described by Dumke[4,5] and extended by Weiser[6] to explain the negative-resistance characteristic in single-crystal GaAs p-i-n junctions. It differs only in that they assumed a quadratic dependence of the pre-breakdown current on voltage, while a linear dependence of pre-breakdown current on voltage gives the best representation for the experimental results with CdSe.

The variation of threshold voltage with frequency, which can be ascribed to the frequency dependence of the absorption coefficient of CdSe, also has been investigated. A detailed description of the frequency effects will appear elsewhere.

2. Weiser's Theory of Negative Resistance

2.1 Weiser's Model

An energy diagram of the model on which Weiser based his theory is shown in Fig. 1. The n and p regions are considered to be heavily

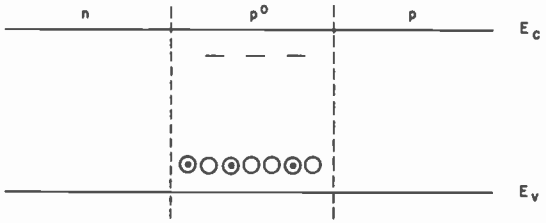

Fig. 1—Impurity scheme of p-p°-n material. E_c and E_v are the edges of the conduction and valence bands. The dashes signify ionized donors, dotted circles signify acceptors ionized by electrons, and the open circles correspond to acceptor levels that are not ionized. The n and p regions are heavily doped.

doped, and the high-resistivity central region (the p^o region) is assumed to be lightly doped p-type. It is also assumed that the width of the p^o region is many times the diffusion length of either electrons or holes. In Weiser's theory, the negative resistance is brought about as follows. Under the positive bias voltage illustrated in Fig. 2, the electrons that traverse the high-resistance region combine with holes near the p^o-p boundary. This recombination is partly radiative and some of the emitted light is absorbed in the p^o region, creating electron–hole pairs. Because of the presence of the negatively charged centers, which are presumed to have a large capture cross section for holes, the holes are immobilized, and do not contribute to the conduction process. Therefore, the result of each absorption in the p^o region is to provide an additional electron to the conduction band and to produce a hole bound to a previously filled acceptor site. Until this hole decays, the additional electron in the conduction band contributes to the conduction process. Together with the injected electrons, the photogenerated electrons flow to the p^o-p interface, recombine in part radiatively, and hence create more electron–hole pairs. Thus, a regenerative process sets in if the quantum efficiency for radiative recombination is high enough and the field is strong enough so that

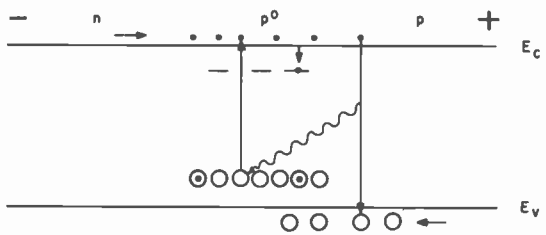

Fig. 2—p-p°-n material with voltage applied.

new electrons can be created in the p^o region at a rate faster than that at which they decay. Furthermore, the process leads to a negative resistance, as opposed to a simple feedback process, only if the quantum efficiency is an increasing function of the current at the beginning of the process. Under these conditions, the regenerative process can continue at lower and lower voltages as the quantum efficiency increases. When the quantum efficiency reaches a constant value, the process stops, and the dynamic resistance becomes positive again.

2.2 Mathematical Analysis of Weiser's Model with Constant Quantum Efficiency

The current–voltage relation at forward bias for the n-p^o-p structure of Fig. 1 was treated theoretically by Ashley and Milnes.[7] They determined that the pre-breakdown current–voltage relation across the p^o layer is

$$j = aV^2, \qquad [1]$$

where j is the current density, V is the voltage across the p^o layer (the total voltage across the material minus the voltage across the n-p^o junction), and a is a constant of the material. The current is carried by electrons and holes flowing toward the p^o-p junction (see Fig. 2), and some of the electrons that reach the p^o-p interface recombine radiatively with the holes of the p region. The flux density, f, of photons produced by radiative recombination is given by

$$f = \frac{\gamma j}{e}, \qquad [2]$$

where γ is the internal quantum efficiency for radiative recombination (≤ 1) and e is the electronic charge. A fraction ϕ of these photons are absorbed by filled acceptors of the p^o region, producing conduction electrons and holes bound to the acceptors. The rate of production of excess electrons per unit volume, Δn, is

$$\frac{d(\Delta n)}{dt} = \frac{\phi}{L} f - \frac{\Delta n}{\tau}, \qquad [3]$$

where L is the thickness of the p^o region and τ is the recombination life-time of conduction electrons. In Eq. [3], the first term is the rate

of absorption of recombination photons in the p°-region and the second term is the rate of decay of excess conduction electrons. On combining Eqs. [2] and [3], the rate at which excess electrons are produced is given by

$$\frac{d(\Delta n)}{dt} = \frac{\phi\gamma(j)}{Le} j - \frac{\Delta n}{\tau}, \qquad [4]$$

where $\gamma(j)$ implies that the quantum efficiency is a function of the current density.

If, at time zero, the current is that given by Eq. [1], the presence of the extra electrons produced by the absorbed recombination radiation will add an ohmic component to the current, since the extra holes are assumed to be *immobile*. The total current density will then be given by

$$j = aV^2 + \frac{\Delta n\, e\, \mu V}{L}, \qquad [5]$$

where μ is the electron mobility. On substitution of Eq. [5] into Eq. [4], the rate equation becomes

$$\frac{d(\Delta n)}{dt} = \frac{\phi\gamma(j)}{Le}\left(aV^2 + \Delta n\, e\, \mu \frac{V}{L}\right) - \frac{\Delta n}{\tau}. \qquad [6]$$

For the case of constant quantum efficiency, Eq. [6] reduces to

$$\frac{d(\Delta n)}{dt} = R + k\,\Delta n, \qquad [7]$$

where

$$R = \frac{\phi\gamma a V^2}{Le},$$

and

$$k = \frac{\phi\gamma\mu V}{L^2} - \frac{1}{\tau}.$$

The solution of Eq. [7] is well known, and is such that $\Delta n \longrightarrow \infty$ as

$t \longrightarrow \infty$ if $k > 0$, and Δn will reach a steady state value as $t \longrightarrow \infty$ if $k < 0$. For $k > 0$, excess electrons are produced at a rate faster than that at which they decay; for $k < 0$, the rates of production and decay of excess electrons approach the same constant value. From the definition of k, when $k = 0$, the critical voltage V_c is found to be

$$V_c = \frac{L^2}{\phi\gamma\mu\tau}. \qquad [8]$$

For voltages higher than V_c (i.e., $k > 0$), a regenerative process sets in. However, this regenerative process does not lead to a negative resistance, since it cannot be maintained at lower and lower voltages. Instead, a sufficient lowering of the voltage only leads to the case of $k < 0$.

2.3 Derivation of the Dark Threshold Voltage

The more general case of letting the quantum efficiency be a function of current density is carried out by using the simple form of dependence of γ on j suggested by Dumke,[5] that is,

$$\gamma = \frac{\gamma_\infty j}{j + b}. \qquad [9]$$

Substituting Eq. [9] into Eq. [4], the rate equation becomes

$$\frac{d(\Delta n)}{dt} = \frac{\phi\gamma_\infty j^2}{Le\,(j + b)} - \frac{\Delta n}{\tau}. \qquad [10]$$

The solution of Eq. [10] is greatly facilitated by assuming that at the threshold of negative resistance, the quantum efficiency depends strongly on the current density so that Eq. [9] is adequately approximated by

$$\gamma \approx \frac{\gamma_\infty j}{b}. \qquad [11]$$

Using the above assumption, and Eq. [5] for the current, Eq. [10] becomes

$$\frac{d(\Delta n)}{dt} = \frac{\phi\gamma_\infty}{Leb}\left(aV^2 + \Delta n\, e\,\mu\frac{V}{L}\right)^2 - \frac{\Delta n}{\tau}, \qquad [12]$$

or

$$\frac{d(\Delta n)}{dt} = u(\Delta n)^2 + v\,\Delta n + w, \qquad [13]$$

where

$$u = \frac{\phi\gamma_\infty e\,\mu^2 V^2}{bL^3}, \qquad [14]$$

$$v = \frac{2\,\phi\gamma_\infty a\,\mu V^3}{bL^2} - \frac{1}{\tau}, \qquad [15]$$

$$w = \frac{\phi\gamma_\infty a^2 V^4}{Leb}. \qquad [16]$$

Integration of Eq. [13] gives two types of solution, depending on whether

$$q \equiv (4uw - v^2) \qquad [17]$$

is greater or smaller than zero. The solution for $q < 0$ has the form

$$t = \frac{1}{\sqrt{-q}}\left[\log\frac{2u\,\Delta n + v - \sqrt{-q}}{2u\,\Delta n + v + \sqrt{-q}} - \log\frac{v - \sqrt{-q}}{v + \sqrt{-q}}\right]. \qquad [18]$$

For this solution, as t goes to infinity, Δn approaches a steady-state value equal to $(-v - \sqrt{-q})/(2u)$; hence, the solution of Eq. [13] for $q < 0$ does not lead to any drastic increase in current with time.

The solution for $q > 0$ has the form

$$t = \frac{2}{\sqrt{q}}\left[\tan^{-1}\frac{2u\,\Delta n + v}{\sqrt{q}} - \tan^{-1}\frac{v}{\sqrt{q}}\right]. \qquad [19]$$

In this case, Δn goes to infinity as $t \to \infty$; hence, the solution of Eq. [13] for $q > 0$ leads to a regenerative process that produces a negative resistance in the presence of an external series resistance. For the condition $q = 0$, a threshold voltage can be derived using Eqs. [14]

to [17]. The result is

$$V_{th} = \left(\frac{bL^2}{4\,\phi\gamma_\infty\, a\,\mu\,\tau} \right)^{1/3}. \qquad [20]$$

The physical meaning of the above results may be described as follows. Below the threshold voltage of Eq. [20] (i.e., $q < 0$), the generation and decay rates of excess electrons approach the same constant value, and therefore, a steady-state current is reached. When the threshold voltage of Eq. [20] is exceeded ($q > 0$), the generation rate of excess carriers is greater than their decay rate, so that the current rises with time. From Eq. [9], however, a rise in current leads to an increasing quantum efficiency; from Eq. [6], as the quantum efficiency increases, the voltage necessary to maintain the critical generation rate can be reduced. A negative-resistance region sets in, and continues until the quantum efficiency becomes constant, that is, when the critical voltage of Eq. [8] is reached.

2.4 Derivation of the Threshold Voltage for External Illumination

Since the negative resistance is brought about by the generation of electrons in the p^o region by light given off at the p^o-p boundary, it is expected that external illumination would tend to lower the threshold voltage. Again making the assumption that the light is uniformly absorbed in the p^o layer, the rate equation may be written to take into account the presence of external illumination of intensity I. Thus, Eq. [4] becomes

$$\frac{d(\Delta n)}{dt} = \frac{\phi\,\gamma\,(j)}{Le} - j - \frac{\Delta n}{\tau} + \alpha\, I, \qquad [21]$$

where I is given in photons/cm^2/sec, and α is the absorption coefficient (cm^{-1}) of the p^o region. Using Eq. [11] for the quantum efficiency, and Eq. [5] for the current, Eq. [21] becomes

$$\frac{d(\Delta n)}{dt} = \frac{\phi\gamma_\infty}{Leb}\left(aV^2 + \Delta n e\,\mu\,\frac{V}{L} \right)^2 - \frac{\Delta n}{\tau} + \alpha\, I, \qquad [22]$$

or

$$\frac{d(\Delta n)}{dt} = u(\Delta n)^2 + v(\Delta n) + w + \alpha I. \qquad [23]$$

Setting

$$w' = w + \alpha I, \qquad [24]$$

integration of Eq. [23] gives two types of solution, depending on whether

$$q' \equiv (4uw' - v^2) \qquad [25]$$

is greater or smaller than zero. The analysis of the two solutions is the same as that given in the previous section.

The critical value of voltage, (threshold voltage, $V_{th(I)}$) with light of intensity I incident on the material is obtained by setting $q' = 4uw' - v^2$ equal to zero, and by using Eq. [24] for w' and Eqs. [14] to [16] for u, v, and w. The relation between $V_{th(I)}$ and I is found to be

$$I = \frac{bL^3}{4\phi\gamma_\infty e\mu^2\tau^2 (V_{th(I)})^2}\left[1 - \frac{4\phi\gamma_\infty \mu\tau\alpha (V_{th(I)})^3}{bL^2}\right]. \qquad [26]$$

Making use of Eq. [20], and

$$j_{th} = \alpha V_{th}^2 \qquad [27]$$

which, from Eq. [1], is approximately the current density at the dark threshold voltage, Eq. [26] reduces to

$$I = \frac{V_{th} j_{th} L}{\alpha e \mu \tau (V_{th(I)})^2}\left[1 - \left(\frac{V_{th(I)}}{V_{th}}\right)^3\right] \qquad [28]$$

This expression relates $V_{th(I)}$, the threshold voltage in the presence of external illumination, to I, the incident light intensity. It may be observed that $V_{th(I)}$ is proportional to $I^{-1/2}$ in the case where the light intensity is high enough so that the threshold voltage is reduced considerably, that is, when the term in brackets in Eq. [28] can be neglected.

The physical meaning of Eq. [28] may be described as follows. When external illumination of intensity I is incident on the material, and when the voltage applied across the material is less than $V_{th(I)}$, then $q' < 0$, and the generation and decay rates of excess electrons approach the same constant value. Therefore, the current approaches a steady-state value. When external illumination of intensity I is incident on the material, and when the threshold voltage, $V_{th(I)}$, of Eq. [28] is exceeded, then $q' > 0$, and the generation rate of excess carriers is greater than their decay rate, so that the current rises with time. From Eq. [9], however, a rise in current leads to an increasing quantum efficiency; hence, the voltage necessary to maintain the critical generation rate can be reduced. A negative-resistance region sets in, and continues until the quantum efficiency becomes constant. Eq. [28] is an extremely important result, since it provides a simple method of comparing theory with experimental observations of negative resistance.

3. Dependence of $V_{th(I)}$ on I—Variations in the Current Equation and the Quantum Efficiency

The results of Weiser's theory were derived using Eq. [21], the rate equation for the production of excess electrons; Eq. [11], an approximate dependence of quantum efficiency on current; and Eq. [5], the current equation,

$$j = aV^2 + \frac{\Delta n e \mu V}{L}. \qquad [5]$$

In Eq. [5], the first term corresponds to the pre-breakdown current in the material. Weiser selected a square-law dependence for the pre-breakdown current, aV^2, because this type of current–voltage characteristic occurs in the model he investigated. The second term of Eq. [5] is the photocurrent produced by the absorption of radiation.

If Weiser had selected a different model on which to carry out his investigation, the pre-breakdown current and the photocurrent of Eq. [5] also would have been different. This changes the result obtained for the dark threshold voltage, Eq. [20], and the relationship between external light intensity and the threshold voltage, Eq. [28]. In order to determine the sensitivity of these relations to variations in the current equation and the quantum efficiency, the analysis described in the preceding section was carried out for several variations of pre-breakdown current, photocurrent, and quantum efficiency. The results are given in Table 1 and summarized in Table 2.

Table 1—Relations Between Threshold Voltage and Light Intensity

γ	Photocurrent	j	V_{th}	I
$\gamma_e j/b$	$\Delta ne\mu V/L$	$aV^i + \Delta ne\mu V/L$	$\left[\frac{L^2 b}{4a\phi\gamma_e\mu\tau}\right]^{1/(i+1)}$	$\frac{V_{th} j_{th} L}{\alpha e\mu\tau V_{th(I)}^2}\left[1-\left(\frac{V_{th(I)}}{V_{th}}\right)^{i+1}\right]$
$\gamma_e j/b$	ΔncV^2	$aV^i + \Delta ncV^2$	$\left[\frac{Leb}{4ac\phi\gamma_e\tau}\right]^{1/(i+2)}$	$\frac{V_{th}^2 j_{th}}{c\alpha\tau V_{th(I)}^4}\left[1-\left(\frac{V_{th(I)}}{V_{th}}\right)^{i+2}\right]$
$\gamma_e j^2/b$	$\Delta ne\mu V/L$	$aV^i + \Delta ne\mu V/L$	$\left[\frac{4L^2 b}{27a^2\phi\gamma_e\mu\tau}\right]^{1/(2i+1)}$	$\frac{V_{th}^{1/2} j_{th} L}{\alpha e\mu\tau V_{th(I)}^{3/2}}\left[1-\left(\frac{V_{th(I)}}{V_{th}}\right)^{(2i+1)/2}\right]$
$\gamma_e j^2/b$	ΔncV^2	$aV^i + \Delta ncV^2$	$\left[\frac{4Leb}{27a^2c\phi\gamma_e\tau}\right]^{1/(2i+2)}$	$\frac{V_{th} j_{th}}{c\alpha\tau V_{th(I)}^3}\left[1-\left(\frac{V_{th(I)}}{V_{th}}\right)^{i+1}\right]$

$i = 1, 2, 3$

From Table 1, it is noted that the main dependence of the threshold voltage $V_{th(I)}$ on the external light intensity I is determined by the photocurrent term and the quantum efficiency; the exponent of the correction term (the term in brackets) is controlled by the pre-breakdown current. From the summary of Table 2, it is noted that the main dependence of $V_{th(I)}$ on I is strong enough so that there is no difficulty in determining which relationship of the table gives best agreement with observation.

Table 2—Summary of Relations Between Threshold Voltage and Light Intensity

Quantum Efficiency	Photocurrent	$V_{th(I)}$, Threshold Voltage, Proportional To
$\approx \gamma_x j/b$	$= \Delta n\ e\ \mu V/L$	$I^{-1/2}$
$\approx \gamma_x j/b$	$= \Delta n\ c\ V^2$	$I^{-1/4}$
$\approx \gamma_x j^2/b$	$= \Delta n\ e\ \mu V/L$	$I^{-2/3}$
$\approx \gamma_x j^2/b$	$= \Delta n\ c\ V^2$	$I^{-1/3}$

Measurements of threshold voltage versus light intensity have been carried out on CdSe powder that exhibits negative resistance. The results are compared with theory in Section 5, and it is found that the best agreement is obtained for $V_{th(I)}$ proportional to $I^{-1/2}$.

4. Methods and Procedures Used in the Experimental Investigation

The method of observing the current–voltage characteristic of CdSe in the dark is illustrated in Fig. 3. The circuit is shown simply as a series circuit with a dc-voltage source, an ammeter, and the CdSe sample. In Fig. 3, the current axis denotes the current through the circuit; the voltage axis depicts the voltage across the CdSe sample *only*. If the voltage across the sample–ammeter combination is increased from zero, at first there is no measurable current through the sample. When the voltage across the material reaches the threshold voltage V_{th}, the current rises rapidly while the voltage across the sample decreases. This is the negative-resistance region, and is indicated by the line with negative slope in Fig. 3. The passage through the negative-resistance region is so rapid that a point-by-point obser-

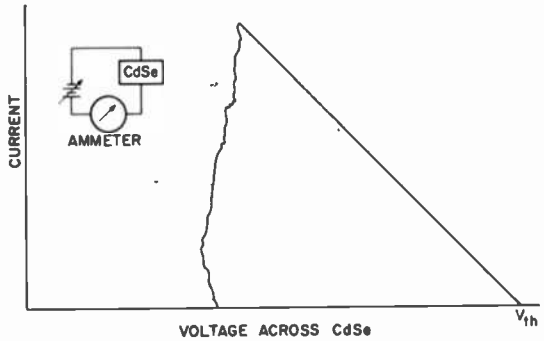

Fig. 3—Current–voltage characteristic of CdSe in the dark.

vation of the current–voltage characteristic in this region cannot be made. At the uppermost part of the curve, the negative-resistance region ceases because of the resistance limitation provided by the ammeter. Without this resistance limitation, the current goes to such a high level that the sample is destroyed. At the point of highest current, the total voltage is still V_{th}, even though the voltage across the sample has decreased. The difference in voltage appears across the ammeter. If the voltage across the combination is decreased, the current decreases in the noisy fashion shown in the figure. After the current reaches zero, the process may be repeated.

When the CdSe sample is illuminated with light, the threshold voltage is reduced. In Fig. 4, the lowering of the threshold voltage is illustrated for three different light intensities. From Figs. 3 and 4, it may be noted that CdSe is a good insulator before the threshold voltage is reached.

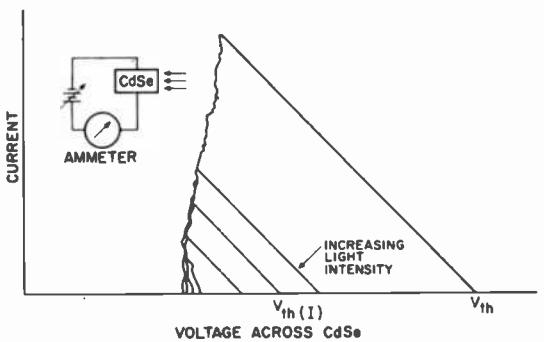

Fig. 4—Current–voltage characteristic of CdSe with light incident.

4.1 Experimental Setup

The experimental setup used to measure the threshold voltage of CdSe powder as a function of light intensity is illustrated in Fig. 5. The light intensity at the exit slit of the monochromator as a function of wavelength was measured using a calibrated phototube. This equipment was also used to calibrate the transmission of various neutral density filters as a function of wavelength. The voltage across the CdSe sample was measured by subtracting the voltage across terminals B from the total voltage across terminals A. This voltage, A minus B, was recorded as the x-coordinate on an X-Y recorder. The voltage across the B terminals was proportional to the current through the CdSe, and was recorded as the y-coordinate on the X-Y recorder.

4.2 Samples

The CdSe samples used in the experiments were prepared by stretching a 10-mil copper wire over a piece of glass with ten strips of transparent, conductive tin oxide coated on the surface. The strips of tin oxide were 0.010 inch wide, separated by 0.040 inch, and were placed perpendicular to the copper wire. In this way, ten samples were made in each setup. The spacing between the wire and the glass was set at 100 μm (0.004 inch), and the copper wire and the conductive coating of the glass provided the electrodes for the small amount of CdSe powder dropped between them. The particle size of the CdSe powder was of the order of 50 μm in diameter.

4.3 Experimental Procedure

Measurements of threshold voltage versus light intensity were carried out for two wavelengths: 7000 and 9000 Å. The monochromator of Fig. 5 was set at one of these wavelengths, and the light from the exit slit was allowed to fall on the CdSe sample. The sample was positioned so that the light emerging from the exit slit fell where the material made contact with the conductive coating of the glass. The absorption due to the glass and the conductive coating was measured before preparing the samples, and thus it was taken into account in determining the incident light intensity. The intensity of the light incident on the sample was varied by placing the various prevously calibrated neutral density filters between the exit slit and the CdSe. With the light incident on the sample, the voltage across it was increased from zero until the threshold was reached. The material passed through the

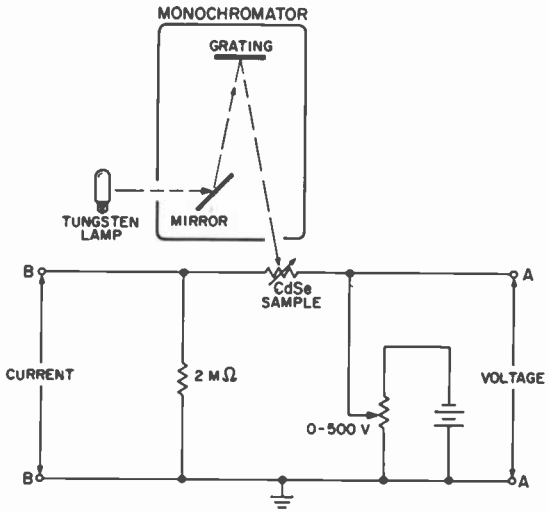

Fig. 5—Experimental setup for measuring the threshold voltage of CdSe powder as a function of light intensity.

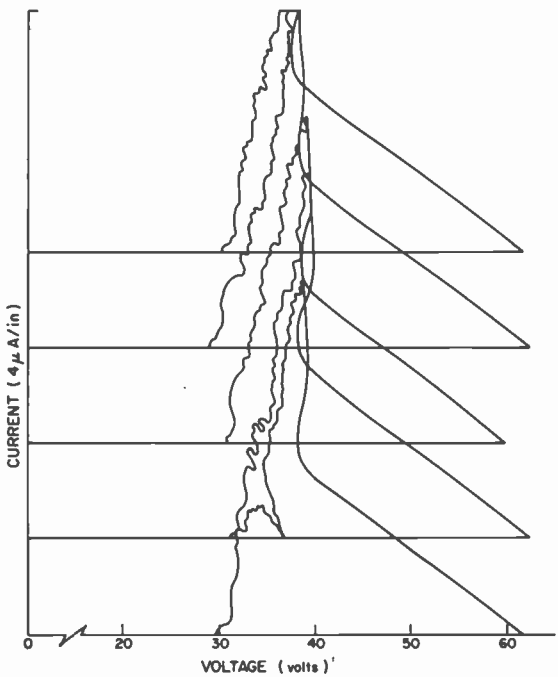

Fig. 6—Measurement of threshold voltage with light incident on the sample ($\lambda = 9000$ Å, $I = 1.06 \times 10^{11}$ photons/cm^2/sec).

negative-resistance region rapidly, then the voltage was returned slowly to zero. This process was repeated five times for each intensity.

Fig. 6 shows an example of the measurement of $V_{th(I)}$ with light of intensity I incident on the sample. For each of the five measurements, the zero-axis of current on the X-Y recorder was shifted. From Fig. 6 it is observed that, below about 30 volts, no measurable current passes through the sample either before or after breakdown. This was always found to be the case, except under conditions of extremely high light intensity (room light or direct light from the tungsten source incident on the sample). Under these conditions, the negative resistance disappeared. However, even with the disappearance of negative resistance for high light intensities, 21 volts still had to be applied across the sample before a measurable current would flow. The value of 21 volts (the average of 25 readings) was therefore taken to be the junction bias voltage. In the example of Fig. 6, the value of $V_{th(I)}$ is about 40 volts (total voltage minus junction bias voltage). This method of determining $V_{th(I)}$ was used in all measurements of the threshold voltage.

In summary, for the wavelengths 7000 and 9000 Å, the incident light intensity was varied by placing various neutral density filters between the exit slit of the monochromator and the CdSe sample. The value of $V_{th(I)}$ was averaged over five readings, and the result was a measure of $V_{th(I)}$ versus I. The results are given in the next section, where they are analyzed in terms of the theory of negative resistance presented in Sections 2 and 3.

5. Measurements of Threshold Voltage Versus Incident Light Intensity

5.1 Results

The results of the measurements at 7000 and 9000 Å are plotted on a log-log scale in Fig. 7. Although each data point of Fig. 7 is the average of five readings, error bars are not included since the maximum variations in $V_{th(I)}$ were of the order of only ±2 volts.

5.2 Comparison of Results with Theory

In Section 2, it was shown that in order for a material with negative resistance to conform to Weiser's theory, measurements of threshold voltage as a function of light intensity must agree with the relation

$$I = \frac{V_{th}\, j_{th}\, L}{\alpha e\, \mu\tau\, (V_{th(I)})^2}\left[1 - \left(\frac{V_{th(I)}}{V_{th}}\right)^3\right]. \qquad [28]$$

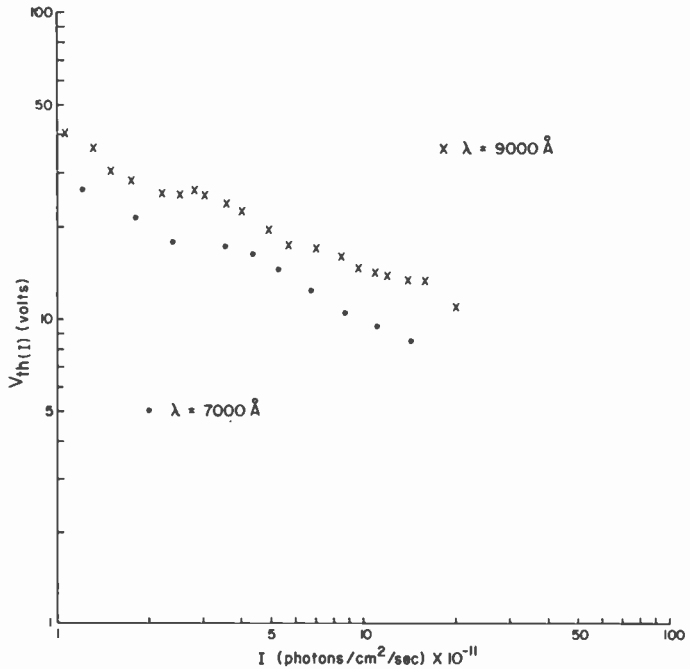

Fig. 7—Threshold voltage versus light intensity.

When the light intensity is high enough so that the threshold voltage $V_{th(I)}$ is considerably reduced in comparison to the dark threshold voltage V_{th}, the term in brackets in Eq. [28] may be neglected. Then $V_{th(I)}$ is proportional to $I^{-1/2}$. This corresponds to the case where the injected current is negligible compared to the number of electrons supplied to the conduction band by absorption of external radiation. According to the theory, such a situation should yield a slope of $-\frac{1}{2}$ on a log-log plot of $V_{th(I)}$ versus I. A linear regression (least squares) analysis was carried out for the two sets of data of Fig. 7. The slopes of best fit were found to be -0.453 for $\lambda = 7000$ Å and -0.416 for $\lambda = 9000$ Å.

The values of slopes obtained from Fig. 7 may be low compared to the theoretical value because several of the measurements were made at relatively low light intensities. In order to investigate the effect of the measurements made at low light intensity, the term in brackets in Eq. [28] should be included. This is accomplished by plotting $V_{th(I)}/[1-(V_{th(I)}/V_{th})^3]^{1/2}$ versus I on a log-log scale. The plot is given in Fig. 8, where the solid lines have the theoretical slope

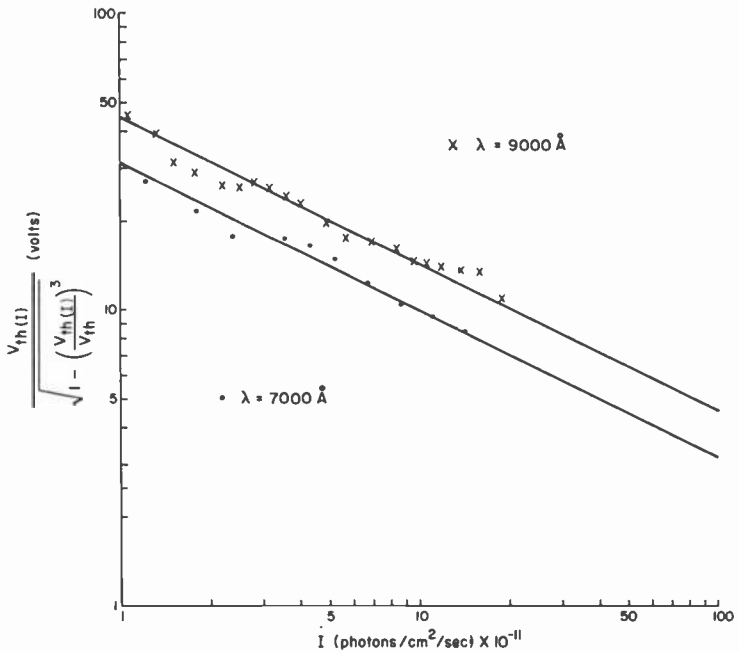

Fig. 8—Threshold voltage versus light intensity—comparison with Weiser's theory.

of $-\frac{1}{2}$. A dark threshold voltage of 69 volts (the average of 25 measurements) was used in the data of Fig. 8.

A linear regression (least squares) analysis was carried out for the two sets of data of Fig. 8. The slope of best fit was found to be -0.465 at 7000 Å and -0.441 at 9000 Å. The agreement between these measured values and the theoretical value of $-\frac{1}{2}$ is considered to be good.

Before concluding that the negative-resistance effect in CdSe powder may be interpreted in terms of Weiser's theory, further consideration will be given to the experimental results in terms of the relationships developed in Section 3. There it was shown that the relationship between the external light intensity and the threshold voltage is sensitive to variations in the quantum efficiency and the current equation. Twelve different relationships between external light intensity and the threshold voltage, including Eq. [28], were derived. These are given in Table 1. By studying these relationships in conjunction with the raw data plotted in Fig. 7, it was found that the best fit for the data is obtained with

$$I = \frac{V_{th} j_{th} L}{\alpha e \mu \tau V_{th(I)}^2} \left[1 - \left(\frac{V_{th(I)}}{V_{th}} \right)^2 \right]. \qquad [29]$$

In deriving Eq. [29], the initial current was considered to be ohmic (aV) instead of following the square-law dependence (aV^2) used in obtaining Eq. [28].

Table 3—Results of Linear Regression Analyses

Quantities Analyzed: log f ($V_{th(I)}$) versus log I	$\lambda = 7000$ Å		$\lambda = 9000$ Å	
$f(V_{th(I)})$	Slope of Best Fit	% Difference From Theoretical Slope of $-\frac{1}{2}$	Slope of Best Fit	% Difference From Theoretical Slope of $-\frac{1}{2}$
$V_{th(I)}$	-0.453	9.4	-0.416	16.8
$\dfrac{V_{th(I)}}{\left[1 - \left(\dfrac{V_{th(I)}}{V_{th}} \right)^3 \right]^{1/2}}$	-0.465	7.0	-0.441	11.8
$\dfrac{V_{th(I)}}{\left[1 - \left(\dfrac{V_{th(I)}}{V_{th}} \right)^2 \right]^{1/2}}$	-0.482	3.6	-0.468	6.4

For agreement to exist between theory and experiment, a plot of log of $V_{th(I)}/[1-(V_{th(I)}/V_{th})^2]^{1/2}$ versus log I should yield a straight line with slope of $-\frac{1}{2}$ for the measurements at each wavelength. The plots are not given since they differ little from those given in Figs. 7 and 8. However, the slope of best fit was found to be -0.482 at 7000 Å and -0.468 at 9000 Å. The results of the experimental investigation are summarized in Table 3. From the table it is observed that a better fit is obtained between the threshold data and Eq. [29], than is obtained between the threshold data and Eq. [28], the relationship derived in Weiser's theory.

5.3 Conclusions

The Dumke-Weiser theory of negative resistance was formulated in order to account for the current–voltage characteristic of GaAs p-i-n junctions. The experimental results presented above verify the validity of the theory for another insulating material, namely, CdSe powder.

In attempting to explain the experimental results with CdSe on the basis of the same mechanism as that proposed by Dumke and Weiser, the effect of varying the functional dependencies of the initial current, the photocurrent, and the quantum efficiency was determined. The best fit of the experimental data for CdSe was found to occur for a linear dependence of the initial current on voltage, rather than the quadratic dependence that was appropriate for the GaAs results. It should be pointed out that a direct observation of the initial current was not possible (see Fig. 6). The functional dependencies of the photocurrent and the quantum efficiency that gave the best fit were the same for both materials.

The displacement of the two sets of data in Figs. 7 and 8 occurs because of the difference in absorption coefficient for the two wavelengths. This conclusion is based on experimental observations that will be presented in a future paper in which threshold data will be used to determine the absorption coefficient of CdSe as a function of wavelength.

Acknowledgments

The authors wish to acknowledge the contributions of J. Vollmer, D. J. Woywood, J. J. Rudnick, L. J. Krolak, and F. E. Shashoua, of Advanced Technology Laboratories; S. A. Harper and F. J. Hinnenkamp, of the Electronic Components and Devices Division; P. Mark of Princeton University; and W. P. Dumke of the IBM Watson Research Center.

References:

[1] F. H. Nicoli, "A Hysteresis Effect in Cadmium Selenide and Its Use in a Solid-State Image Storage Device," **RCA Rev.**, Vol. 19, p. 77 (1958).
[2] F. J. Hinnenkamp, **Hysteresis in Cadmium Selenide,** M.S Thesis, Franklin and Marshall College, Lancaster, Pennsylvania, April, 1966.
[3] R. W. Smith, Private Communication.
[4] W. P. Dumke, "Theory of Negative Resistance in GaAs pin Diodes," **Bull. Am. Phys. Soc.**, Vol. 9, p. 217 (1964).
[5] W. P. Dumke, "Theory of the Negative Resistance in P-I-N Diodes," **Proc. 7th International Conf., Phys. of Semiconductors,** Dunod, Paris (1964); p. 611.
[6] K. Weiser, "Properties of GaAs Diodes with P-P^{o}-N Structures," **IBM J. Res. Dev.**, Vol. 9, p. 315 (1965).
[7] K. L. Ashley and A. G. Milnes, "Double Injection in Deep-Lying Impurity Semiconductors," **J. Appl. Phys.**, Vol. 35, p. 369 (1964).

Luminescence from GaN MIS Diodes

J. I. Pankove and P. E. Norris
RCA Laboratories, Princeton, N. J.

Abstract—A high electric field is used to generate holes at the surface of n-type GaN; a reversal of the electric field polarity allows radiative recombination to occur over a broad spectrum, including the ultraviolet, due to near-band transitions.

Introduction

MIS luminescent diodes have been made with GaAs[1] and GaP[2]. The structure consists of a metal electrode spaced from the semiconductor by a thin insulating layer. A second metallic connection provides an ohmic contact to the semiconductor. Because the most interesting phenomena occur in the vicinity of the metal-insulator-semiconductor region, the second (ohmic) metal electrode is omitted from the acronym, "MIS."

The principle of operation of the MIS diode is as follows. A transient voltage is applied across the diode to induce an inversion layer in the semiconductor at the IS interface. A negative voltage is applied to the metal to invert the n-type material, and conversely, a positive voltage to invert a p-type semiconductor. The inversion concentrates minority carriers at the surface of the semiconductor. Then, the polarity of the bias is reversed to "inject" the minority carriers from the surface into the bulk of the semiconductor.

Injection luminescence can be easily studied without resorting to the MIS structure in those semiconductors in which p-n junctions can be readily fabricated. But in those materials in which p-n junctions have not or cannot be made, minority carrier injection can be accomplished only by the use of either the MIS structure or a Schottky barrier. Since we have not been able to make p-type GaN and have not obtained electroluminescence from a Schottky barrier to n-type GaN,[3] the MIS structure was tried.

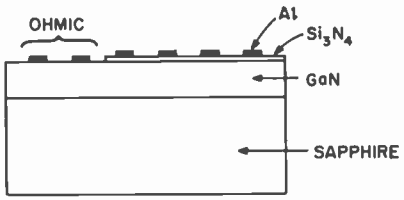

Fig. 1—Structure of an array of MIS diodes.

MIS Fabrication

A 1000-Å layer of Si_3N_4 was deposited on GaN by reacting silane with ammonia at ~700°C. Then 20-mil-diameter dots of Al were evaporated onto the Si_3N_4 layer to form MIS diodes (Fig. 1). The ohmic contact to the GaN was provided by Al dots evaporated over a bare region of GaN. The ohmicity of these contacts could be verified by measuring the $I(V)$ characteristics between any two dots on the bare GaN. The "undoped" n-type GaN, grown by the vapor-transport method,[4] had a carrier concentration of 3.9×10^{18} electrons/cm^3 and a mobility of 137 cm^2/Vsec.

Electrical Characteristics

The $I(V)$ characteristics of the MIS structure showed symmetrical breakdown at about ±50 V. This breakdown corresponds to Frankel–Poole conduction in the Si_3N_4 when a critical field of 5×10^6 V/cm is achieved.[5] It was noted that the MIS diode always "burned out" when more than about 5 μA were passed through the contact with the "metal" (field-effect electrode) negative, whereas a larger current could usually be tolerated with the metal positive. Burnout rendered the MIS contact ohmic.

A negative bias on the metal causes double injection in the insulator

and therefore a negative resistance is expected, whereas a positive bias on the metal transfers electrons from the conduction band of GaN to the conduction band of Si_3N_4, and from there to the metal. Hole injection from the positively biased metal to Si_3N_4 is probably inefficient because of the higher barrier to holes (3.05 eV) than to electrons (2.1 eV) at the MI interface.[6] However, some holes are injected at the MI interface as evidenced by the cw emission of radiative recombination during positive breakdown bias of a few microamperes. The expected onset of negative resistance would explain the greater vulnerability to burnout with a negative bias.

$C(V)$ measurements were made with a 1-MHz small signal superimposed on a swept dc bias. The zero-bias capacitance was 90 pF. As shown in Fig. 2, the capacitance decreases when the bias is negative,

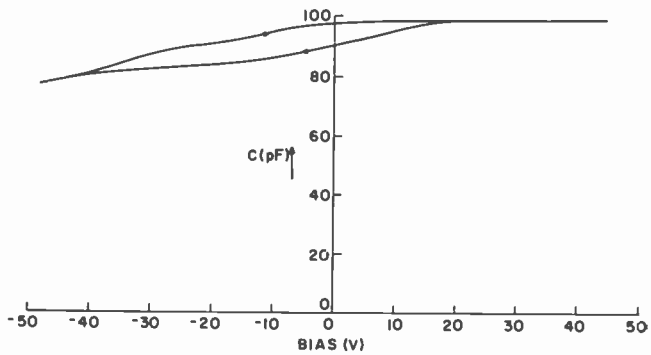

Fig. 2—$C(V)$ characteristic of MIS diode.

as expected from the generation of a depletion region. However, the hysteresis in the $C(V)$ curve and its shallow slope indicate the presence of trapping states at the GaN/Si_3N_4 interface. From the sense of the hysteresis, it appears that electron extraction or hole trapping occurs at the interface.[7] The broad step-like structure at about −20 V suggests the presence of two sets of surface states.

Luminescence

The following luminescence experiments were performed at fields lower than the breakdown field of Si_3N_4 (5×10^6 V/cm). Holes were generated at the IS interface by applying a sudden negative (~40 V) bias to the metal electrode (Fig. 3a). This polarization caused an upward bending of the bands, which produced a surface inversion layer. The

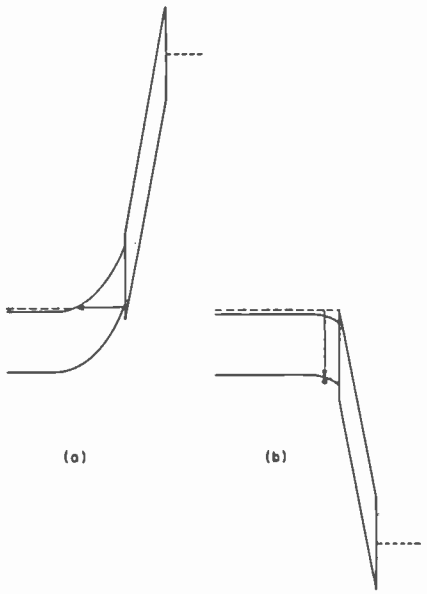

Fig. 3—Band structure at MIS transition (a) with metal negatively biased for hole generation and (b) with metal positively biased for recombination.

inversion layer traps the holes generated either by field emission or by a combination of thermal and field emission of electrons from the valence band at the surface to the conduction band in the bulk. Then, the bias was reversed (metal driven positive) to allow electron–hole recombination at the surface (Fig. 3b).

This bipolar pulse was produced by two synchronized pulsers, one generating a negative pulse and the other generating a positive pulse at the end of the negative pulse, as shown in Fig. 4. Because of impedance mismatch between the generator and the MIS load, the square

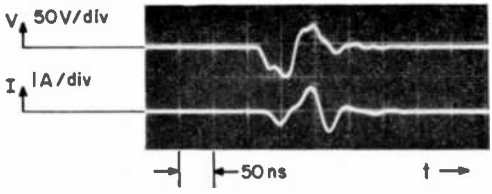

Fig. 4—Voltage and current waveforms of driving signal. The current waveform is delayed by 25 ns with respect to the voltage (this is an instrumental effect).

waves are greatly distorted. The current through the diode is also shown in Fig. 4. As expected, light is emitted when the metal electrode is biased positively. It was noted that the intensity of the light did not depend on the duration of either the negative or of the positive pulses, provided the duration exceeded a minimum value of 60 ns. Below 60 ns, the intensity of the pulses decreased, causing a corresponding drop in luminescence. The luminescence intensity, however, depended critically on the delay or overlap of the two pulses. The highest output was obtained when the positive current was maximized corresponding to the fastest possible polarity reversal. The light emitted was too weak to conveniently display its waveform on an oscilloscope.

The emission spectrum (Fig. 5) forms a broad band extending below 3.4 eV and consists of a peak at 3.28 eV and another one more intense at 2.10 eV. These two peaks are joined by a broad structureless emission spectrum.

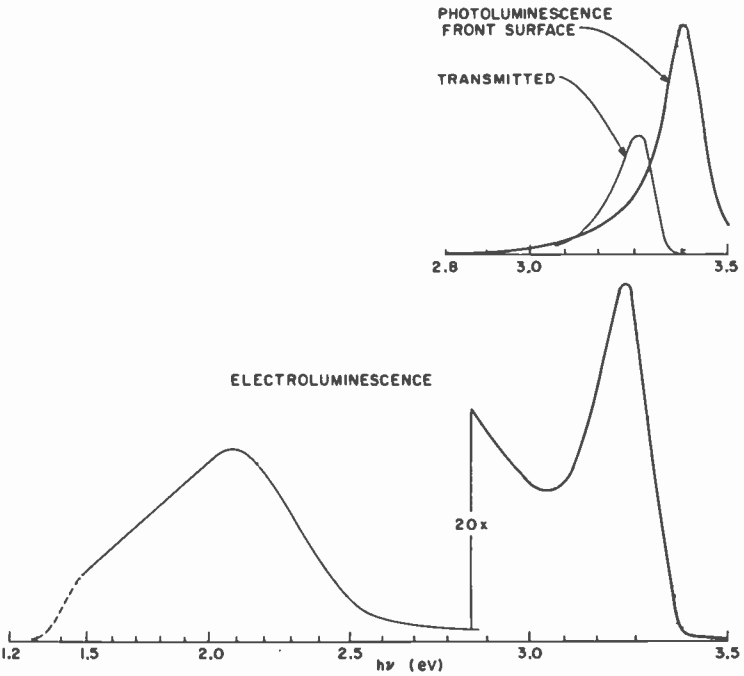

Fig. 5—Electroluminescent emission spectrum during bipolar biasing of the MIS diode. The dashed portion of the low energy peak is a cutoff due to the detector's characteristics. The upper two curves are the photoluminescent spectra obtained from the front (excited) face and after transmission through the material.

The near-edge photoluminescence spectra obtained with an He-Cd UV laser are shown in the inset of Fig. 5. One spectrum was obtained by measuring the light emitted from the illuminated side; the other spectrum was obtained by measuring the light transmitted through the crystal. It is evident that the shift of the emission peak from 3.395 to 3.31 eV is caused by the high energy cutoff of the radiation transmitted by the GaN crystal due to the extensive absorption edge of this material. This observation suggests that self-absorption may play an important role in clipping the high energy edge of the radiation emitted by the MIS structure. A transmission measurement shows that the absorption coefficient is greater than 10^3 cm^{-1} at 3.40 eV and is rising rapidly at higher photon energies. Hence, it is expected that the emission under the contact may be a very intense near-gap emission.

Acknowledgment

We are grateful to E. A. Miller for growing the GaN, to M. T. Duffy for depositing the Si_3N_4 film, to J. E. Berkeyheiser for assistance with the measurements, and to A. M. Goodman and H. Kressel for valuable discussions.

References:

[1] C. N. Berglund, "Electroluminescence Using GaAs MIS Structures," **Appl. Phys. Lett.**, Vol. 9, p. 441 (1966).
[2] F. E. Harper and W. J. Bertram, "Theory and Experiments on an Electroluminescent Device Constructed in the Metal-Insulator-Semiconductor Geometry," **IEEE Trans. Elec. Dev.**, Vol. 16, p. 641 (1969).
[3] J. I. Pankove, J. E. Berkeyheiser, H. P. Maruska, and J. P. Wittke, "Luminescent Properties of GaN," **Solid State Comm.**, Vol. 8, p. 1051 (1970).
[4] H. P. Maruska and J. J. Tietjen, "The Preparation and Properties of Vapor-Deposited Single-Crystalline GaN," **Appl. Phys. Lett.**, Vol. 15, p. 327 (1969).
[5] A. M. Goodman, E. C. Ross, and M. T. Duffy, "Optimization of Charge Storage in the MNOS Memory Device," **RCA Rev.**, Vol. 31, p. 342 (1970).
[6] A. M. Goodman, "Photoemission of Electrons and Holes into Silicon Nitride," **Appl. Phys. Lett.**, Vol. 13, p. 275 (1968).
[7] K. H. Zaininger and F. P. Heiman, **Solid State Tech.**, Vol. 13, No. 5, p. 49 and No. 6, p. 46 (1970).

Infrared Transmission Microscopy Utilizing a High-Resolution Video Display

Richard A. Sunshine and Norman Goldsmith

RCA Laboratories, Princeton, N. J.

Abstract—This paper demonstrates that an infrared miscroscope having particularly good sensitivity for defects in silicon is obtained by combining a silicon vidicon television camera with a standard miscroscope objective, low-intensity light source, and a video monitor. The rapid fall in response of the silicon vidicon at wavelengths approaching the bandgap of silicon results in enhanced contrast when using white-light illumination sources. Resolution of the system is excellent because it is limited only by the microscope objective. The usefulness of this simple apparatus is illustrated by photographs taken quickly and nondestructively showing doping variations, precipitates, and decorated dislocations in semiconductor materials and devices.

Introduction

A large variety of techniques have been developed to detect and identify defects in semiconductor materials and devices. However, few of these techniques are at once simple, rapid, and nondestructive so as to be used to routinely monitor defects introduced or present in the material. Here we describe a simple, nondestructive, and relatively inexpensive apparatus for examining semiconductor samples by means of high-contrast, high-resolution infrared transmission microscopy. In

addition, we demonstrate the usefulness of this technique by directly viewing and photographing within a wafer many features that are normally found only by destructive etching and staining techniques or time consuming x-ray topography.

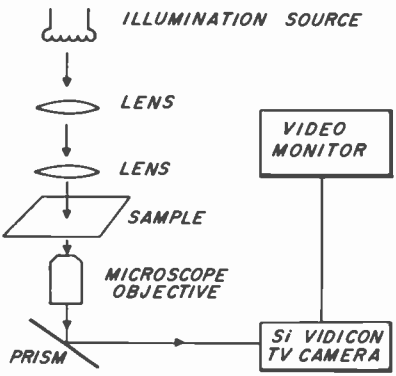

Fig. 1—Experimental apparatus used in this investigation.

Experimental Arrangement

The experimental arrangement is extremely simple, as can be seen from Fig. 1. A low-power microscope lamp is used to illuminate the sample, which is placed on a stage capable of x-y-z motion. The light passing through the sample is focused, using a standard microscope objective, onto the target of a silicon vidicon television camera. The image is viewed or photographed from a video monitor. The magnification can be changed by changing the objective lens, the distance between the vidicon camera and the objective, or the video monitor size. Changing the camera distance allows one to "zoom in" on a defect of particular interest. This system has several significant advantages over conventional image converter microscopes[1] and laser scanning systems.[2] Some of these are

[1] The silicon vidicon responds to light with wavelengths as long as 1.10 μm, allowing the use of low-power illumination sources for viewing silicon samples.

[2] Standard video circuitry is used resulting in an image of good contrast, adequate grey scale and easy viewing.

[3] The spatial resolution is excellent. We have resolved features less than 2 μm in size without the use of infrared corrected optics.

[4] The magnification is simply and conveniently adjusted.
[5] There are no critical alignments or moving parts such as are used with a laser scanning system.
[6] The components are relatively inexpensive, widely available, and as convenient to use as a conventional metallurgical microscope.
[7] There is no severe barrel distortion, as in image converter microscopes, and no "grain" due to magnification of a phosphor screen.

Contrast and Spectral Response

There are a number of factors that contribute to the production of a clearly defined image of defects and surface features using this system. For examining samples of silicon the system is almost ideally matched as shown by the following analysis.

The transmission through a polished sample of material thickness x_s, absorption coefficient α_s, and reflection coefficient R, is given by[3]

$$T = \frac{(1-R)^2 \exp(-\alpha_s x_s)}{1 - R^2 \exp(-2\alpha_s x_s)}. \qquad [1]$$

In general, T will be a function of wavelength. For the case of a silicon sample, $R \simeq 0.3$, so that to a reasonable approximation the second term in the denominator can be dropped. Thus the transmission through the sample can be written,

$$T_s = A \exp(-\alpha_s x_s) \qquad [2]$$

where A is a constant. The sensitivity S of the silicon vidicon is proportional to the ligh absorbed in the silicon target. If B is the proportionality constant and α_v and x_v are the absorption coefficients and thickness of the vidicon target, then

$$S = B\,[1 - \exp(-\alpha_v x_v)]. \qquad [3]$$

The response of the system is then

$$R^* = ST_s = AB\,[\exp(-\alpha_s x_s)]\,[1 - \exp(-\alpha_v x_v)]. \qquad [4]$$

It is convenient to introduce new variables

$$y = \alpha_s x_s \text{ and } \delta = \frac{\alpha_v x_v}{\alpha_s x_s}. \qquad [5]$$

The response can then be written

$$R^* = AB \exp(-y)\,[1 - \exp(-\delta y)]. \qquad [6]$$

We now find the value of y for which the response is a maximum. Differentiating R with respect to y and setting the result equal to zero gives

$$y_m = \frac{1}{\delta} \ln(1 + \delta). \qquad [7]$$

From Eq. [5], we see that for the normal range of silicon wafers, $\delta \ll 1$, since x_s/x_v will be in the range 8 to 40. In addition, since the vidicon is not heavily doped, $\alpha_v \leqslant \alpha_s$. Thus δ is less than 1, allowing Eq. [7] to be expanded to give

$$y_m = 1. \qquad [8]$$

For a typical sample thickness of 2×10^{-2} cm, the system will have maximum response for $\alpha = 50$ cm^{-1}, i.e., in a wavelength region near the absorption edge of silicon. The contrast ratio C observed for two adjacent regions will be given by the ratio of the response for each of these regions. From Eq. [4], we obtain

$$C = R_1^*/R_2^* = \exp(-\alpha_{s1}x_{s1})/\exp(-\alpha_{s2}x_{s2}) \qquad [9a]$$

$$\ln C = \alpha_{s2}x_{s2} - \alpha_{s1}x_{s1} \qquad [9b]$$

If the values of x_s are the same, a contrast ratio of two will be obtained when the difference between the α's is 30 cm^{-1} for a thickness of 2×10^{-2} cm. Examination of the absorption edge of silicon[4] (the region in which the system has appreciable response) will show that this difference is easily obtained for small differences in doping if levels above 10^{18} cm^{-3} are considered.

Contrast can also be obtained by changing the surface reflectivity of the sample, i.e., the value of A in Eq. [2]. This occurs, for example, when a portion of the sample is coated with an oxide layer of optical thickness other than $\lambda/2$. Diffraction at the edges of surface discontinuities will also result in enhanced contrast of the displayed image. Such discontinuities can occur in regions where a thermal oxide has been selectively grown on the surface removing some silicon. Small differences in contrast can also be enhanced electronically in the video display circuit.

Experimental Results

To perform transmission microscopy requires that both surfaces of the wafer be highly polished to prevent scattering of the light. Chemical polishes are suitable only if they do not result in an "orange peel" surface. We have had satisfactory results using both purely mechanical polishes and chemomechanical polishes. The use of a fine lapped surface is not acceptable. Because silicon has a high index of refraction, small bumps or depressions can act as highly effective positive or negative lenses. These are observed in transmission as bright or dark spots. This sensitivity to surface finish is not objectionable and, in fact, can be put to good use in studying various polishing techniques. We have also found the method useful for examining wafers that have been etched to reveal crystallographic faults. Small defects that are not easily observed using conventional episcopic illumination stand out in high contrast when observed in transmission.

Figs. 2 and 3 are photographs of a typical integrated circuit taken at two different magnifications to show the ability of the system to display differences in doping density as varying shades of grey. These photographs were taken with the various oxides left in place. No significant change was noted when the same circuit was examined after removing the oxides. We are also able to locate diffusions from a doped oxide, a technique that leaves the silicon surface unmarked.

Fig. 4 is an example of the ability of the transmission microscope to locate defects. The snowflake pattern is a precipitate resulting from a boron diffusion. These particular precipitates were found by J. M. Assour[5] using x-ray topography, a technique that provides essentially unmagnified images only after many hours of exposure. In addition, he located the defects using Sirtl etching, which is a destructive method. The precipitates shown here were located nondestructively with no more effort than would be required using a conventional microscope.

A similar case is shown in Fig. 5 for a heavily tellurium doped sample of GaAs. In this case the sample was etched so as to reveal dislocations prior to examination. The dislocation pits shown clearly at each end of the dislocation. By moving the focus through the sample it is easy to follow the dislocation line from the pit on top of the wafer through to the pit on the opposite side of the wafer. These dislocations are visible only because they have been decorated by the precipitation of excess tellurium (probably in the form of Ga_2Te_3) during growth.[6] Undecorated dislocations are not observed. Dislocations in silicon can be deliberately decorated by the introduction of copper.[7]

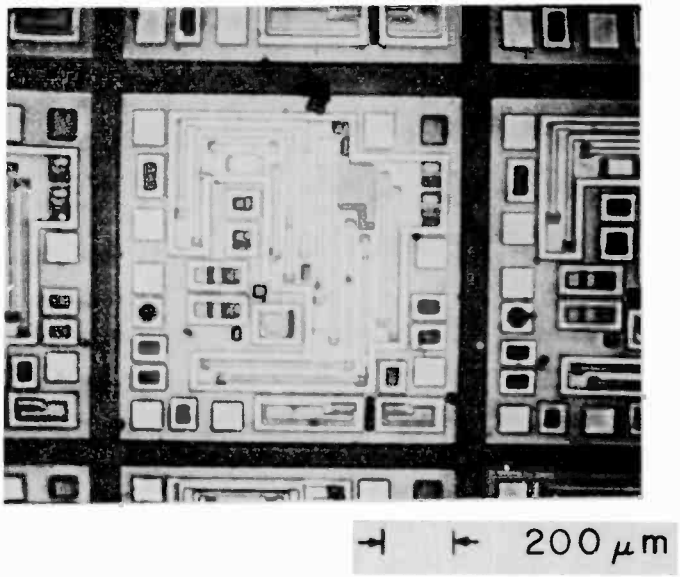

Fig. 2—Infrared transmission photomicrograph of an integrated circuit.

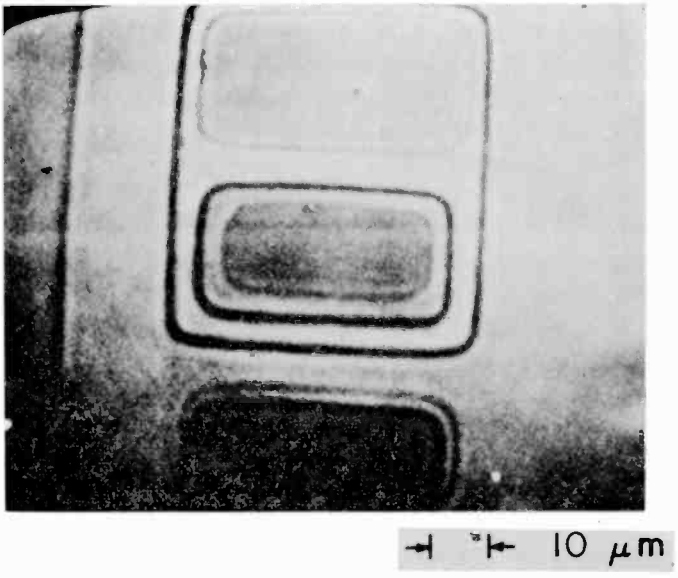

Fig. 3—Detail of circuit element from Fig. 2.

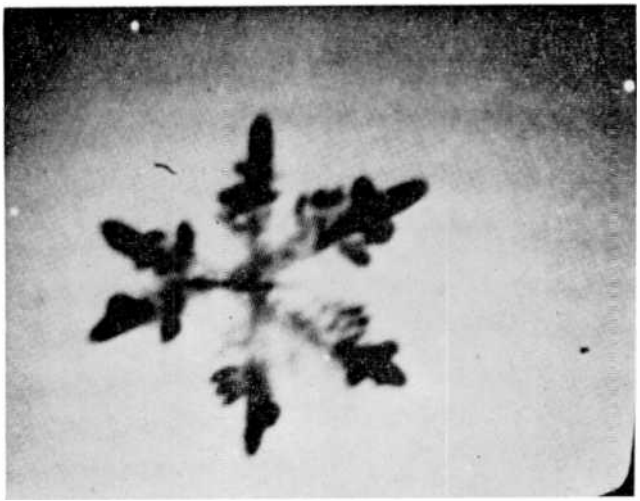

Fig. 4—Precipitate in silicon wafer due to boron diffusion.

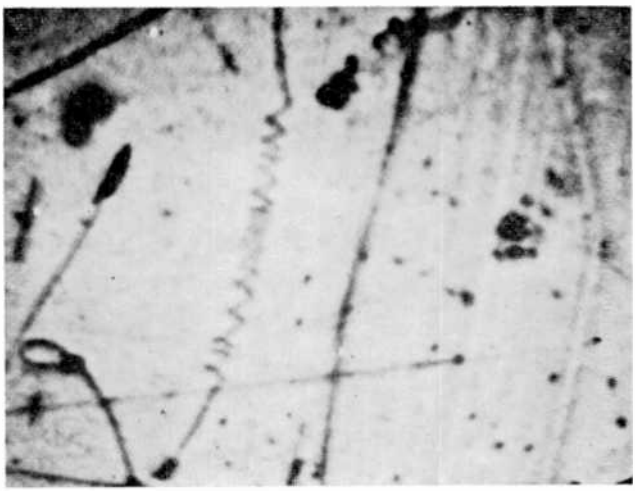

Fig. 5—Precipitates and decorated dislocations in tellerium doped GaAs.

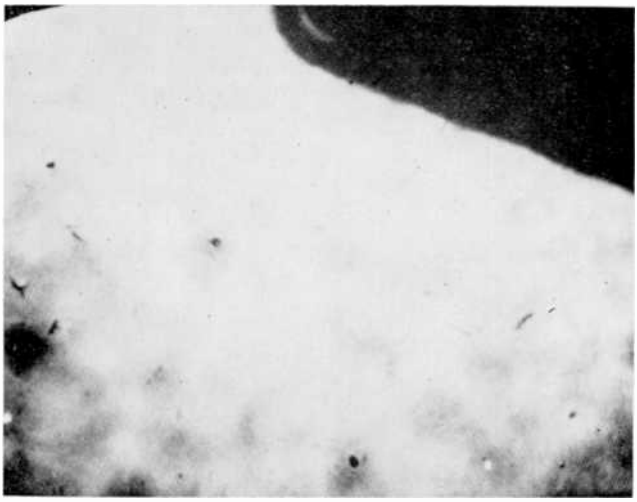

Fig. 6—Base region of epitaxial power transistor.

The wide dynamic range of the system can be illustrated using Figs. 6 and 7. Fig. 6 shows the base region of an epitaxial power transistor with the emitter visible in the upper corner as a region of solid black. Fig. 7 is a view through that same emitter region. A number of defects in both areas are visible as well as a general non-uniformity.

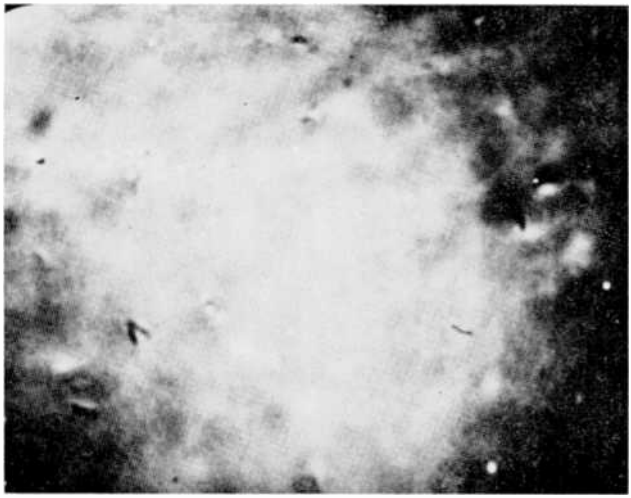

Fig. 7—Emitter region of epitaxial power transistor.

There are other defects that can be found in silicon crystals that are only apparent at much lower magnification than the previous examples. Fig. 8 is a photograph of a 25-mm-diameter, [111]-oriented slice, 0.25 mm thick, that is doped with antimony to near the solid solubility limit. The decided swirl pattern is either preferential impurity segregation about the thermal center of the growing ingot or possibly vacancy clusters as described by de Koch.[8] To obtain this

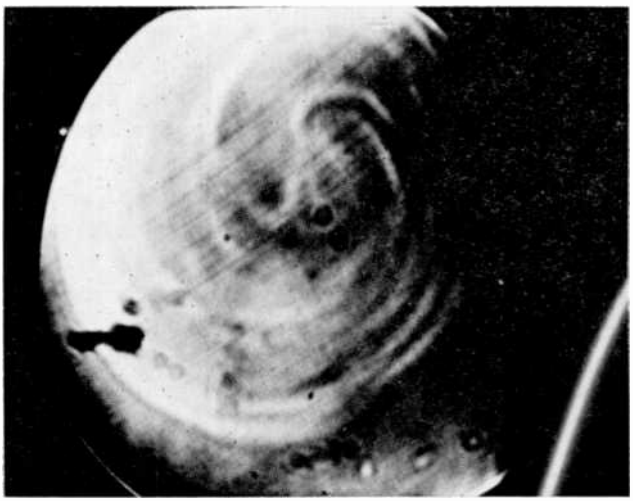

Fig. 8—Microscopic inhomogeneity in 1 inch diameter silicon crystal.

picture we substituted a low-quality plane–convex lens for the microscope objective and placed it such that it projected a reduced image of the wafer that just filled the sensitive area of the vidicon. The light source was also vignetted with a pair of diaphragms so as to obtain a more nearly collimated beam of light. Sirtl etching the wafer did not reveal a high defect density within the swirl pattern.

Discussion and Summary

We have demonstrated that an infrared microscope having particularly good sensitivity for defects in silicon is obtained by combining a silicon vidicon television camera with a standard microscope objective, low-intensity light source, and a video monitor. The rapid fall in response of the silicon vidicon at wavelengths approaching the bandgap of silicon results in an enhanced contrast when using white light illumination sources. Resolution of the system is excellent because it is

limited only by the microscope objective. The usefulness of this simple apparatus is illustrated by photographs taken quickly and nondestructively showing doping variations, precipitates, and decorated dislocations in semiconductor materials and devices.

Gupta et al[9] have compared the response of transmission systems for studying silicon samples. They concluded that a system operating at 3.39 μm was more sensitive to changes in impurity density than one operating at the band edge of silicon. Although this is true, we have demonstrated that, with our very simple system, resistivity swirls are readily detected in substrate material doped in the mid-10^{18} range, and that base, emitter, and collector diffusions in an integrated circuit are easily distinguished. In addition, shallow diffusions can be distinguished from deeper diffusions with the same surface concentration, as can two equal-depth diffusions with different surface concentrations. Furthermore, the contrast of the system described here can be improved at the expense of the sensitivity by using a monochromatic source of light, which is highly attenuated by the sample. The 1.015-μm Hg line with the 1.1287-μm line filtered out is suitable for silicon samples in the usual thickness range. With a narrow spectral source, one can also study heating effects in operating devices because of the shift of bandedge with temperature.[10]

References:

[1] O. Deutschbein and M. Bernard, **Solid-State Physics in Electronics and Telecommunications,** Vol. 1, Part 1, p. 177, Academic Press (1960).
[2] B. Sherman and J. F. Black, "Scanned Laser Infrared Microscope," **Appl. Optics,** Vol. 9, p. 802 (1970).
[3] J. Pankove, **Optical Processes in Semiconductors,** p. 92, Prentice-Hall, Inc., (1971).
[4] V. I. Fistul, **Heavily Doped Semiconductors,** p. 228, Plenum Press (1969).
[5] J. Assour and S.H. McFarlane, private communication.
[6] H. Kressel, H. Nelson, S. H. McFarlane, M. S. Abrahams, P. LeFur and C. J. Buiocchi, "Effect of Substrate Imperfections On GaAs Injection Lasers Prepared by Liquid Phase Epitaxy," **J. Appl. Phys.,** Vol. 40, p. 3587, Aug. 1969.
[7] W. C. Dash, "Copper Precipitate on Dislocations in Silicon," **J. Appl. Phys.,** Vol. 27, p. 1193, Oct. 1956.
[8] A. J. R. de Koch, "Vacancy Clusters in Dislocation-Free Silicon," **Appl. Phys. Lett.,** Vol. 16, p. 100, 1 Feb. 1970.
[9] D. C. Gupta, B. Sherman, E. D. Jungbluth, and J. F. Black, **Solid State Tech.,** Vol. 14, No. 3, p. 44 (1970).
[10] R. A. Sunshine and M. A. Lampert, "Stroboscopic Investigation of Thermal Switching in an Avalanching Diode," **Appl. Phys. Lett.,** Vol. 18, p. 468, 15 May 1971.

Modulation Transfer Function Calculation of Electrostatic Electron Lenses

Illes P. Csorba
RCA Electronic Components, Lancaster, Pa.

Abstract—The modulation transfer function of electrostatic electron lenses is calculated by deriving the point and line image current density functions from the computer calculated electron paths. The method presented is applicable to an optical system with geometrical aberrations.

Introduction

The Modulation Transfer Function (MTF) of ideal image tube lenses free of geometrical aberrations has been derived and computed in a previous paper.[1] In the present paper, the general case that includes geometrical aberrations is discussed. For a system with geometrical aberrations, the transverse focusing error as a function of emission angle may be obtained from the computer plot of the electron paths. Having the transverse focusing error, the point and line image current density functions may be given by simple equations. These functions, in turn, may be converted into the MTF.

Derivation of Point and Line Image Current Density Functions

The MTF of an electron lens may be obtained by calculating the image current density distribution for a sinusoidal pattern. For this purpose assume that ΔA is an elemental area on the surface of the photocathode and from ΔA a polyenergetic emission occurs with an emission energy distribution $dN(V_i)$ and with an angular distribution obeying Lambert's law. The incremental current di_θ emitted

between angles θ and $\theta+d\theta$ from ΔA is

$$di_\theta = 2dN(V_i)\Delta A \sin\theta\cos\theta d\theta. \qquad [1]$$

Here $dN(V_i)$ is the fraction of electrons emitted at an emission energy eV_i in an emission energy interval $d(eV_i)$, and θ is the angle between the emission direction and the direction of the electric field.

The incremental current di_θ strikes the phosphor screen over an annular element having a radius Δr, where Δr is the transverse focusing error. The current density in the annular element may be obtained by dividing di_θ by the area of the annular element,

$$j(\Delta r) = \frac{2dN(V_i)\Delta A \sin\theta\cos\theta d\theta}{2\pi\Delta r d(\Delta r)}. \qquad [2]$$

Here $d(\Delta r)$ is the width of the annular element. The value of Δr as a function of emission angle θ may be obtained by electron trajectory calculations. (Because of the aberrations of the electron lens, the electrons emitted at different emission angles θ strike the phosphor screen at a different radial distance Δr measured from the center of the point image.)

For a monoenergetic line source, the image current density at a distance x from the line is

$$j_l(x) = \frac{1}{\pi}\int_{-\Delta r_m}^{+\Delta r_m} \frac{dN(V_i)\sin\theta\cos\theta d\theta}{\Delta r d(\Delta r)} dy = \frac{dN(V_i)}{2\pi}\int_{-\Delta r_m}^{+\Delta r_m} \frac{\sin 2\theta d\theta}{\Delta r d(\Delta r)} dy, \qquad [3]$$

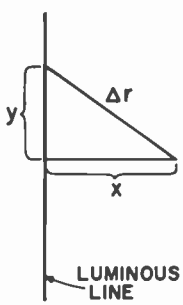

Fig. 1—Diagram for derivation of the image current density of a luminous line.

where Δr_m is the maximum value of transverse focusing error. Changing to a new variable Δr, Eq. [3] becomes

$$j_i(x) = \frac{dN(V_i)}{\pi} \int_{\theta(x)}^{\theta(\Delta r_m)} \frac{\sin 2\theta d\theta}{\sqrt{\Delta r^2 - x^2}}. \qquad [4]$$

For a polyenergetic line source, Eq. [4] must be integrated over the emission energy distribution curve to obtain the image current density at a distance x from the line:

$$J(x) = \int_0^{V_{im}} j_i(x), \qquad [5]$$

where V_{im} is the maximum emission energy.

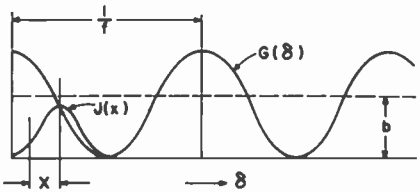

Fig. 2—Diagram for the derivations of image current density distribution of a cosine wave pattern at the photocathode.

For a consine wave pattern at the photocathode, $G(\delta)$, the image current density distribution may be obtained by integrating $J(x)$ over the pattern[2]:

$$F(\delta) = \int_{-\Delta r'_m}^{+\Delta r'_m} J(x)\, G\,(\delta - x)dx = \int_{-\Delta r'_m}^{+\Delta r'_m} J(x)\, [b + b\cos 2\pi f(\delta - x)]dx, \qquad [6]$$

where $\Delta r'_m$ is the maximum value of transverse focusing error of a polyenergetic source, and f is the line frequency of the resolution pattern. According to Eq. [4], $J(x)$ is an even function of x. Hence,

after normalizing by dividing $F(\delta)$ by $\int J(x)dx$, the following equation is obtained:

$$F_n(\delta) = b + b\,A(f)\cos(2\pi f\delta), \qquad [7]$$

where

$$A(f) = \frac{\int_0^{\Delta r'_m} J(x)\cos(2\pi fx)\,dx}{\int_0^{\Delta r'_m} J(x)\,dx}. \qquad [8]$$

The MTF is

$$\text{MTF}\,(f) = |A(f)| \qquad [9]$$

It is possible to generalize the derivation for an asymmetric point image. In this case, it is necessary to write in place of Eq. [2]

$$j(x,y) = \frac{dN(V_i)\Delta A\sin(2\theta)\,d\theta\,d\phi}{2\pi dx\,dy}, \qquad [10]$$

where ϕ is the polar coordinate angle; and for Eq. [4],

$$j_i(x) = \frac{1}{2\pi}\int_{v_{min}}^{v_{max}} dN(V_i)\sin(2\theta)\,\frac{\delta(\theta,\phi)}{\delta(x,y)}dy. \qquad [11]$$

Here, the functional relationship expressed by the Jacobian is obtained from ray tracing data.

After normalizing by dividing $F(\delta)$ by $\int J(x)dx$, the following equations are obtained:

$$\begin{aligned} F_n(\delta) &= b + bA_1(f)\cos 2\pi f\delta + bA_2(f)\sin 2\pi f\delta \\ &= b + b|A(f)|\cos 2\pi f(\delta-\alpha), \end{aligned} \qquad [12]$$

where α is the spatial phase shift and

$$A_1(f) = \frac{\int_{-\Delta r'_m}^{+\Delta r'_m} J(x)\cos 2\pi f x\,dx}{\int_{-\Delta r'_m}^{+\Delta r'_m} J(x)\,dx}\;;\quad A_2(f) = \frac{\int_{-\Delta r'_m}^{+\Delta r'_m} J(x)\sin 2\pi f x\,dx}{\int_{-\Delta r'_m}^{+\Delta r'_m} J(x)\,dx}. \qquad [13]$$

The modulation transfer function is

$$\mathrm{MTF}(f) = |A(f)| = \sqrt{A_1^2(f) + A_2^2(f)}. \qquad [14]$$

Steps in the Calculation of MTF

1. Use an emission energy distribution given by the following equation:

$$dN(V_t) = \frac{\pi^2}{(\pi-2)2}\,\frac{V_t}{V_m}\cos\left(\frac{\pi}{2}\,\frac{Vi}{V_m}\right) d\left(\frac{V_t}{V_{im}}\right)$$

2. Divide the emission energy distribution into 20 monoenergetic groups,

$$d\left(\frac{V_t}{V_{im}}\right) = 0.05.$$

3. Calculate the fraction of electrons emitted in the interval $d(V_t/V_{im})$ for each monoenergetic group.

4. Calculate Δr as a function of θ for each monoenergetic group by running electron trajectories at an increment of $d\theta=2°$ (total of 45 trajectories). Place the phosphor screen in the image plane of electrons having $V_{af}/V_{im} = 0.25$ axial emission energy; where V_{af} represents the axial emission energy for which sharp focus is obtained.[1]

5. Calculate $j(x)$ by using Eq. [4] or [10].

6. Calculate $J(x)$.

7. Calculate $A_1(f)$ and $A_2(f)$.

8. Calculate MTF.

Conclusion

In the past decade, computers have become an important tool in the hands of electron opticians. Initial designs are often checked out on a computer by calculation of the electric potential field and of the electron paths. After the initial computer tests and adjustments of the electron optics, the final test is to build a sample tube and measure the imaging quality. This paper gives a method for computing the imaging quality without building a sample tube.

Acknowledgment

The author thanks E. G. Romberg for his critical reading of this paper and for his valuable suggestions.

References:

[1] I. P. Csorba, "Chromatic-Aberration-Limited Image-Transfer Characteristics of Image-Tube Lenses of Simple Geometry," **RCA Review**, Vol. 31, p. 534, Sept. 1970.
[2] W. J. Smith, **Modern Optical Engineering**, McGraw Hill, Inc., N. Y., N. Y.

A Simplified Method for the Determination of Particle Size Distributions of Fine Magnetic Powders

J. W. Robinson and E. F. Hockings

RCA Laboratories, Princeton, N. J.

Abstract—Small-particle magnetic oxides in the sub-micron range have been quantitatively characterized by size measurements. For each material, the method requires about 100 observations from electron micrographs. The small number of observations gives particle-size distributions with relatively little effort compared with standard methods requiring about 500 observations. The dimensions of several samples of needle-shaped gamma ferric oxides used in magnetic recording materials are tabulated.

Introduction

Particle size distributions of magnetic powders have been shown, by Dismukes et al.,[1] to influence directly the recording characteristics of tapes made from them. We desired to extend their work, but the considerable effort needed to obtain particle size distributions by conventional approaches greatly hindered our progress. This barrier was reduced when a simplified procedure was utilized. The purpose of this paper is to demonstrate that useful data can be obtained from small, readily measured samples.

A sample of about 100 particles can be used to represent the distribution of the bulk population from which it is drawn, provided the data are expressed in the form of a cumulative percent frequency distribution and the sample is from a population that follows one of the standard forms, such as normal or log normal.[2] The magnetic powders discussed here are gamma ferric oxide, and their size distributions follow either the normal or the log normal law. Particles that derive from a chemical precipitation have a size distribution that follows the normal law.[2] If the precipitated particles are then milled, their size distribution is better represented by the log normal law. Another requirement is that the curve used to describe the distribution be smooth. This smoothness will be realized when a cumulative percent frequency curve is obtained from approximately 100 observations. The use of this number of observations represents a considerable reduction in the effort needed to determine particle size distributions. The reproducibility of the method was examined by repeated measurements on a commercial gamma ferric oxide, and then a series of oxides were characterized using this modified procedure.

Experimental

The gamma ferric oxide particles used in magnetic recording are acicular (needle shaped) and less than 1 μm in length. Their dimensions were obtained by direct measurement on transmission electron micrographs. The samples were prepared for examination by dispersing the powders in collodion, forming into thin films, and then observing at about ×30,000 magnification. Sufficient micrographs were taken to include about 100 distinguishable particles. For ease of measurement, photographic prints were made that increased the magnification to about ×90,000. Reduced examples are shown in Figs. 1 and 2. The measurements made on the prints were of particle length and width. Care had to be exercised to ensure that only single particles were measured. Fig. 1 shows overlapping particles. When these are oriented in the same direction they appear as a single particle, but on the original prints the outlines of the individual particles can be distinguished. The length and width of each particle was measured and then the particle was marked to ensure that it was not measured again. The data were arrayed and the cumulative frequency percentages were calculated. In Table 1, values are listed for the particle lengths l, in micrometers, of several commercial oxides.

The reproducibility of the method has been demonstrated by many replicate determinations. For example, data from two measurements on the same batch of oxide are shown in the first two rows of Table 2.

Fig. 1—Electron micrograph of oxide A.

Fig. 2—Electron micrograph of oxide C.

Table 1—Cumulative Frequency Distributions of Particle Lengths of Gamma Ferric Oxides

Oxide A Batch 1 Sample 1				Oxide A Batch 1 Sample 2				Oxide A Batch 2				Oxide C Batch 4			
ℓx10	%	ℓx10	%	ℓx10	%	ℓx10	%	ℓx10	%	ℓx10	%	ℓx10	%	ℓx10	%
0.46	0.6	2.78	70.0	0.57	2.3	2.90	77.0	0.81	2.0	3.12	70.0	0.80	0.7	3.20	66.0
0.57	2.3	2.90	74.0	0.69	3.9	3.00	81.0	0.93	5.0	3.24	71.0	0.91	2.1	3.31	71.0
0.69	3.5	3.00	77.0	0.81	6.2	3.12	85.0	1.04	8.0	3.35	76.0	1.03	3.4	3.54	75.0
0.81	6.5	3.12	79.0	0.93	10.0	3.24	86.7	1.16	14.0	3.48	81.0	1.14	5.5	3.66	76.0
0.93	7.0	3.24	82.0	1.04	16.0	3.35	89.0	1.29	16.0	3.59	83.0	1.26	8.2	3.77	78.0
1.04	12.4	3.35	83.0	1.16	20.0	3.48	90.5	1.39	21.0	3.71	84.0	1.37	13.0	3.88	81.0
1.16	18.0	3.48	86.0	1.29	26.0	3.59	91.2	1.50	23.0	3.82	86.0	1.49	16.0	4.00	82.0
1.29	23.0	3.59	88.0	1.39	30.0	3.82	93.0	1.62	27.0	3.93	89.0	1.60	20.0	4.11	83.0
1.39	29.0	3.71	89.0	1.50	34.0	3.93	94.3	1.74	30.0	4.05	91.0	1.71	23.0	4.23	84.0
1.50	31.0	3.82	92.0	1.62	37.0	4.17	96.0	1.85	37.0	4.17	93.0	1.83	27.0	4.33	85.0
1.62	34.0	3.93	93.0	1.74	42.0	4.28	96.8	1.97	38.0	4.28	96.0	1.94	31.0	4.46	86.0
1.74	39.0	4.05	96.0	1.85	48.0	4.37	98.3	2.08	39.0	4.51	97.0	2.06	38.0	4.57	87.0
1.85	41.0	4.17	96.5	1.97	51.0	5.28	99.0	2.20	42.0	5.78	98.0	2.17	41.0	4.69	88.0
1.97	47.0	4.28	97.0	2.08	55.0			2.32	46.0	6.25	99.0	2.28	48.0	4.80	90.0
2.08	54.0	4.70	98.0	2.20	60.0			2.43	49.0			2.40	50.0	4.91	92.0
2.20	57.0	4.90	98.7	2.32	64.0			2.54	51.0			2.51	55.0	5.14	93.0
2.32	59.0	5.00	99.0	2.43	67.0			2.66	54.0			2.63	59.0	5.26	94.0
2.43	63.0			2.54	73.0			2.78	58.0			2.86	62.0	5.38	95.0
2.54	65.0			2.66	75.0			2.90	64.0			2.97	64.0	5.48	98.0
2.66	69.0			2.78	76.0			3.00	69.0			3.09	65.0	6.06	99.0

The arithmetic means of the length and width of the two samples are seen to be very similar. The distributions of the particle lengths were compared in the form of cumulative percent frequency curves, and these were plotted on arithmetic probability graphs, because normal distributions are then represented by straight lines. The replicate data from Table 1 are shown in Fig. 3 as probability graphs, and they indicate the degree of reproducibility of this simplified method that uses small samples.

Discussion

An outstanding feature of these oxides is the acicular shape of the particles. In Table 2 the mean lengths, mean widths, and their ratio are listed. The length-to-width ratio quantitatively describes the

Table 2—Dimensions of Some Gamma Ferric Oxides

Oxide	Batch	Sample Size	Mean Length $\ell(\mu)$	Median Length $\ell(\mu)$	Mean Width $w(\mu)$	Median Width $w(\mu)$	Mean ℓ./ Mean w.	σ of Length $\ell(\mu)$	σ_V of Length (%)
A	1	170	0.22	0.20	0.045	0.040	4.9	0.10	46
A	1	128	0.21	0.19	0.044	0.040	4.9	0.11	49
A	2	100	0.26	0.24	0.050	0.048	5.2	0.12	46
B	3	89	0.44	0.41	0.096	0.089	4.6	0.21	47
C	4	146	0.28	0.25	0.070	0.067	4.0	0.13	48
D	5	141	0.27	0.25	0.057	0.055	4.7	0.12	46

acicular shape of the particles. The median lengths and widths are also listed, and comparison to the mean values shows that the latter have not been influenced by a few extremes. The ways in which the particles vary in their dimensions provide further means of characterization.

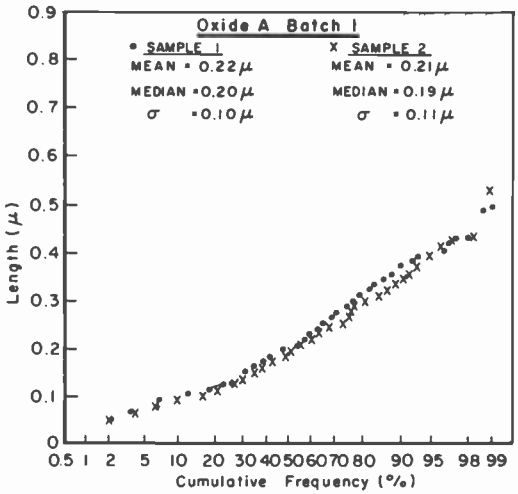

Fig. 3—Arithmetic probability graphs of two samples of oxide A.

A measure of this variation is the standard deviation σ defined as

$$\sigma^2 = \sum \frac{(x - \bar{x})^2}{n - 1},$$

where x is the particle size, $\bar{x}$ is the arithmetic average of the particle sizes, and n is the number of particles measured. The standard deviation is influenced by the mean particle size; therefore, the coefficient of variation C_v, which is defined as $C_v = 100\ \sigma/\bar{x}$, is a more useful measure for comparison when mean values differ widely. This is shown by the constancy of the values in the last column of Table 2.

The distribution of particle lengths for several oxides are shown as probability graphs in Figs. 3, 4, and 5; they are somewhat curved because of deviations from the normal distribution, and these deviations are characteristic of each oxide. For example, the graph for oxide C (Fig. 4) shows a larger deviation from a normal distribution than do the graphs of the other oxides. The curvature suggests that the distribution would be better represented as a logarithmic probability graph; this is shown in Fig. 6. The data fall on a straight line,

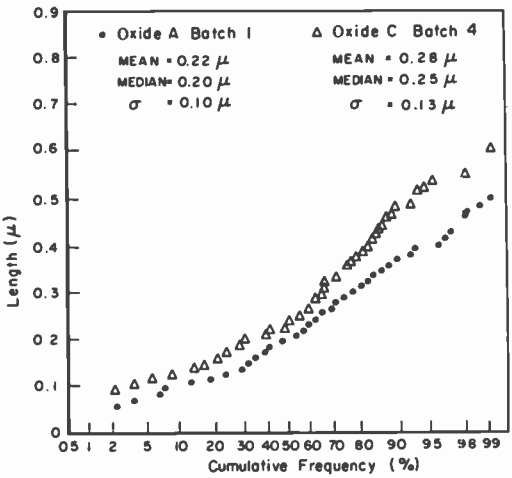

Fig. 4—Arithmetic probability graphs of oxides A and C.

which suggests that the distribution is the result of a milling procedure. In Fig. 2, it can be seen that some of the particles have straight square ends, as if they had been broken as a result of comminution.

The dimensions of several gamma iron oxides used in magnetic tapes and disks have been measured and quantitative comparisons have been made. An example of the use of this type of quantitative char-

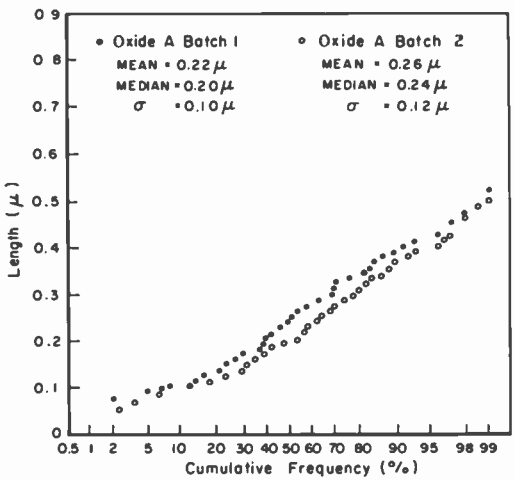

Fig. 5—Arithmetic probability graphs of two batches of oxide A.

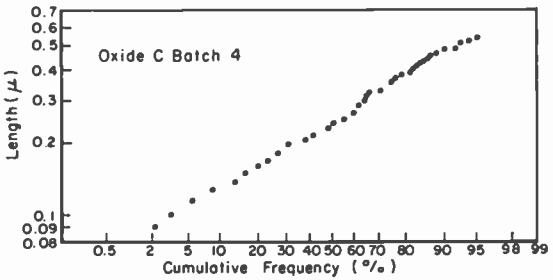

Fig. 6—Logarithmic probability graph of oxide C.

acterization is given by the observation of differences between two batches of the same oxide. The probability graphs of the two batches, received at different times, show these differences (Fig. 5). Table 2 shows that batch 2 has a larger mean particle size than batch 1. The mean particle length is 0.26 μm compared with 0.22 μm, and the mean particle width is 0.050 μm compared with 0.045 μm. A comparison of the graphs shows that the shapes of the curves are similar but that they are displaced.

This abbreviated statistical method will make the correlation of magnetic recording properties with particle size distributions a more reasonable task with regard to time and effort. The method has already been valuable for the characterization of new iron oxides and for their quantitative comparison to presently used oxides.

References:

[1] J. P. Dismukes, D. F. Martin, L. Ekstrom, C. C. Wang, and M. D. Coutts, "Ferromagnetic Chromium Dioxide for Magnetic Tape," **Ind. Eng. Chem. Prod. Res. Develop.**, Vol. 10, No. 3, p. 319, Sept. 1971.
[2] G. Herdan, **Small Particle Statistics**, Elsevier, Amsterdam, 1953, p. 127.

Electrophotography—A Review*

Robert B. Comizzoli, G. S. Lozier, and D. A. Ross
RCA Laboratories, Princeton, N. J.

Abstract—This review is concerned primarily with the electrophotographic systems currently in use, i.e., the electrodeless, stored energy systems. First, the history of reproduction is traced from printing, through wet- and dry-chemical photography, to electrophotographic systems. The electrodeless system is defined and described in terms of the processing. Then, the light sensitive materials and processing are examined, and the characteristics of the material comprising the electrophotographic layer are related to the operational steps of charging and exposure. The principal development materials, dry powder and liquid toners, are described on an electrochemical basis, and the toning mechanisms are reviewed. Finally, the principal applications and future trends of electrophotographic systems are outlined.

1. Introduction

Electrophotography, as its name implies, is a technique for imaging, copying or printing by electro-optical methods in contrast to mechanical-impact or contact printing or to the photochemical processes used in conventional chemical photography. The technology is based on electrostatic forces and photoconductivity and requires no chemical processing.

The practical application of insulating photoconducting materials for reproduction came initially through invention rather than the systematic development of materials suitable for electrophotography. It was only after discovery and reduction to practice that large scale research began to be directed to the improvement and development of new and better materials and processes. Research has increased with the commercial success of electrophotography in the office copying field.

* This paper has also appeared in the April 1972, Vol. 60, No. 4, issue of the *Proc. IEEE*.

This review describes the basic processes and technologies used for electrophotographic reproduction and points out some of the still unsolved technical problems. Rather than attempt to cover the complete field of electrophotography, we refer the reader to several excellent general reviews for details.[16, 27, 139] We concentrate on the more common systems, their present and future status, and possible systems yet to be developed. We have also attempted to place electrophotography in its proper place as an active, growing branch of the graphic arts industry.

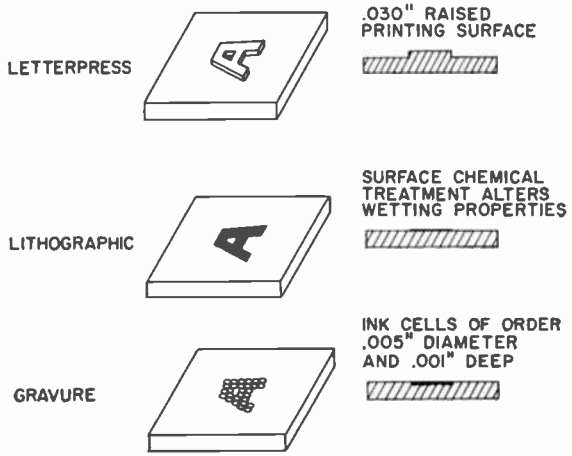

Fig. 1—Schematic representation of three principal kinds of printing plates used in mechanical printing.

1.1 Mechanical Reproduction

By reproduction we mean any method of creating a copy of an original image. The oldest and most widely used method of reproduction is mechanical or contact printing and the earliest examples were made from wood cuts. The wood-cut was hand-carved by the artist, inked, and the image reproduced on a suitable surface by contact. While useful for graphics or single documents, each new page had to have its own hand-carved master.

Around 1440, Gutenberg produced the first successful, movable-type from which he could make a printing master. He could compose the master by arranging the movable characters in page form and then print the desired number of copies. When complete, the letters were rearranged and reused for the next page.

Mechanical impact printing has grown from these humble begin-

nings to a $20 billion industry today with mammoth presses printing at web speeds of up to 25 miles per hour. The masters are no longer hand-carved but are formed by sophisticated chemical, electro-mechanical, and electro-optical techniques, and the inked surfaces include metals and plastics. The three main mechanical configurations for the printing masters are illustrated in Fig. 1.

1.2 Photographic Reproduction

Paralleling the development of better contact-printing processes was the search for a method of capturing an optical image on paper. Although aids to improve reproduction fidelity were available, such as pinhole and lens cameras with mirrors for directing the image onto the copy paper, a skilled artist was needed to draw the image by hand.

Wet Chemical Photography

Photochemical reactions by which light causes a blackening of certain chemicals were known in the early 1800's. The technique of making these changes permanent and making the non-light-struck areas of the image immune from further light darkening was discovered in 1839 by Daguerre who succeeded in producing permanent photographic images on a metal plate.[22] Almost simultaneously, Talbot in England announced his version of a photographic process, using AgCl salts on paper, that could be made permanent by a chemical treatment following exposure and development.[158] Talbot's fixing step made photography a practical process and the ensuing 130 years have seen the development of cameras and films for almost every conceivable use.

Wet photochemical systems that do not use silver halides, although lacking the speed of the silver systems, found other important uses. One of the most important was the "blueprint" which resulted from the reduction of ferric to ferrous salts and which was developed by Sir John Herschel in 1842. This remained the standard method of reproducing engineering drawings until the development of the diazo process in the 1920's.

Dry Chemical Photography

Aggressive development of wet photochemical camera imaging systems continued through the 1930's. In the early 1940's, Agfa[137] in Europe and Land[96] in the United States developed a silver halide diffusion transfer process that could produce partially dry copies of documents. Also, in the late 1930's, Miller at the University of Minnesota demon-

strated thermography,[116] a system using heat sensitive dyes. Another thermal imaging system described by Robillard makes use of the change in the dielectric constant of certain materials when they absorb light.[135] If the sheet is heated with rf energy, there will be a selective absorption of the rf energy in the light-struck areas of the sheet. Heat sensitive dyes incorporated into the sheet will develop a visible image where the rf energy has been absorbed.

One of the more recent dry photochemical systems used commercially is "Dry Silver."[150] Both opaque and transparent films are available commercially, and the optical speed is close to that of the conventional electrophotographic systems.

LIGHT SENSITIVE MATERIALS	IMAGE	LATENT IMAGE	MECHANISM	VISIBLE DEVELOPMENT	
Heat Sensitive Dyes	Thermal	None	Thermography	None	(116,135)
Dry Silver	Optical	Silver Nuclei	Silver Photography	Heat	(150)
Free Radical	Optical	Free Radicals	Free Radical Chain Reaction	Heat or Solvent Vapor if Needed	(97)
Photo-Polymerization	Optical	Photo Excited Monomers	Polymerization	Heat or Vapor if Needed	(17)
Photo-Chemical	Optical	Excited Molecules	Diazo	Heat or Vapor	(124)
Vesicular	Optical	Excited Diazonium Compounds	Gas Formation and Expansion	Heat to Form Gas Bubbles	(124)
Thermal Evaporation	Optical	Oil Film	Adherography	Powder or Liquid Toner	

Fig. 2—Characteristics of dry photo-chemical systems.

If light can trigger a photochemical reaction that will propagate, a gain may be realized. Free radical systems have been described in which the absorption of a photon will cause a chain reaction and give a quantum gain.[97]

Photopolymerization can be used to produce an image. With proper control, high gains can be achieved.[17] The most extensive use of this process has been in the formation of resists for etching processes and in developing deep relief printing plates.

The dissociation of diazonium compounds by light can be used to develop a vesicular film image as well as to produce normal diazo images.[124]

Although these dry photochemical systems are not truly electrophotographic in that no macroscopic electrical forces are used, they have been and still are being used extensively for document reproduction. They have been included for completeness and are summarized in Fig. 2.

1.3 Electrophotographic Reproduction

While commercial electrophotography is a relatively new technology, the use of electrical rather than chemical energy to produce images has a long history.

Electrophotographic systems can be broken down into two broad categories: (1) those systems that obtain electrical energy from an external source and (2) those in which the electrical energy is incorporated in the photosensitive surface prior to optical exposure.

LIGHT SENSITIVE MATERIAL	LATENT IMAGE	MECHANISM	DEVELOPMENT	
Reuseable Plate in Contact with Electrosensitive Paper	None – Immediate Development	Electrosensitive Dye	Direct	(167)
Reuseable Plate in Contact with Insulating Paper	Electrostatic	Charge Transfer	Powder or Liquid – Direct	(14,25,26,170,181)
Reuseable Plate	Electrostatic	P.I.P.	Powder – Transfer	(39,80)
Reuseable Plate and Paper	None – Immediate Development	Field Control of Toner Trajectory	Direct – Powder Toner	(69)
Toner Particles	None – Immediate Development	Electrophoretic Deposition of Charged Toner	Direct	(163)
Photo-Emitter	Electrostatic	Emission of Charges onto an Insulator	Powder or Liquid – Direct	(98,147)
Screen Printing	Electrostatic Mask	Toner Attraction	Powder – Direct	(133)

Fig. 3—Electrophotographic systems using external energy source.

External Field Systems

Historically, systems that used external fields were the first to be developed. A number are listed in Figure 3.

In 1922, von Bronk received a patent on a system using a photoconductive plate in contact with electrosensitive paper.[167] A system using a similar principle has recently been reduced to commercial practice. It uses a sandwich of a photoconducting plate in contact with an insulating, coated paper.[14,25,26,170,181] Light striking the photoconductor produces charge carriers which, with the aid of an external field, transfer to the insulating surface of the contacting paper. The image can then be developed in a separate step with powder or liquid electroscopic toners.

Another system that may use an external field during exposure makes use of the polarization properties of certain types of photoconducting materials. If photoconducting pigments or particles are imbedded in an insulating matrix and an external field is applied during

illumination, the charge carriers will move to one or the other end of the particle. If the photoconducting pigments are suitably constructed, the charges will be trapped after illumination has ceased and the field has been removed. The result is a persistent internal polarization.[39,80] The external fields resulting from this internal polarization can attract toner particles to produce an image.

Another variation of the use of external fields during exposure is that in which a powder toner is injected into the field region between an insulating paper and a photoconducting plate. Illumination of the plate causes parts of it to be conductive and will distort the electric field lines in the toner region. If the toner follow the field lines, it will travel to areas that are still insulating rather than to those areas that are conducting, thus forming an image.[69]

A system in which the toner particles themselves are photoconducting has been described.[163] When illuminated in the presence of an electrical field, the particles exchange charge with an electrode. Once charged, they travel under the influence of the electrical field to the opposite electrode. If the toner particles are made of dyes that selectively absorb light in specific regions of the visible spectrum, only those particles with specific spectral absorption regions will be charged and produce a colored image representing the color of the incident light.

Another external field system uses photoemission. Light striking the photoemitting surface causes electrons to be collected on an insulating surface under the influence of an accelerating field. The image is made visible by developing with a powder or liquid toner material.[147] If the photoemitted electrons strike insulating wires in the vacuum system faceplate, the wires may be used to transfer the charge to insulating paper outside the vacuum system.[98]

Electrostatic screen printing uses fixed metal masks to form the image. Powder toner is attracted through holes in the mask by an external field and strikes an imaging surface placed between the mask and a conducting electrode. A more recent innovation is the use of a mask or mesh coated with insulating photoconducting material[133] The mask is corona charged and then exposed. The light locally reduces the charge on the mask and alters the electrical aperture of the mesh. Where the electrical aperture is large, powder toner is accelerated through the mask by an external field and strikes the printing surface placed between accelerating electrodes.

Electrodeless Systems

Fig. 4 lists electrodeless systems where internal electrical fields provide the energy for imaging. The most commonly used form of electro-

photography as we know it today is the development of a latent electrostatic image on a precharged insulating photoconductor as described by Carlson in 1938.[11] When suitable charged toner particles are brought into contact with the latent electrostatic image, those regions not exposed to light, and still charged, attract the toner, while the discharged, exposed regions do not. The first public announcement of Carlson's process was made in 1948.[140]

LIGHT SENSITIVE MATERIAL	PRE-EXPOSURE PREPARATION	EXPOSURE	LATENT IMAGE	MECHANISM	VISIBLE DEVELOPMENT	
Insulating P.C. Reuseable Plate	Corona Charge	Optical	Electrostatic	P.C. Discharge	Powder-Transfer	(140)
Insulating P.C. Coated Paper	Corona Charge	Optical	Electrostatic	P.C. Discharge	Liquid/Powder – Direct	(180)
Reuseable Plate or Coated Paper	Optical Image	Corona	Persistent Conductivity	P.C Discharge		(81)
Coated Paper	None	Optical	Persistent Conductivity	Electro-less Plating	Electro-Plate	(7,78)
Coated Paper	None	Optical	Persistent Conductivity	Electrolytic	Electro-Plate	(78,174)
P.C. Thermo-plastic	Corona Charge	Optical	Electrostatic	Deformation	Heat	(40,44,177)
Laminar Particles in P.C. Binder	Corona Charge	Optical	Electrostatic	Particle Orientation	Heat	(84)

Fig. 4—Electrophotographic systems using stored energy.

To avoid having to transfer the toned image from the insulating photoconductor to paper, the photoconducting layer may be coated directly on the paper. It was found that white, French-process ZnO powder (produced by burning zinc in air) in an insulating resin binder could act as an electrophotographic layer.[50] This direct electrophotographic process was first reported in 1954 by Young and Greig[180] and was called Electrofax.* Greig also reported on the use of dye sensitization to extend spectral response.

While these two systems have been the most successful of the commercial electrophotographic systems using internal fields, there are other useful electrophotographic systems that do not use an external field. One, which makes use of the persistent conductivity following exposure, reverses the charging-exposure cycle.[81] Another variation of persistent conductivity is the reduction of metallic ions in an electroless plating process by the light-excited carriers. The resulting latent image can be enhanced by further electroplating.[7,79]

* Electrofax is a registered trade name of RCA.

Persistent conductivity of the photoconductor can be used with external field developing systems. One such system uses the persistent conductivity of a ZnO-binder layer to electrolytically deposit metal ions from an aqueous solution following exposure.[78,174]

A thermoplastic insulating photoconductor has been used for producing images. It is charged, exposed, and then heated. The electrostatic forces in the charged areas cause the layer to deform producing a ripple or deformation image that can be viewed by Schlieren projection. Further heating will erase the image and the layer can be re-used.[40,44,177] Various forms of surface crazing induced by electrostatic fields in conjunction with heat or a vapor atmosphere have also been used for imaging.[123]

Laminar particle orientation has been used to prepare opaque or transparent images. Colloidal substances such as graphite or aluminum having a plate-like structure are embedded in a thermoplastic, photoconducting, insulating binder with random orientation forming an opaque layer. The plate is charged and imaged to produce a latent electrostatic image. Heating and softening of the layer allows the particles to align themselves with the electrical field in the nonimaged areas which then transmit light. Resolutions of 11 lines per mm have been reported with a contrast ratio of 40:1.[84]

2. The Electrophotographic Process

The most common form of electrophotography today uses an insulating photoconductor which is charged, exposed and toned to produce a visible image. The toner particles may be the same or opposite in charge to that of the latent electrostatic image, giving either a positive (direct) or negative (reversal) image of the original. The operational steps are illustrated in Figure 5.

2.1 Charging

The most common charging method used today is the corona-type charger used by Carlson.[12] It consists of insulated fine wires supported in a conducting shield and positioned close to the electrophotographic surface. The voltage on the wires is several thousand volts. With wires of about 3 mils diameter, this is enough to produce a glow discharge in the high field region around the wires. The dc field between the wires and the photosensitive surface moves the ions to the insulating photoconductor surface where they are trapped in the dark.

The ionic composition of the glow discharge in various ambients has been measured with a mass spectrometer.[146] The major negative

constituent at atmospheric pressure in both nitrogen and oxygen is reported to be CO_3-. Positive corona in air yields primarily $(H_3O)+$. The actual ionic species on the surface of the insulator is still a matter of speculaton.

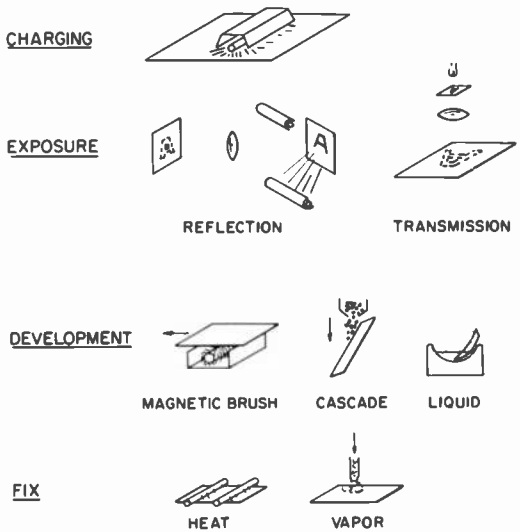

Fig. 5—Operational steps in electrophotography with stored-energy systems.

In some systems, the surface is charged to saturation, i.e., the surface is given as much charge as it will take. If there is danger of causing irreversible breakdown through the insulator, the surface voltage of the photoconductor can be limited by reducing the voltage on the corona wires or by using a grid of fine wires between the insulator surface and the corona wires.[169]

Since the voltage should be across the photoconductor only, the substrate which supports the photoconductor should be more conducting than the layer. In systems where the photoconductor is used as a transfer medium and re-used for each image, it is usually on a metal substrate. In direct imaging systems where the photoconducting layer is coated on paper, it was recognized very early that the paper should be treated to make it conducting enough to allow charge to travel through the substrate to the paper base side of the electrophotographic layer. Since paper conductivity varies widely with humidity, this conductive treatment is particularly important in low relative humidity

conditions.[68] To prevent the paper from sticking to the metal ground plate, a double corona system can be used, which places an equal and opposite charge on the back of the paper base, thus avoiding induced charges in the ground plate.[45]

2.2 Exposing

After the layer is charged in the dark, it is exposed with an optical image of the document to be reproduced. Where light strikes the layer, the charge is dissipated. Where the layer has not been exposed, the electrostatic charge remains forming a latent electrostatic image of the original.

The exposure may be from an illuminated opaque original, the image being focused on the electrophotographic surface with a lens. This is the most common method used in office copiers. The image may also be from transparent full-size film or microfilm, from cathode-ray tubes, or from any type of light-image-forming device. The light source used for illumination should have a spectral distribution that matches the photoconductor. Only the light absorbed by the photoconductor is useful in discharging the layer, and a bad mismatch between the light source and the photoconductor will lower the speed of the system. Fig. 6 illustrates the match between a commercial dye sensitized Electrofax paper and a P-11 phosphor in a cathode-ray tube.

The maximum quantum efficiency of the corona-charged electrophotographic layer is unity. The energy required to discharge the layer at maximum absorption is 5 to 50 ergs per cm^2. Any loss of light by transmission through or reflection from the layer as well, as any loss of charge carriers generated by the light, will increase the energy needed for discharge and reduce the quantum efficiency.

2.3 Toning

Following exposure, a latent electrostatic image is formed. This image can be made visible by bringing charged toner particles close to the surface of the insulating photoconductor.

The toner particles may be dry powder that is transported to the insulator surface by a carrier of some inert material. Two types of carriers are insulating glass beads and fine magnetic particles.[53] The toner particles are pulled away from the carrier and adhere to the charged areas of the image. Toner particles may also be suspended in insulating liquids which act as a carrier.[112,113] When the latent-electro-

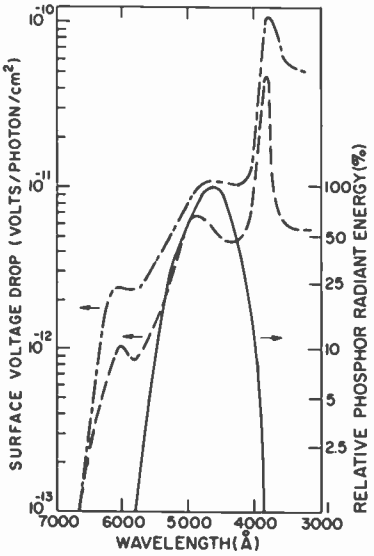

Fig. 6—Light sensitivity of typical ZnO–resin binder layers compared with light output of cathode-ray tube.

static-image surface is immersed in the toner bath, the toner particles adhere to the charged image areas making the latent electrostatic image visible.

The visible image formed by the toners may be transferred to ordinary paper if the photoconductor is to be re-used. In such cases, a piece of ordinary paper is brought into contact with the toner, and the toner is transferred electrically by applying an appropriate electrical field. If the insulating photoconductor has been applied to the surface of the final piece of paper, as in Electrofax, no transfer step is required.

2.4 Fusing

The final image must be fixed to the paper so that the toner cannot escape when handled. In the case of powder toners, this is accomplished by heating the thermoplastic toner particle so that it becomes soft and adheres to the paper. In the case of liquid toning (generally used when the insulating photoconducting surface is on the paper), it is possible to add to the liquid vehicle agents that fix the image when the liquid vehicle has evaporated. Mild heating or hot air blowing over the sheet is sometimes used to enhance the evaporation at normal office-copier

speeds. In very high speed machines, the liquid-suspended toner may be coated with a thermoplastic and heated to fix permanently.

These four or five steps, depending on the system in use, are the most common methods for practicing electrophotography today. It is also possible to transfer the electrostatic charge pattern (formed by charging and exposure) to another sheet which is thereafter toned.[139] This process will not be discussed.

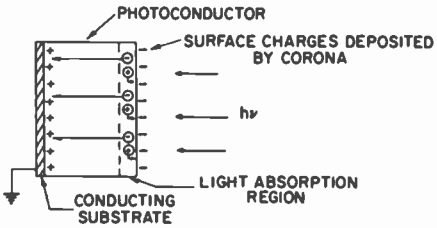

Fig. 7—Optical generation of carriers by strongly absorbed light in an ideal photoconducting layer. In the ideal layer, all carriers are transported to the appropriate surfaces.

3. The Electrophotographic Layer

3.1 The Physical Model

In the *ideal* case, we assume the electrophotographic layer is a homogeneous, perfectly insulating photoconductor.[171] Charge of one sign is uniformly deposited on the free surface. The compensating opposite charge appears at the conducting substrate. The layer charges as a simple capacitor with no space charge in the volume of the layer. The relation between surface charge density and voltage is linear and no current flows in the dark.

Illumination of an ideal layer by strongly absorbed light generates electron–hole pairs as shown in Fig. 7. Every incident photon is absorbed and generates a hole–electron pair in a narrow region close to the charged surface. Recombination takes place only at the surfaces where the optically generated carriers and the surface charges recombine. Every photon neutralizes one charge for a quantum efficiency of one. The decay rate of voltage with time under constant illumination is linear and there are no response time effects due to carrier trapping. If the charged layer is illuminated with a light pulse of short duration compared to the charge-carrier transit time, there will be a linear decay in voltage with time up to the transit time; at that point there will be a sharp kink after which the voltage is constant, if diffusion effects are neglected. We assume, further, that the number

(per cm^2) of optically excited mobile charges drifting in the field is small compared to the number (per cm^2) of charges on the surface.

In real electrophotographic systems, intrinsic and operational effects complicate the ideal picture.

Charging

In charging, practical systems show evidence of volume space charge, injection at contacts, and localized breakdown. These phenomena have varying importance depending on whether the electrophotographic material is a one- or two-carrier system, the relative sign of the deposited surface charge with respect to the volume space charge, and the surface and substrate contact limitations.

In depositing surface charge on a one carrier material when the sign of the corona deposited charge is the same as that of the mobile charge, a space charge of sign opposite to the surface charge will form if mobile carriers are available in the conduction band or in shallow trapping states.[2] For example, if negative corona charge is deposited on the surface of an n-type layer, electrons in the conduction band will be swept out to the substrate. A net volume positive charge will result within the layer which may or may not pentrate to the substrate depending on the magnitude of the deposited surface charge and density of electrons available to be swept out. For a uniform space-charge distribution, the relations among surface charge, surface voltage, and space charge are shown in Figure 8. For a material with one carrier mobile, a blocking contact is only required at the surface since, by assumption, there is no conduction by positive charges and the substrate contact need not be blocking.

For positive charging of the surface of an n-type layer, the substrate contact must block electrons going from the substrate into the layer. In this case, the field of the positive charges on the surface attracts electrons from the volume of the layer. Depending on the magnitude of the positive surface charge, the space-charge region, now of the same sign as the surface charge, may be confined within the layer or may extend to the surface. This situation is shown in Fig. 9 for a uniform-density space charge. Note that for a given surface voltage, the field at the substrate interface is greater for the case in which the space charge is of the same sign as the surface charge than for the case of opposite sign, shown in Fig. 8. Analogous considerations apply for a p-type material.

For two-carrier materials, the substrate and the surface contact must be blocking for the appropriate charge carrier. On charging by

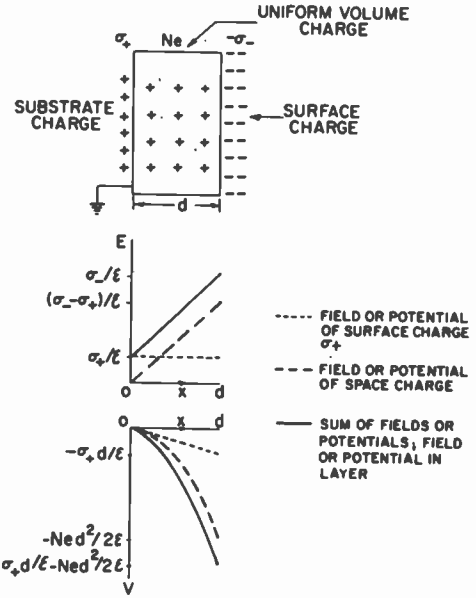

Fig. 8—Electrophotographic layer with negative surface charge, uniform positive volume charge, and positive substrate charge showing field and potential profiles.

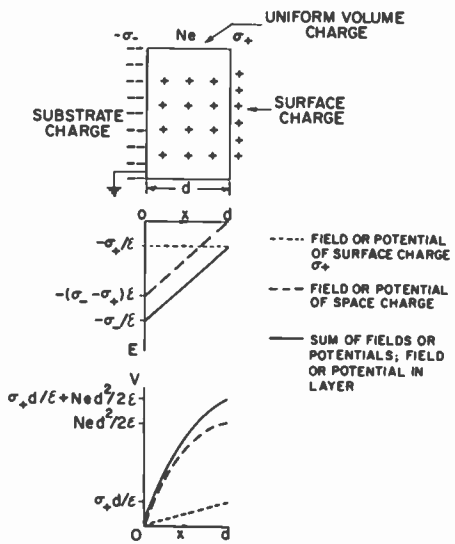

Fig. 9—Electrophotographic layer with positive surface charge, uniform positive volume charge, and negative substrate charge showing field and potential profiles.

either sign of corona, both positive and negative charge carriers will be swept out. A space charge will form if there are more thermally available charge carriers of one sign than the other during charging.

It has been pointed out that the density of the space charge in the volume of the electrophotographic layer depends on the density of charges available to be swept out by the applied field. These charges may be available in dark equilibrium or they may be the result of previous light exposure. The latter case is referred to as the "fatigue effect," and is important in re-usable photoconducting plates.

Thus, the actual charge distributions depend on the sign of the applied charge, the availability of carriers in the material, the properties of the contacts, and the history of the sample. Since the release of carriers from traps may continue for significant times after charging, the charge distribution itself may vary with time.

Dark Decay

After charging, the surface voltage of an electrophotographic layer decreases in the dark. Typical decay rates near the maximum surface voltage are of the order of one volt per second. The dark decay may have several causes. Charge may be injected from the surface or the substrate. The rate of voltage decay from this process depends on the rate of injection or breakdown and the motion of the charges through the layer. Thus, in an n-type material, a leaky substrate contact will result in greater dark-decay rates when the surface charge is positive than when it is negative, since injected electrons from the substrate move toward the surface more readily than injected holes. Also, if a space charge forms in the layer upon charging, the electric field at the substrate is greater when the surface deposited charge is the same sign as the volume space charge (positive for an n-type material). This higher field may lead to higher injection rates and breakdown.

Injection of charge from the surface lowers the surface voltage by decreasng the surface charge. Injection from the substrate reduces the voltage by altering the charge geometry — the capacitance is effectively increased since the charge spacing decreases. The surface charge density need not decrease, although it eventually will when a charge injected from the substrate recombines with a surface charge.

A bulk process that contributes to voltage dark decay and that may not alter the surface-charge density is the release of carriers from traps. Thus, for an n-type layer charged negatively, the surface voltage will decay as the positive volume-space-charge density increases

with time due to the release of electrons from traps. Such a process may be responsible for increased dark decay after light exposure, the fatigue effect. This situation is illustrated in Figure 10 in an energy band diagram.

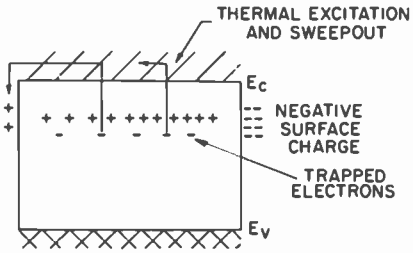

Fig. 10—Band diagram showing a possible dark decay process in which the surface charge does not decay. Slow release of electrons from traps increases the positive charge density in the volume thus decreasing the voltage. (Band bending is not shown for simplicity.)

Light Exposure

In the ideal photoreceptor, light absorbed in a thin region near the surface generates electron–hole pairs that drift toward the appropriate surface charges. For each photon absorbed, one electron–hole pair is formed and one surface charge is dissipated. In practical materials, this simple picture is complicated by charge-carrier generation within the layer by weakly absorbed light, a field-dependent quantum efficiency, carrier recombination and deep trapping, and shallow trapping.

Light penetration into electrophotographic layers varies from strong absorption within less than 1μm of the surface to weak absorption where the light excitation is nearly uniform throughout the layer. This is a function of the material and the wavelength of the illumination. Weakly absorbed light, besides being inefficient in that only part of the incident light is absorbed, can introduce complicating effects in a one-carrier system. If the incident light generates carriers throughout the thickness of the layer and if only one sign of carrier is mobile, then as the mobile carrier is swept out, a space charge whose sign is that of the immobile carrier is formed. This process gives an efficient voltage decay to one-half the initial voltage and a relatively slow decay for the remaining voltage in a simple model assuming no initial space charge, uniform illumination, and long range for the mobile carrier.[18]

There are two effects contributing to the inefficient voltage decay after the voltage midpoint is reached as shown in Figure 11. At the

voltage midpoint, the space-charge region breaks away from the substrate and shrinks toward the surface. Since the effective capacitance of the layer now increases with time, each neutralized charge carrier contributes a decreasing amount of voltage decay. Also, since illumination contributes to the voltage decay only in a field region, a decreasing portion of the light is effective in contributing carriers. If the deposited surface charge sign is that of the immobile carrier, then the space-charge region breaks away from the surface and shrinks toward the substrate. The voltage decay is identical, however.

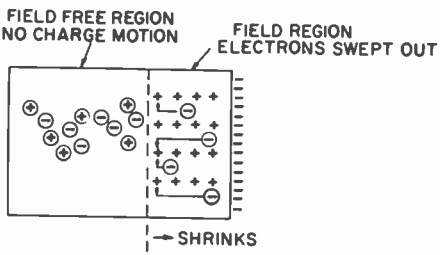

Fig. 11—One carrier, uniformly illuminated electrophotographic layer showing space charge resulting from electron sweep out. Field region shrinks as electrons are captured at edge.

Recombination of carriers may take place through recombination centers generated by the optical excitation in which case the recombination occurs only in the illuminated region. This process should be negligible except at high light levels. Recombination may also occur between photogenerated free carriers of one sign and pre-existing oppositely charged localized states.[2] This latter process may be associated with space-charge regions and is not confined to the illuminated region. Both processes can act to lower the light-induced voltage decay sensitivity. In the former case, carriers recombining in the generation region do not contribute to the decay of surface charges or space charges. In the latter case, charge is neutralized, but the charge carriers move through only a fraction of the sample thickness since they are captured by centers that form a volume space charge. The voltage change contributed by this motion of charge will be smaller than that due to the motion of a carrier from the generation region to the opposite surface. In terms of *charges neutralized,* however, the sensitivity is unchanged. In certain applications, charge neutralization may be a more proper criterion of light sensitivity than voltage decay.

Carrier trapping is similar to recombination in that it limits the

motion of free carriers. It is convenient to distinguish deep trapping and shallow trapping. Deep trapping immobilizes a carrier in a localized energy state for times long compared to times of interest. In addition, the localized level is in a charged state after capturing the carrier. Thus, deep trapping during light discharge results in the formation of a space charge of sign given by the trapped carrier. Such processes will result in a "residual voltage"[100, 144]— a lower voltage limit that is approached by the light-induced decay.

Shallow trapping does not affect the sensitivity of the photoreceptor, but only the time dependent decay of the voltage. For example, a negative carrier optically generated near the negatively charged surface will drift toward the substrate. As it moves through the layer, it is captured and released by shallow traps. "Shallow" means that the localized state is sufficiently close to the conduction band that thermal energy can excite the captured carrier to the conduction band in times of interest. The carrier may be captured and released many times as it drifts toward the substrate and may spend much more time in trapping states than in the conduction band.[41, 42, 136, 138]

The previous effects are concerned generally with the transport of charge carriers and determine the distance traversed by a carrier and the charge geometry. There are also effects involving the generation of charge carriers by light. The absorption of a photon in certain materials produces a bound electron–hole pair that dissociates under the action of an external electric field.[155] Thermal energy and the potential energy of the field contribute to the dissociation. Such a process limits the quantum efficiency in a way that depends only on electric field, and *not* on a combination of electric field and sample thickness, as in recombination or deep-trapping processes.

3.2 Practical Electrophotographic Materials

Selenium

In electrophotography, the amorphous form of selenium is used. It has a random chain structure, and is highly insulating and photoconducting. Electrophotographic plates are obtained by evaporation in vacuum onto conducting substrates. Schaffert[139] discusses the properties of elemental selenium and effects on electrophotographic performance of substrate, preparation procedures, and impurities.

The bulk substrate material is not as important to performance as the character of the substrate surface and its preparation. The substrate surface conditions have a large effect on the voltage dark decay

characteristics for both polarities of surface charge. Chemical cleaning treatment reduces the dark-decay rate.[139] The dark-decay rate on clean aluminum supports, however, may be too high, and it is necessary to form a layer of Al_2O_3 at least 15 Å thick on the aluminum surface before Se deposition.[145] This oxide layer acts as a barrier for carrier injection from the substrate. It is thin enough so that the voltage drop across it, which is limited by the breakdown field, is negligible when compared to the voltage across the photoconductor.

The deposition onto the substrate of various materials before selenium evaporation affects electron- or hole-injection properties at the interface. Thus, SeO_2, Te, Ge, and crystalline Se give increased hole injection; As_2O_5 enhances hole and electron injection; and As and ZnS have no effect. Similar effects occur at the free surface of a charged Se plate. Isopropanol and ammonia form a barrier that inhibits the decay of positive surface charge, while the injection is enhanced by ferric chloride, ozone, and chloranil.[139]

Various parameters, such as residual gas, apparatus geometry during the selenium evaporation, and evaporation rate, affect the electrophotographic properties. Substrate temperature during deposition of the selenium has large effects and has been studied in some detail.[139] These effects may involve structural defects, interactions with the substrate, or the formation of crystalline selenium.

The principal effect of impurities and doping is to change the electron or hole range (the mobility-lifetime product). Some impurities act to increase light fatigue which suggests the introduction of trapping states. Red response can be enhanced with a 25% As–Se alloy.[37]

The optical and photoconductive properties of selenium and the light-induced discharge of selenium electrophotographic layers have, until recently, not been well understood. It is well known that the optical absorption edge is shifted to significantly longer wavelengths than the photoconductive edge. For example, light absorption commences at about 6,500 Å, while measurable electrical effects begin at about 5,500 Å, as shown in Fig. 12. Another problem has been the decrease in sensitivity with decreasing voltage as the light-induced voltage decay proceeds.

An explanation has been proposed based on carrier range and recombination effects for the decreasing rate of change of surface voltage as the voltage decreases with exposure to strongly absorbed light.[100] Two effects determine the voltage discharge curve in this model. In the optical generation region, recombination occurs which reduces the quantum efficiency. Also, as the holes drift through the bulk to the substrate, some are captured in deep trapping states. The limitation

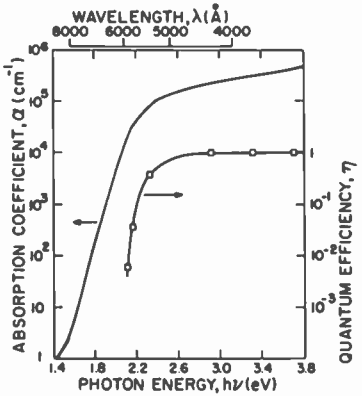

Fig. 12—Optical absorption coefficient and quantum efficiency for vitreous selenium at room temperature. (Adapted from J. L. Hartke and P.J. Regensburger, "Electronic states in vitreous Se," Phys. Rev., vol. 139, p. A970, 1965.)

on the sensitivity depends on the ratio of the average distance traveled by a carrier, $\mu\tau E$, to the sample thickness L, where μ is the mobility, τ is the carrier lifetime, and E the electrical field. In the model, the range, $\mu\tau$, limits the distance traveled by carriers to a fraction of the sample thickness. This limitation demands that the sensitivity of a layer depend on both field and thickness. Also, since the carrier range is limited by trapping within the layer, a signficant residual potential must result if the decrease in slope of the voltage decay curve is ascribed to a range limitation.

Tabak and Warter[155, 156] point out that these two requirements are *not* met. The sensitivity does not depend on sample thickness, but only on field, as shown in Fig. 13. Thus, a model dependng on carrier range cannot explain the light-induced voltage decay curve. Also, observed

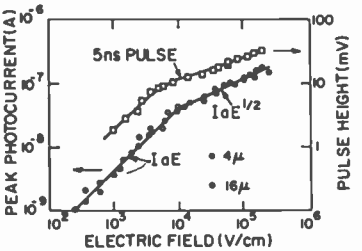

Fig. 13—The lower data show the hole-photocurrent-applied-field characteristic as a function of sample thickness for a 4300 Å msec light exposure. The upper curve gives the total voltage pulse height (integral of the current) as a function of the applied field for a 5 nsec exposure. (Adapted from Ref. 150.)

residual voltages are too low to fit the range-limited model. The field, temperature, and wavelength dependence of the photosensitivity imply a field-dependent optical generation process.[128, 155] Viscakas has also advanced this suggestion.[165] An absorbed photon generates a tightly bound electron–hole pair. Free carriers are then formed by field-assisted thermal dissociation. Reasonable agreement with a simple calculation of the generation rate based on the Frenkel effect[38] is obtained. The field-assisted thermal dissociation process also provides an explanation for the lack of photoconductivity at the longer wavelengths absorbed by selenium. At these longer wavelengths, a bound pair is formed, but the thermal and electrical potential energy are insufficient to dissociate the pair.

While the number of holes captured within the bulk of the selenium layer during any one photodischarge is insufficient to explain the decreasing voltage decay rate by a charge fatigue effect, it has been shown[144] that a small fraction are captured in each discharge and, that after many cycles, the captured holes form a nearly uniform positive space charge within the layer. This captured space charge is responsible for cycling "fatigue."

Zinc Oxide-Resin Binder Layers

The most widely used electrophotographic pigment-resin binder layers contain photoconducting ZnO powder as the pigment. The ZnO grains may be classified grossly as parallelopipeds with dimensions of 0.3 to 0.4 microns. Since ZnO is the commercially important pigment, much more effort has been devoted to understanding this system than others.

Zinc oxide is an n-type semiconductor and a photoconductor. Light of wavelength shorter than about 3,850Å is strongly absorbed and induces photoconductivity.[117] Some absorption and photoconductivity may extend into the visible depending on impurity content or stoichiometry.

Large single crystals of ZnO are normally conducting unless suitably doped. In powder form, however, the large surface-to-volume ratio of the ZnO grain enables surface effects to dominate the bulk electrical properties of the grain. A well-known example of the dominance of surface effects in ZnO is the influence of oxygen on the conductivity, which has been studied in ZnO thin films, powders, and single crystals.[15, 59, 63, 117, 172] These experiments suggest that adsorbed atomic or molecular oxygen from the ambient captures ZnO conduction-band electrons and immobilizes them in a chemisorbed oxygen surface state. The effect of the oxygen is illustrated in Fig. 14. Heating or optical excitation can neutralize the chemisorbed oxygen which may then be

removed into the ambient. In this manner, ZnO can be cycled between a relatively conducting and a highly insulating state by alternate desorption and adsorption of oxygen.

The importance of chemisorbed oxygen in reducing the conductivity of powder grains is important for the charging properties of ZnO-resin electrophotographic layers.[41, 42, 138] In the absence of oxygen, a large density of free and trapped electrons would be available. Upon negative corona charging, the large positive space-charge density generated by the sweep out of these electrons would result in a very low surface voltage, if any. The voltage drop for this high-density depletion layer would occur across only a small fraction of the layer thickness.

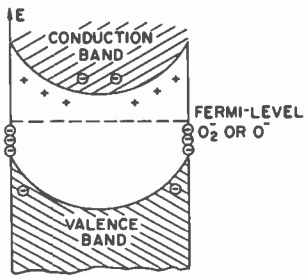

Fig. 14—Insulating effect of chemisorbed oxygen on ZnO powder particle. (Adapted from J.A. Amick, "A review of Electrofax behavior", RCA Review, vol. 20, p. 753, 1959.)

Other substances, in addition to oxygen, affect the surface condition of the ZnO grains. Large effects on the dark and photoconductivity of ZnO powder are induced by water vapor present in the ambient.[89, 125] At low concentrations, the presence of water vapor increases photoconductivity, possibly by an electron liberating reaction with chemisorbed oxygen. At high concentrations, photoconductivity decreases due to trapping of conduction band electrons by chemisorbed OH^-. The humidity dependent properties of the binder layer have been studied by using metallic or other substrates whose conductivity is not humidity dependent.[61]

Many additives and binder modifications for ZnO-resin layers will cause modification of maximum surface voltage, dark decay rate, light sensitivity, and light adaptation properties. Very little is known about the actual mechanisms involved, but the phenomena suggest that these additives are surface active agents for the ZnO grains and that they alter the charge-carrier concentration of the grain in a way similar to the oxygen effects.

Coating properties depend on resin dielectric constant and acidity. Coatings with nonpolar banders (dielectric constant below 2.7) have relatively low saturation voltage while polar binders (dielectric constant above 3.0) contribute to a higher top voltage.[120] Increasing resin acidity results in higher saturation voltage.[157] If the polar and acid groups act to immobilize ZnO conduction band electrons by trapping at the grain surface, then the higher voltage obtained with such coatings represents a decrease in the electron concentration available to be swept out upon corona charging. Positive space-charge density is relatively low or negligible in such coatings and, for a given surface-charge density, the measured surface voltage is higher.

Polar and acidic resins decrease the voltage decay rate under illumination. Several mechanisms are possible. The acid groups may act as deep traps for the optically generated carriers, or the higher acidity resins may wet the ZnO more completely during the dispersion process. Compared to less acid resins, more resin would separate the ZnO grains from each other and the motion of carriers would be inhibited. This encapsulation effect was demonstrated by Kurita[94] who measured the photosensitivity of charged electrophotographic layers of ZnO with stearic acid as binder. For less than monolayer coverage, the sensitivity was comparable to that of the usual layer. At and above monolayer coverage, the photosensitivity was decreased by a factor of 100. It was concluded that, in the normal layer, the ZnO grains touch each other.

A large variety of coating additives have been described. Electron acceptors such as H_2O_2, benzoyl peroxide, and potassium permanganate increase the maximum surface voltage.[105] Several materials are reported to decrease the voltage decay rate in the dark.[24, 43] Cupric ion decreases the effects of light adaptation.[34] On the other hand, reducing agents increase the dark-decay rate.[10] These various effects are consistent with a charge transfer mechanism occurring at the grain surface which immobilizes or, in the case of the reducing agent, frees carriers.

With negative polarity charging on a dark adapted ZnO-resin layer, a large fraction of the charge is distributed as in a simple capacitor.[41, 42, 138] This reveals the highly insulating state of the ZnO crystals resulting from the immobilization of electrons at the crystal surface as discussed previously. When light adapted, a negatively charged layer exhibits a greater positive space charge, which accounts for the well-known decreased sensitivity with previous light exposure. Amick[2] has used the light-induced voltage decay to measure the space charge density which varied greatly depending on the ZnO type. Hoesterey[67] has measured the dependence of the saturation negative

potential on sample thickness. The saturation voltage increased with thickness up to a critical thickness beyond which the voltage was constant. This behavior is interpreted in terms of a depletion-layer model. The maximum depletion-layer thickness is given by the surface-charge density (limited by breakdown) and the charge density in the depletion region. Increasing the sample thickness beyond this critical thickness will not increase the voltage, since no field or voltage drop exists outside the depletion region. Hauffe and Stechemesser[61] suggest that the surface negative charge is not confined to a surface plane, but is distributed over some distance near the surface of the layer.

It seems clear that depletion-layer effects are important in the charging properties of ZnO-resin layers. Very few workers have considered the surface voltage *and the charge* as independent parameters. This is the only way one can study the depletion-layer properties. Several techniques have been used. Ruppel, Gerritsen, and Rose[41, 42, 138] measured the charge delivered while charging up the layer. Amick[2] used known amounts of charge generated by light for the neutralization of the deposited charge. Recently, the neutralization of the surface charge with known amounts of opposite-sign corona charge has been used to measure charge density and charge geometry of ZnO-resin layers.[19, 20] This technique eliminates the complicating effects of conduction through low resistivity paths, breakdown near the maximum voltage, and the complicating effects of light. Further, it can be used to study the charge density and geometry of layers after partial dark or light discharge.

Thus far, the possible influence of inhomogeneities on the charging properties have been ignored. Elder[31] found that larger currents could be passed between a high voltage point corona source and a grounded metal plate when the plate was covered with a ZnO-resin layer. This surprising result suggests that a positive ion discharge takes place at the surface of the layer while it is being charged, resulting in the increased current. The positive discharge, which is sometimes accompanied by visible light emission, occurs at high field regions on the surface associated with the inhomogeneous structure of the layer. Hoesterey[67] also has suggested that the microscopic inhomogeneities of the coating are important and that breakdown occurs in localized spots. Surface voltage is limited, then, not by a uniform breakdown, but by the fact that the corona current flows through localized conducting spots. Recent papers describe techniques for studying the inhomogeous, grainy nature of ZnO–resin binder layers.[70, 111]

Many ZnO-resin binder layers do not accept as high a positive

surface voltage as they do negative, and the positive voltage decays more rapidly in the dark than the negative. The importance of the substrate in positive charging has been demonstrated.[61] As discussed for the ideal photoreceptor, the blocking nature of the substrate contact is important when the surface charge is of sign opposite that of the majority carrier. The electrical properties of the layer are also important, since it is observed that, with a given substrate, the positive charging properties vary with the ZnO and resin used.[176]

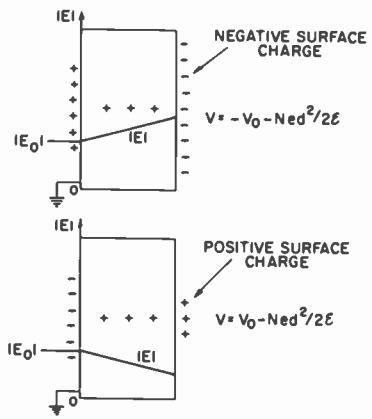

Fig. 15—Schematic of charge and field in a layer for two polarities. The voltage is limited by the same substrate breakdown field in each case.

Simple electrostatic considerations suggest that, if surface voltage is limited by breakdown at the substrate, the presence of space charge in the layer will have a large effect on the difference between the magnitudes of the maximum surface voltages for negative and positive charging. For the simple case illustrated in Figure 15, the difference in the magnitudes of maximum surface potential is given by

$$\Delta V = |V_-| - |V_+| = Ned^2/\epsilon$$

where Ne is the space-charge density and d the thickness. The breakdown field at the substrate is assumed to be independent of polarity.

Several processes may contribute to the dark decay of the surface voltage of pigment binder layers. These include the release of charge from the corona deposited ions by thermal excitation or tunneling, electrical breakdown or injection at the surface or substrate, and the

generation of free carriers from traps in the volume of the sample. Inhomogeneities in the layer may lead to varying decay rates in different surface regions.[31, 67]

The parameters affecting dark decay have been investigated for negative surface charging. Inoue[76] found that the dark-decay rate varied only slightly with the ratio of ZnO to silicone resin binder. For the same materials, the dark resistivity varied two orders of magnitude over the same range of pigment–binder ratio. There is no necessary connection between the resistivity of a material (as measured with ohmic or nonblocking contacts) and its surface charge-storage properties. Very high humidity leads to very rapid dark decay rates.[61] Dark decay is faster when the ZnO-resin mixture has been milled for protracted periods.[60]

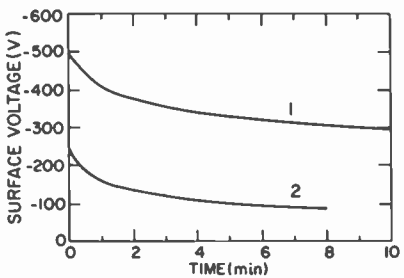

Fig. 16—Dark decay of negative surface charge of ZnO-silicone resin layer; 1, in oxygen; 2, in air. (Adapted from K. Hauffe, "Electrophotographie", Die, Naturavissenschaften, vol. 54, p. 181, 1967.)

Hauffe and Stechemesser[61] suggest that the usually observed initial rapid voltage decay shown in Fig. 16 is due to electron tunneling from surface states, and that the slower decay at lower voltage is due to space-charge formation as formulated by Schaffert[139] for selenium layers. However, in a study of the electrophotographic properties of single crystals, Kiess[85] found little dependence of the dark decay on field, which seems to rule out a tunneling process, at least for the single crystal.

Various forms of the light-induced voltage-decay curves with time have been reported. Fig. 17 shows two representative curve shapes. Different samples of ZnO-resin layers yield different response curves, or a difference in sample history or illumination intensity can yield these two different shapes.

One of the earliest published analyses of light-induced voltage decay

by Gerritsen, Ruppel and Rose[41, 42, 138] showed that the discharge is due to a primary, saturated photocurrent above several hundred volts, where recombination is negligible; that trapping of electrons leads to very long rise times for the photocurrent and to the low sensitivity initial portion of the voltage decay curve; that hole motion was less than 10^{-5} cm; and that the quantum efficiency of the discharge process was close to unity.

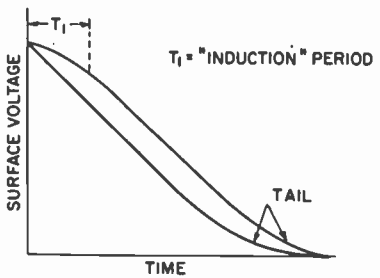

Fig. 17—Two characteristic shapes of photodecay of ZnO-resin layers. Induction period or tail may be more or less pronounced.

Amick[3] studied the light discharge of layers produced with various ZnO powders by a pulse method. Coatings with a maximum surface voltage of 400 volts or greater exhibited a pulsed light-discharge curve that was approximated by a linear region at high voltage followed by a quadratic at lower voltages. The linear region was related to the primary saturated photocurrent in a simple capacitor geometry, while the quadratic or curved region was related to the neutralization of a positive space charge. Coatings that charged only to low voltages exhibited only a curved region.

A study of response times showed that the characteristic S curve was a function of pre-illumination, the illumination intensity and wavelength (UV or visible), and the surface votlage.[4] Pre-illumination decreased the low-sensitivity portion at the top of the S curve. These and other effects were attributed to trapping of the electrons by positively charged centers. The initial slow part of the decay corresponds to the filling of traps; electrons are captured and therefore drift only part way to the substrate, and the sensitivity increases. One may calculate a trap cross section for such a process assuming a mobility μ of 1 cm^2/V-sec and a trap density N of about $10^{14}/cm^3$. This trap density is a reasonable value based on the typical S-shaped decay

curve. The trap cross section is

$$\sigma > \frac{\mu V}{NvL^2} \approx 10^{-13}\ \text{cm}^2$$

where v is the thermal carrier velocity ($\sim 5 \times 10^7$ cm/sec). Thus, the cross section is that of a coulomb attractive center and this supports the model.

The slow initial portion of the light decay has also been attributed[60] to recombination of photogenerated electrons with oxygen atoms or molecules at the ZnO surface, resulting from the neutralization of negative ions by the photoexcited holes. The neutral atoms or molecules gradually desorb and the recombination then decreases.

The previous models for the discharge have assumed a homogeneous layer. The rough surface and particulate nature of the pigment-binder layer may provide alternate explanations, which are difficult to test. The Zn0-resin layer has been pictured as a layered structure of potential barriers. The discharging of these barriers requires a certain amount of photoexcited electron–hole pairs, which results in the slow initial discharge.[166] However, such a barrier model requires weakly absorbed light for discharge.[171] Strongly absorbed light (UV) would only produce a partial discharge. It is well-known, however, that UV light results in complete discharge with a quantum efficiency near unity.[18,41,42,138]

Other Pigment-Binder Layers

Electrophotographic titanium dioxide binder layers have been studied by Nozaki and Iida.[126] The charging properties depend on the binder; for example, a silicone resin layer has too fast a dark decay, while a polyester resin is more suitable. Milling beyond 20 hours decreases the saturation voltage and the light sensitivity. Several dyes that sensitize the TiO_2 layer are listed. In a later paper, the same authors reported a systematic study of the dependence of electrophotographic properties on the resin and proportions used.[73] It was found that resins with a higher dielectric constant contributed to a faster recovery from light adaptation.

The dependence of surface voltage and light decay on the thickness of CdS binder plates has been analyzed in terms of a range-limited model.[151] It is surprising that even for a 216-μm layer there was no evidence of space charge. This requires that the trap density be less than $10^{12}/\text{cm}^3$. ZnCdS binder plates for a transfer process have also been

studied.[14] Decreased fatigue effects and sensitivity comparable to amorphous selenium are claimed for a co-precipitate of CdS and $CdCO_3$ dispersed in acrylic resin.[104]

Organic Photoconductors

Gutman and Lyons[57] discuss the photogeneration processes in organic materials. Intrinsic photogeneration is characteristic of the bulk photoconducting material itself and may be a one- or two-quantum process. Intrinsic one-quantum processes include the formation of charge carriers by direct ionization, which has a small probability in most organic materals, and the production of bound carrier pairs, excitons, that are dissociated to form charge carriers by thermal energy or electric field ionization. Two-quantum processes are not expected to be important in electrophotography because of the low quantum efficiency. Extrinsic processes include the photoexcitation of trapped carriers and the interaction of excitons with impurities or surfaces. The product of the latter process is usually a free hole and a bound electron.

Pohl[132] has reviewed the influence of structure on the electrical properties of organic materials. The electrical properties of a polymer depend on a mixing of electron orbitals of the constituent atoms or molecules forming the polymer. Thus, all semiconducting polymers are conjugated, that is, possess a series of alternately single and double bonds along the polymer chain. Such a structure leads to the orbital overlap required for charge carrier mobility. Not all conjugated polymers possess this overlap, however, since various structural parameters, such as the presence of an interfering side group, can disturb the electronic interaction among the single-and double-bonded atoms or molecules. The importance of conjugation and the general features of photoconductivity in organic materials have been summarized by Weigl.[173]

A large variety of organic materials have been proposed for electrophotographic use. These may be grouped into three classes — thin films of molecular solids (such as anthracene), solid solutions (molecular dispersions) of photoconducting materials in insulating binders, and photoconducting polymers.

One of the first materials used in electrophotography was sublimed authracene.[139] Such plates, and other thin films of organic molecular solids, are usually not sufficiently sensitive for practical use. A large literature describing conductivity and photoeffects in such materials exists (see, for example, Gutman and Lyons[57]), but there are few reports of electrophotographic use.

The leuco bases of triphenylmethane dyes are interesting examples of molecular dispersions of organic photoconductors in an insulating matrix or binder as first reported by Greig[49] and later explained by Mehl and Wolff.[109] In particular, the leuco base of malachite green as the photoconductor in a polyvinylchloride copolymer or sucrose benzoate inert binder was studied. A trace amount of the leuco base is oxidized after the layer is formed and acts as a spectral sensitizer. The photoconduction proceeds by a thermally activated carrier "hopping" between leuco base molecules.

Among the photoconductive polymers, polyvinylcarbozole (PVK) has received much attention. Hoegl[66] reported on the dye sensitization and Lewis acid doping of PVK. Charge-transfer effects associated with acceptors and donors affected the photoconductivity. The degree of polymerization was not important. The dye sensitization and chemical doping of PVK was studied by Hayashi.[62] It was found that cationic (basic) dyes were better sensitizers than anionic (acidic) dyes. The addition of strong acids or acceptors increased fatigue due to carrier trapping. Malachite green dye sensitized photoeffects in PVK have been studied.[127]

The optical generation and transport of carriers in PVK has been examined.[20,134] Trapping of carriers was negligible and both the carrier generation efficiency and mobility were proportional to the square of the electric field. Some sort of field-activiated process thus governs the transport. A recent patent describes a higly photosensitive layer composed of PVK and 2,4,7-trinitro-9-fluorenone.[149] Schaffert has described the electrical and optical properties of this layer.[142]

Many other organic materials have electrophotographic applications. Table 1 lists some of these materials and references or patents. Various other materials have been proposed for electrophotography, most for a toner transfer process. These are listed in Table 2.

3.3 Spectral Sensitization

The sensitization of photoelectronic and chemical phenomena in solids is of great commercial and scientific interest. Silver halide photography, as we know it, exists only because of the spectral sensitization of the silver halide grains by organic dyes. In many forms of electrophotography, sensitization is needed to extend the spectral response of the photoconducting layer into the visible spectrum. This increases the sensitivity to normal light sources and permits the copying of colored material.

Table 1—*Organic Photoconductors for Electrophotography*

Author(s)/Inventor(s)	Reference(s)	Material(s)
P. M. Cassiers et al	*Belg.Pat.* 588,050 8/26/60 589,994 589,995 590,299	Vinyl polymers
P. M. Cassiers et al	USP 3,113,022 12/3/63	Photoconducting vinyl with diazonium salt
P. M. Cassiers et al	Can.Pat. 678,920 1/28/64	Photoconducting polymers
P. M. Cassiers R. M. Hart	Belg.Pat. 599,627 5/16/61	Photoconducting polymers from Friedel-Crafts catalyst
P. M. Cassiers R. M. Hart	USP 3,240,594 3/15/66	Halogenated polymers
P. M. Cassiers J. F. Willems	USP 3,140,946 7/14/64	6-hydroxy-2-phenyl-3-(*p*-dimethyl aminophenyl)-benzofurane
P. Chiorboli et al	*Ric.Sci.* 38 (9) 796 (1968) (English)	Dibenzothiophene
L. A. DuPlessis	USP 3,440,044 4/22/69 Dow	Anthroic acids and metal anthroate salts
C. J. Fox	Brit.Pat. 1,143,340 2/19/69 Kodak	4-diphenyl amino chalcone pigment in binder
C. J. Fox	USP 3,265,496 8/9/66	Tertiary amine
C. J. Fox A. L. Johnson	USP 3,387,973 6/11/68	Triphenylamines
O. Gorgon	Czech Pat. 127,914 6/15/68	Pyrazolines
H. G. Greig	*RCA Review* 23, 413 (1962)	Solid solution of photoconductor in binder
Y. Hayashi	*Bull.Chem.Soc.Jap.* 39, 1660 (1966)	PVK
Y. Hayashi et al	*Bull.Chem.Soc.Jap.* 39, 1670 (1966)	Polyacenaphthylene and PVK
Y. Hayashi H. Oido	USP 3,438,773 4/15/69 Matsushita	PVK formulation for continuous tone
W. A. Hewitt A. H. Sporer	USP 3,341,472 8/26/63	Condensation of 9 Na- carbazone
H. Hoegl	*J.Phys.Chem.* 69, 755 (1965)	PVK with electron acceptors

(continued on next page)

Table 1 (Contd.)

Author(s)/Inventor(s)	Reference(s)	Material(s)
H. Hoegl	Germ.Pat. 1,127,218 4/5/62 USP 3,287,114-123 11/22/66	Lewis acids as sensitizers for organics
H. Hoegl et al	Can.Pat. 678,946 1/28/64	Polymerized vinyl heterocyclic cpd.
H. Hoegl	Can.Pat. 678,948 1/28/64	Polymerized aromatic cpd.
H. Hoegl H. Schlesinger	USP 3,307,940 3/7/67	Polyacrylamides
M. Ikeda et al	*Jap.J.Appl.Phys.* 8, 759 (1969) English	PVK Sensitization
A. Inami et al	*Bull.Chem.Soc.Japan* 37, 842 (1964)	Nitroderivatives of polyvinyl aromatic compounds
A. Inami et al	Jap.Pat. 41-18,309 10/20/66	Polyacenaphthylenes
A. Inami et al	Jap.Pat. 42-19,751 10/4/67	Poly-3, 6-dibromo-9-vinylcarbazole
A. Inami K. Morimoto	Germ.Pat. 1,264,954 3/28/68 Matsushita	Polymers with donor and acceptor units
J. E. Jones	*J.Opt.Soc.Amer.* 59, 877 (1969)	Absorbance and response of organic photoconductor
H. Kosche	Belg.Pat. 702,458 2/9/68	Metal complexes and chelates
H. Kosche	Germ.Pat. 1,296,001 4/12/62 Renken-Belipa GmbH	Reaction products of isocyanates with organic compounds
H. Kosche	French Pat. 1,540,858 9/27/68 Renken-Belipa GmbH	Various organic photoconductors
A. I. Lakatos J. Mort	*Phy.Rev.Letters* 21, 1444 (1968)	Photoemission into PVK
F. A. Levina et al	USSR Pat. 169,395 12/18/65	Sensitization of PVK
J. Mammino	USP 3,408,187-189 10/29/68 Xerox	Lewis acids in resin
J. A. Mattor	Belg.Pat. 661,438 9/22/65	Condensation of p-phenylenediamine with halogenated compounds
J. A. Mattor	USP 3,314,788 4/14/66	Tetra-substituted *p*-phenylene diamines

Table 1 (Contd.)

Author(s)/Inventor(s)	Reference(s)	Material(s)
J. A. Mattor et al.	USP 3,290,147 12/6/66	Arylideneazine
Wolfgang Mehl N. E. Wolff	*J.Phys.Chem.Solids* 25, 1221 (1964)	Solid solution of photoconductor in binder
K. Morimoto et al	*Bull.Chem.Soc.Jap.* 36, 1651 (1963)	Pyrazolines
K. Morimoto et al	*J.Polymer Sci.Part* A-1 5, 1699 (1967)	Reaction products of poly(9-vinyl anthracene)
K. Morimoto et al	Jap.Pat. 42-9,639 4/18/67	Poly-*N*-vinyl-3-aminocarbazole
K. Morimoto et al	*Nat.Tech.Report* 15 #2 4/69 (Japanese)	PVK
K. Morimoto A. Inami	Jap.Pat. 41-17,907 10/13/66	ZnO in photoconducting binder
K. Morimoto Y. Murakami	*Applied Optics*:Suppl. on Electrophot., 50 (1969) 1st Int. Conf. Electrophot. Rochester	Poly-3, 6-dibromo-N-vinyl carbazole
V. S. Myl'nikov	*Russ.Chem.Reviews* 37 (1), (1968)	Polymer optical properties review
W. Neugebauer et al	Brit.Pat. 836,148 11/26/63	Triazole compound
W. Neugebauer et al	Brit.Pat. 938,434 10/2/63	Diarylimidazole
W. Neugebauer et al	USP 3,245,783 4/12/66	Amino compounds
K. Okamoto et al	*Bull.Chem.Soc.Jap.* 41, 2563 (1968) (English)	Sensitized PVK
T. Prot J. Jedrzejewski	*Bull.Acad.Pol.Sci.*, Section Math., Astron., Physics 17, 319 (1969) (English)	Acenaphthene formaldehyde resin and its nitro derivatives
P. J. Regensburger	*Photochem.Photobiol.* 8, 429 (1968)	Injection from Se into PVK
L. D. Rozenshtein et al	USSR Pat. 207,723	Electron acceptors in polymers
H. Schlesinger	Ger.Appl.Pat. 1,110,007 3/18/59	1, 2, 5, 6-tetraazacyclooctatetraenes-(2, 4, 6, 8)
H. Schlesinger	USP 3,294,531 12/27/66	Photoconducting resins
H. Schlesinger	USP 3,130,046 4/21/64	1, 2, 4-triazine compounds

(continued on next page)

Table 1 (Contd.)

Author(s)/Inventor(s)	Reference(s)	Material(s)
H. Schlesinger	USP 3,163,532 12/29/64	Metal complexes of aromatic cpds.
H. Schlesinger J. Munder	USP 3,257,202 6/21/66	Photoconducting polymers
James H. Sharp	*Phot. Sci. & Eng.* 11, 69 (1967)	N-isopropylcarbazole
M. D. Shattuck et al	Brit. Pat. 1,092,618 11/29/67	Activators for persistent conductivity
M. Shattuck U. Vahtra	Brit.Pat. 1,122,458 8/7/68 IBM	Vinyl heterocyclic compound and 2, 4, 7-trinitro-9-flourenone
I. Sidaravicius et al	*Optiko-Mekh. Prom.* 33 #5 27-30 (1966)	Acetylene polymeric compounds
O. Sues et al	Ger.Pat. 1,137,625 10/4/62	Organic colloids with photoconducting compcompounds
O. Sues et al	USP 3,257,203 6/21/66	Triphenyl oxazoles
H. Tani et al	Jap.Pat. 41-18,467 10/24/66	1,1,6,-tetraphenylhexatriene
M. Tomanek	USP 3,290,146 12/6/66	Amine, acid anhydride condensation products
M. Tomanek	USP 3,301,676 1/31/67	Sublimable photoconducting compound
H. Tsukahara et al	*J.Soc.Sci.Phot.Japan* 29, 182 (1966)	Pyrazoline ring compound
J. A. Van Allan	USP 3,250,615 5/10/66	IR sensitizers in photoconducting polymers
C. V. Wilson	Brit.Pat. 1,051,201 12/14/66	Leuco base in binder
C. V. Wilson	FrenchPat. 1,519,059 3/29/68 Kodak	Substituted 1,1,1-triarylalkanes and tetraarylmethanes
	Belg.Pat. 636,038 12/2/63 Ferrania SpA	Pyrazolines
	Belg.Pat. 641,346 6/16/64 Kalle AG	Metallic resinates
	Brit.Pat. 1,079,838 8/16/67	Phenylenediamine compositions
	Brit.Pat. 1,004,929 9/22/65 Kalle AG	1,3,4-thiadiazoles

Table 1 (Contd.)

Author(s)/Inventor(s)		Material(s)
	Brit.Pat. 1,075,626 7/12/67 IBM	Carbazole polymers
	Brit.Pat. 1,146,142 3/19/69 Rank Xerox	Alkyl compounds
	Brit.Pat. 1,062,935 Kalle AG	Amino substituted quinoxaline
	Brit.Pat. 1,101,391	9:10-dimethylene anthracene
	Brit.Pat. 1,046,058 10/19/66	Substituted vinyl carbazole polymer
	Brit.Pat. 1,030,702 5/25/66 Kalle AG	3,3-bis (aminophenyl) phthalide
	Neth.Appl.Pat. 6,406,505 12/21/64	Condensation product polymers
	Neth.Appl.Pat. 6,507,664 12/16/65 Rank Xerox	Phthalocyanine
	Neth.Appl.Pat. 6,609,193 1/2/67 Rank Xerox	Phthalocyanine
	USP 3,331,687 7/18/67	Photoconducting ring systems

Table 2—*Miscellaneous Materials*

Author(s)/Inventor(s)	Reference(s)	Material(s)
A. J. Behringer L. Corrsin	USP 3,238,150 3/1/66	CdS powder
D. W. Chapman F. J. Stryker	*Phot. Sci. & Eng.* 11, 22 (1967)	ZnCdS for charge transfer
Yu Cherkasov et al	*Zh. Nauch. i. Prikl, Fot. i. Kin.* 12, 227 (1967) (Russian)	Sublimed CdS, CdSe, Cd Te
K. Chino et al	*Electrophot.* (Japan) 7, 15 (1966)	CdS evaporated film
K. Makino I. Sawato	Fr.Pat. 1,498,064 10/13/67 Fuji Photo-Film Co.	CdS and $CdCO_3$ coprecipitate

(continued on next page)

Table 2 (Contd.)

Arthur E. Middleton Donald C. Reynolds	USP 3,121,006 2/11/64 Xerox USP 3,121,007	Various materials in binders
E. Mooster H. O. Boelstarlii	USP 3,265,532 6/6/62 Amer. Cyan.	Gallium Sulfide
J. C. Schottmiller R. C. Walborn, Jr.	Fr.Pat. 1,501,511 11/10/67 Rank Xerox	PbO layer without binder
M. Smith A. J. Behringer	*J. Appl. Phys.* 36, 3475 (1965)	CdS in lucite binder
C. Wood et al	USP 3,469,978 9/30/69 Xerox	III-V Compounds
C. Wood et al	Fr.Pat. 1,515,704 3/1/68 Fr.Pat. 1,511,172 1/26/68 Rank Xerox	Fused oxide electrophotographic plates
	Brit.Pat. 1,139,532 1/8/69 Fuji Photo-Film Co.	$CdCO_3$

The essential feature of dye sensitization is that the absorption of light by a dye molecule or film in contact with a sensitizable solid produces the same sort of photoeffects observed when the solid itself absorbs light. For example, the absorption of 3,800 Å light induces photoconduction, photovoltaic effects, and oxygen desorption in ZnO. Some adsorbed organic dyes, absorbing light of a wavelength longer than 3,800 Å, can induce these same effects in ZnO. The question is how the absorption of a low-energy photon by the dye molecule can excite photoeffects in a material that requires higher energy photons to display these photoeffects without the dye.

No detailed model or theory of dye sensitization exists, but two general points of view on this problem are found. In the energy transfer model, the light-absorbing dye molecule transfers its excitation energy to some state in the sensitized solid which then releases a charge carrier into its conduction (or valence) band. In charge transfer, the light ionizes the dye molecule and a charge carrier is transferred directly from the dye to the conduction (or valence) band of the solid. The latter process requires that the sum of the ground-state energy level of the dye molecule in contact with the solid and the excitation energy of the dye (the absorbed photon energy) be at or above the proper carrier band (conduction band for electron excitation). This requirement is illustrated in Fig. 18. Meier[110] has reviewed

dye sensitization and supports a modified charge transfer model, while Terenin and Akimov[161] argue for energy transfer. Measday[108] has also reviewed the subject.

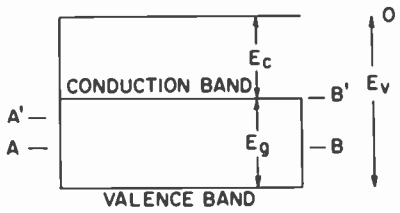

Fig. 18—Energy relations for dye sensitization. E_v = valence band energy; E_c = conduction band energy; E_g = forbidden gap. A and A' are ground and excited states respectively of dye which does not sensitize according to charge transfer model. B dye will sensitize.

Energy levels of dyes on ZnO have been calculated.[160] All sensitizing dyes considered had an excited energy state above the ZnO conduction band edge which is about 4.3 eV below the vacuum level. The excited states of the nonsensitizers were found to lie below the conduction band. This correspondence of sensitizing effect and energy level position is a necessary condition for a charge-transfer process. Akimov et al[1] have measured photoemission of electrons into vacuum from dyed ZnO powder. Their interpretation of photoemission threshold wavelengths indicates that the excited dye states were about 0.8 eV below the ZnO conduction band. This would be strong evidence against charge transfer and for energy transfer. In the calculation of the energy levels, Akimov used 3.2 eV, obtained by photoemission from the ZnO powder, for the ZnO conduction band edge energy. The correct value is about 4.2 to 4.6 eV.[143,154] Photoemission from powders is complicated by the "patch effect" described in detail by Herring and Nichols.[64]

Various aspects of the dye sensitization of ZnO *suggest* a charge transfer process. Thin evaporated ZnO films show a decrease in dark conductivity when a dye layer is applied to their surface from solution, indicating that ZnO conduction electrons are localized by chemisorbed dye molecules.[30]

Various electron acceptor molecules (EAM) are found to increase the dye sensitized photocurrent in ZnO powder layers with ohmic contacts by up to two orders of magnitude.[74] A possible explanation of this increase is that, in the sensitization process, the light excited dye molecule injects an electron into the ZnO and remains in a positively

charged state, or a neutral state if originally the dye is in a chemisorbed negatively charged ground state. In the absence of the EAM, the dye molecule will return to its ground state by capturing a conduction-band electron. In the presence of an EAM, the dye may return to its ground state by charge exchange with the EAM. The EAM will then capture conduction band electrons, but with a lower capture cross section than the excited dye molecule in the absence of the EAM. Thus, the carrier lifetime is increased by the presence of an EAM and photocurrents are enhanced. Note, however, that such a process will *not* lead to the same degree of enhancement in electrophotographic operation, since the surface charge forms a blocking contact and the dye generation efficiency is near unity.[18,21] Further evidence for the interaction of excited dye molecules with charged states is the observation of oxygen desorption from a dye-sensitized ZnO powder due to the excitation by less than bandgap light.[75] In addition, there is evidence that photo-excited dye molecules can act as electron recombination centers.[21] Grossweiner has discussed various aspects of ZnO dye sensitization in terms of an electron acceptor mechanism.[55]

3.4 Reciprocity

If the receptor photosensitivity in terms of response versus incident energy is independent of light intensity, the receptor is said to obey reciprocity. The response then depends only on the product of intensity and time. Thus, an exposure to one microwatt for one second produces the same response as an exposure with one watt for one microsecond.

There has been some question of the reciprocity behavior of electrophotographic materials, but recent work indicates that reciprocity is obeyed for amorphous selenium, ZnO binder layers, and some organic coatings for exposure times ranging from tens of seconds to microseconds.[18,54] Microsecond exposure corresponds to carrier densities of the order of 10^{20} to $10^{21}/cm^3$. At higher intensities, reciprocity failure due to increased recombination would not be unexpected.

4. Development

Of equal importance to the optical response of the electrophotographic layer is the development process for making the latent electrostatic image visible. It is this step that gives the high gain or amplification because of the ease of moving charged particles with electrostatic forces. Without such a gain, electrophotographic reproduction would not have achieved its dramatic commercial success.

4.1 Basic Systems

In developing the latent electrostatic image, the source of the energy for image development plays a significant role in determining the development technique, gain or amplification, and image quality. The two principle approaches for development of a latent electrical image depend on whether the energy is stored in the electrostatic image or comes from an external source. Various methods of image development of photoconductors are listed in Fig. 4. Some development techniques that are based on changes of conductivity and chemical reactivity of a photoconductor are also listed, since these may be combined with electro-

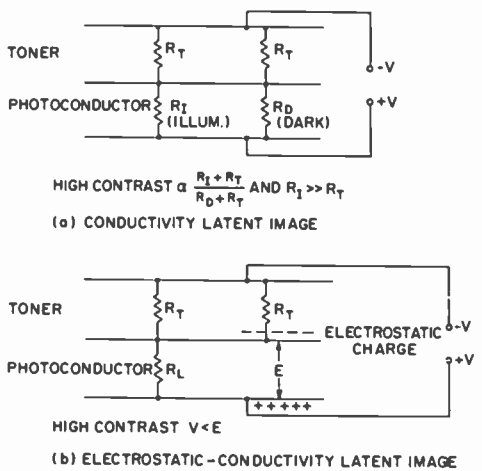

Fig. 19—Equivalent circuits for development with external fields.

static image development. Fig. 19 shows the basic difference between external field electrolytic development and internally stored energy systems. For electrolytic systems, the toner resistivity must be low with respect to the photoconductor resistivity. For electrostatic systems, the toner resistivity must be high to prevent lateral discharge of the latent image. External field control in the latter case can be controlled by special electrode and bias arrangements.[27, 122, 141]

The general approaches to the development of stored-energy electrostatic images in the most widely used commercial systems are the liquid suspended toners for coated-paper systems and powder toners for transfer systems, as shown in Fig. 20.

4.2 Dry Powder Development

Historically, a one-component dry powder toner was the first technique used for developing latent electrostatic images. Because the one-component toners usually contain particles of both signs, a high background deposition occurs and consequently such systems are not extensively used commercially.[16] A more effective way of handling powder toners that has since been developed uses a carrier as a second component. This provides more uniform toner particle charging and simpler transportation of the toner to the latent electrostatic image.[16,27] The most widely used systems are the cascade and magnetic brush techniques.

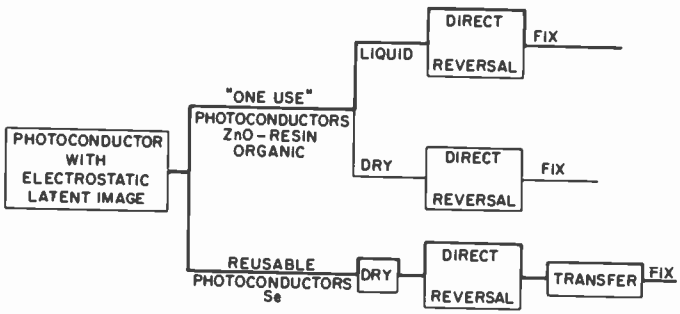

Fig. 20—Schematic diagram showing principle processes in cascade and airborne development.

The carrier particles for the cascade process are insulating particles, while the carrier particles for the magnetic brush process are iron. Both are from 200 to 500 μm in diameter. The toner particles are between 5 and 25 μm in diameter. Typically, there are as many as 3,000 toner particles per carrier particle.

The average charge per toner particle is most commonly determined by a "blow-off" technique.[29] For typical dry toners, the average charge is between 5 and 20 μ coulombs/gram of toner. In direct toning, the reflection density is related to the electrostatic contrast—the difference in potential between the image and background areas. Typical values for these potentials are 650 V in image area and 50 V in background area.

On a microscopic scale, the sign and magnitude of the toner charge is determined by the triboelectric relationship between the toner and the carrier-particle surface composition.[13,58,65,118,119,148] The forces holding the toner particle to the carrier particle are believed to be either

van der Waals[93] or electrostatic.[28,29] In either case, under static conditions, the toner–carrier mixture has very few, if any, free charged particles. The free charged particle becomes available only from the mechanical agitation occurring during the development process. The detachment process is believed to be a combination of an impulse force due to particle-to-particle collisions and a field-assisted detachment force. The work on cascade systems suggests the observed phenomena are in agreement with an electrostatic adhesion theory. Similar forces are presumably acting in the magnetic brush development mode.

FORCE	DEFINING EQUATION	MAGNITUDE
Coulombic	$\vec{F} = q\vec{E}$	$5 \cdot 10^{-4}$ dynes
Polarization	$\vec{F}_p = 2\pi\epsilon_o a^3 \left(\frac{K-1}{K+2}\right) \nabla E^2$	$5 \cdot 10^{-5}$ dynes
Image	$\vec{F}_I = \frac{K-1}{K+1} q^2 \hat{a}/16\pi\epsilon_o a^3$ for $d/a >> 1$	$>5 \cdot 10^{-7}$ dynes
Viscous (Drag Force)	$\vec{F}_v = 6\pi\eta a\vec{v}$ $\vec{v} = \frac{\vec{E}q}{6\pi\eta a}$	Terminal velocity of 300 cm/sec in air.
Gravitational	$\vec{F}_g = mg$	$5 \cdot 10^{-7}$ dynes

Particle: $a = 10\ \mu$m dia.
$m = 5 \cdot 10^{-10}$ g
$q = 5 \cdot 10^{-15}$ coulombs
K = dielectric constant = 3
η = viscosity

[1] Adapted from References 16, 27, 139

Fig. 21—Forces on toner particle in powder development techniques.

The deposition process is the most complex and least understood step in dry-toner development. To obtain a better understanding of the physical processes involved, approximations of the magnitudes of the forces on a toner particle during deposition are listed in Fig. 21.[130]

In cascade development, the two principle mechanisms for the separation and deposition of charged toner particles in the image are contact[130] and airborne development[153] which are illustrated in Fig. 22. Contact development refers to the detachment and subsequent deposition of toner particles that follow field lines essentially perpendicular to the image. Higher toner deposition at potential discontinuities, known as the edge effect, shows that the high electrical fields lead to a higher probability for the field-assisted toner particle detachment. Contact development enhances the edge of solid areas and narrow lines and involves only toner-carrier combinations in the immediate vicinity

of the discontinuity without a development electrode. This mechanism is more pronounced with cascade than magnetic brush systems.

Airborne development refers to the deposition of charged toner particles traveling some distance and not necessarily becoming detached from the carrier directly over the image area. The principle forces on a particle in airborne development are coulombic and viscous. When airborne development is dominant, the deposition occurs toward the center of a solid image area. This is a result of the larger volume element from which the field near the center may influence detached toner particles, as compared to the volume element available for contact development as shown in Fig. 22.

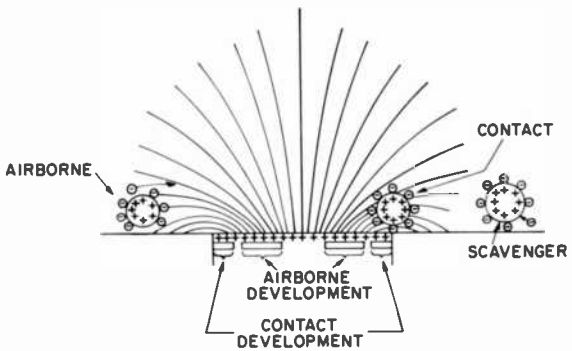

Fig. 22—Development by charged particles in stored energy systems.

A secondary phenomenon occurring is the scavenging of charged toner particles from the background areas by a carrier–toner combination that has a high resistance and has become charged by loss of a toner particle. This tends to reduce the background deposition.

Powder Developer Systems

The configuration of the cascade development system will affect the visible image and the relative role of the above development mechanisms. In general, the preferred mechanism is contact development. This predominates with a development zone angle of $\approx 60°$ in the open cascade and by the use of a development electrode. The development zone angle and toner flow control the distance between the carrier–toner "bounces" and amount of toner in contact with the image area and hence the ratio of airborne to contact development.

The development electrode leads to improved image quality by increasing the field strength in the center of extended areas and reducing the role of potential gradients. Airborne development is reduced because the field lines at close spacing are nearly perpendicular to the image. The improved image quality factors due to a development electrode are higher density in large solid areas and a lower background when biased. The minimum background is controlled by applying a bias voltage to the development electrode to attract toner particles. A typical bias potential is 150 V relative to the photoconductor substrate.

A detailed paper by Bickmore et al[8] describes the interrelationships among flow rate, electroded versus nonelectroded development zone angle, development time, and electrode spacing.

Due to the high electrical conductivity of the magnetic brush, the development mode is principally by contact development with a closely spaced development electrode. Also, the high conductivity in the brush leads to easy application of electrical bias control in direct development and permits reversal development with solid area fill-in.

Important points in the deposition process of dry powder toners are charge buildup on carrier particles and charge transfer between toner and the electrostatic image. Charge buildup on the carrier particles must be prevented because this leads to a field opposing toner deposition.

The nature of the bonding between the toner particle and the electrostatic image plays a significant role in the image quality when using toner transfer for the final copy. For the field-assisted transfer step to be efficient, the bonding should be electrostatic with little charge transfer to the photoconductor. The success of transfer systems, the ability to redevelop an electrostatic image after transfer, and the interpretation of particle adhesion strongly support a model based on electrostatic forces with little charge neutralization by charge transfer.

Transfer

In electrophotographic systems with a reusable photoconductor, the final copy is prepared by transferring the toner to paper.[16,27,139] The image may be transferred by electrostatic or mechanical adhesion or by adsorption forces. The most widely used method is by electrostatic transfer as illustrated in Fig. 23.

Mechanical transfer is accomplished by contacting the toned image with a pressure sensitive tape to which the toner adheres. Several variations based on special toner and adhesive properties of the pressure sensitive tape have been reported. The resolution is claimed

to be greater than 100 line pairs/mm and is recommended for micro-imaging or continuous-tone electrophotography.

In adsorption transfer, the image is developed with dye particles or a dyed toner. The image is transferred to a layer which has been moistened with a solvent for the dye. This technique may lead to low resolution due to dye bleeding.

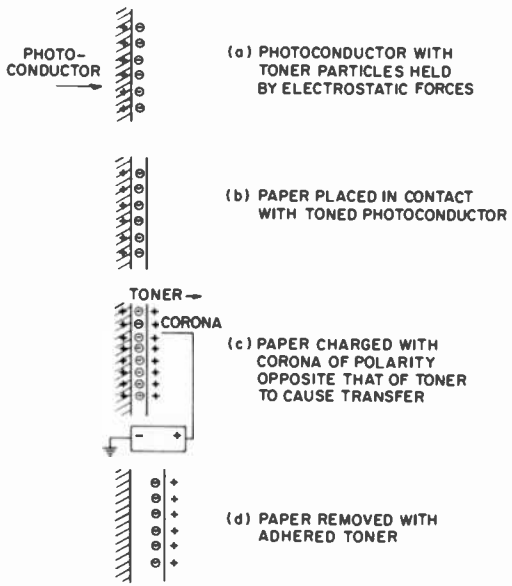

Fig. 23—Toner transfer by electrostatic mode.

Fixing

The fixing of dry toners in most electrophotographic systems is by the application of heat to soften the toner particle. Flash fusing has been considered because it has the advantage in that light is absorbed principally by the colored toner particle and does not heat the paper. Variations in toner composition, binders in single-use photoconductors, and solvent liquid or vapor wetting of toner or paper have been reported for fixing.[16, 27, 139]

4.3 Liquid Development

Liquid development is the most widely used method for developing latent electrostatic images on single-use photoconductors because liquid

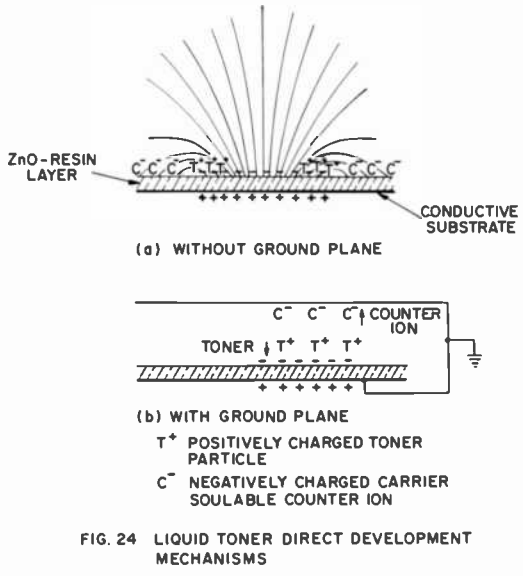

Fig. 24—Liquid toner direct development mechanisms.

toners can be self-fixing and the machine can be simple in design. Liquid toning has come to mean development techniques that are based on the electrophoretic deposition of particles or pigments from insulating liquids. The basic mechanisms are illustrated in Figs. 24 and 25. At present, liquid toners are only applicable to single-use photoconductors; the transfer of liquid toned images has not been demonstrated on a practical basis.

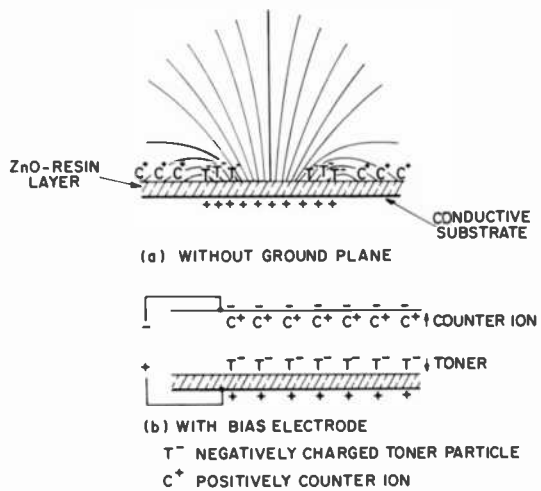

Fig. 25—Liquid toner reversal development mechanisms.

Liquid Toner Composition

A liquid toner consists of

(1) An insulating liquid carrier or vehicle that prevents discharge of the latent charge image. The lower limit on resistivity provided by the self-ionization of the carrier and the nonimaging current carriers is between 10^9 and 10^{10} ohm-cm. The resistivity restriction and the requirements of low toxicity and reasonably high flash points have restricted the choices for carrier fluids to a few aliphatic hydrocarbons. Certain fluorocarbons and silicones have also been considered. The liquids should also have a low dielectric constant to permit a low charge per particle for a given mobility.[27, 51, 52, 112, 113, 139]

(2) The toner particles, which may have a positive or negative charge and a diameter of 0.1 to 40 μm.

(3) A chemical component that charges the toner particle by dissociation. Charge neutrality in the suspension is provided by soluble counter ions.

(4) Charge control resins which coat the toner particle and alter its surface properties to aid in the charging process by providing a more suitable chemical or steric environment.[114]

(5) Fixing resins, which may be in solution or adsorbed on the toner particles, to provide self-fixing of the toner to the substrate upon drying. These resins may serve as the charge control resins or may be electrically inert.[115]

(6) Other components may be used for dispersion of the pigments, e.g., organic titanates. The charge control and fixing resins may also perform this function. Tinting dyes are sometimes added to alter the color of the toner particle.[168]

Charging Mechanism

In contrast to dry toners, the liquid suspended toner particles acquire their charge from a chemical dissociation reaction on the toner particle surface and the solubilization of a charged species in the carrier to form the counter ion. Although the literature on ionization mechanisms in low dielectric liquids is relatively sparse, some trends that may aid in understanding toner charging mechanisms are known.[32, 33, 36, 90, 92, 103, 131] The principle charging mechanisms are

(1) Specific adsorption, usually of a metal cation.[6, 91, 99, 106]

(2) Acid-base reaction between particle surface and counter ion.[36,107]

(3) Ionization of a charge-transfer complex.[102,178]

The specific adsorption mechanism is best illustrated by the oil-soluble metal soaps as follows

$$2MX + TMX \rightarrow [TM\,MX]^+ + X^-MX$$

where TMX is a toner particle with adsorbed MX molecules, MX is an undissociated metal soap in solution, $[TM\,MX]^+$ is a charged toner particle with undissociated MX molecules adsorbed on the toner surface and X^-MX is a counter ion with a micelle structure. For a typical toner particle, the number of undissociated MX molecules will be several orders of magnitude greater than the number of free charges. Conductivity studies on metal soaps in nonpolar solvents indicate that the number of free charges per micelle may be as low as one. The number of MX per micelle is a function of the metal cation,[82,83] water[5,86,87,88] in the micelle and solvent, and solubility of the nonpolar part of the anion in the solvent.[121,162] Typical micelles contain between 5 and 75 molecules. The addition of certain resins has been shown to enhance the ionization of the metal soaps and make the mechanisms more reproducible with carbon pigments.[102]

The acid-base mechanism in its simplest form is the removal of a hydrogen ion from an acidic pigment particle by a solvent-soluble base as follows

$$T{\cdot}H + RB \rightleftharpoons T^- + RBH^+$$

where T·H is an acidic toner particle, RB is solvent-soluble base, T^- is a negatively charged toner particle, and RBH^+ is the positively charged counter ion. The acidic properties of the toner particle may be due to acidic groups on its surface, e.g., —COOH on carbon particles or adsorbed charge-control resins with acid groups. Examples of the solvent-soluble bases are the overbased metal alkyl sulfonates (oil soluble micelles of metal alkyl sulfonates with excess metal hydroxide or carbonate solubilized) and oil soluble polymeric amines.[36,103] As with the MX charging mechanism, the addition of certain resins will enhance and stabilize the charging mechanism.

The above two mechanisms do not explain a number of liquid toners reported in the literature. The best explanation is probably through a generalized acid–base theory including the concept of ionization of charge-transfer complexes.[102] The most applicable work to date is the

role of solvent polarity in particle charging[159] and the application of the Pearson acid–base theory to micelle formation.[36]

The charge stability of the toner is determined by the thermodynamics of the charging reactions and any competing reactions. The particle charge can be altered through concentration changes and the introduction of impurities capable of competing in the charging reaction. The role of water in nonaqueous suspensions is not known.[103] In addition, the high fields associated with electrostatic images may cause desorption of the charge species from the particle surface. Qualitative support for the importance of these factors is that, during electrodeposition of carbon particles from certain toners, some particles first approach the electrode and then reverse direction without striking the electrode.[102]

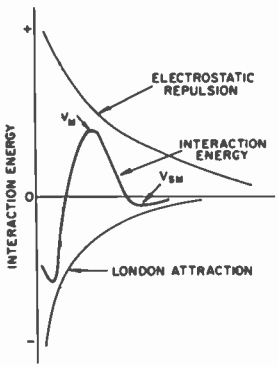

Fig. 26—DLVO theory of colloid stability.

The stability of colloids with respect to flocculation is determined by the interaction of the repulsive and attractive forces between particles. The attractive force that causes flocculation is a consequence of London–van der Waals forces. The forces providing long-term stability can result from electrostatic repulsion of the charged particles and/or steric hindrance due to adsorbed large molecules.

The electrostatic theory of repulsion is by Derjaguin–Landau–Vervey–Overbeek (DLVO).[91, 103, 129, 164] The significant features of the DLVO theory for colloidal suspension are shown in Fig. 26, which shows how the London attraction and Coulombic repulsion forces interact to give conditions leading to flocculation or stable suspension. The significant points determining stability are the potential energy barrier V_m, the secondary minimum for particle attraction V_{sm}, and the role

of particle size. A potential energy barrier of 10 to 15 kT is believed sufficient to prevent rapid flocculation into the primary minimum. Another type of flocculation can occur when $V_{sm} \gg kT$. These flocs contain a liquid film between the particles and can be readily dispersed. Since $V_L \propto a$ and $V_R \propto a^2$, V_m increases with increasing particle size; hence electrical stabilization should be more effective on large particles.

The other major mechanism providing an energy barrier to flocculation is steric repulsion.[103,179] The basic mechanism involves the adsorption on the particle surface of lyophilic groups which extend a reasonable distance into the solvent. The interaction of these chains prevents the close approach required for flocculation. The energy barrier created has been attributed to a loss of configurational entropy on close approach. One of the first good experimental demonstrations of this mechanism was for carbon in various hydrocarbon media with absorbed alkylated aromatic molecules, e.g., tetradecyl naphthalene. Steric repulsion probably occurs for many liquid toners.

Transport Mechanisms

The transport of particles to the charged surface prior to deposition, i.e., to within range of the forces at the paper surface, occurs by three principal mechanisms.

(1) In electrophoretic attraction of charged particles of opposite sign, the force is described by the equation $\vec{F} = q\vec{E}$, where F is the force, q is the particle charge, and E is the electric field.

(2) Dielectrophoretic attraction of polarizable uncharged particles with higher dipole moments than the solvent in nonuniform fields.

(3) Diffusion resulting from the toner concentration gradient at the interface.

The forces on a particle undergoing electrophoretic transport to the deposition site in the low dielectric constant carriers are electrostatic and viscous drag. Frequently, experimental mobilities are used to calculate the zeta potential. The various correction factor used in calculating the zeta potential and particle charge are beyond the scope of this paper.[175] The electrophoretic mobility is a critical factor in the development time because it determines the rate at which particles are brought to the deposition site. A list of zeta potentials and electrophoretic mobilities of several typical particles in low dielectric constant solvents and toners are listed in Fig. 27. The charge per toner particle when extrapolated to a 1 μm diameter is between 300 and 1,100 elemental charges. Experimental measurements give a

value of about 500 charges per 1-μm-diameter particle[47] which is close to that reported for powder toner particles.

Dielectric transport is the result of the force due to a divergent field on polar particles or particles with an induced dipole.[139] Both powder and liquid toners can be moved by these forces. An r^3 term in the force equation becomes important for particles with diameters over 0.4 μm and an E^2 term becomes a factor over 100 V/cm. Dielectrophoretic forces can also occur from the image forces on a charged particle near a polarizable surface. Since typical aliphatic solvents have

PARTICLE	SOLVENT	DISPERSANT	MOBILITY ($\times 10^5$) $cm^2/V\text{-}sec$	ZETA POTENTIAL[1] mv	REFERENCE
Fe_2O_3	Xylene	Aerosol OT	1.43	68	91
Al_2O_3	Xylene	Span 40	0.7	33	91
Carbon	n-heptane	Aerosol OT	1 to 2	19-55	99
Carbon	Benzene	Mg, Ca, Ba dioctyl sulphosuccinates	0.7 to 1.6	30-68	
Commercial Direct	Isopar G		≈1 to 1.2	15-19	102
Carbon Peerless 155[2]	Freon TF	Cooper Naphenate Zirconium Octoate	1 to 1.2	30-37	102
Carbon	Freon TF	OLOA-1200[3]	0.8 to 1.0	24-30	102

[1] Calculated from $\zeta = 6\pi\eta u/\epsilon$, where η is viscosity, u is mobility and ϵ is dielectric constant.

[2] Columbian Carbon Co.

[3] Chevron Chemical Co.

Fig. 27—Particle mobilities in selected solvents.

very low dielectric constants, it should be expected that most organosol particles could be affected by dielectrophoretic forces. In liquid development, dielectrophoretic forces may act to concentrate the suspended particles in areas of high and divergent fields and, thus, may contribute to edge effects and background. These movements of particles to points of high electric fields and formation of deposits are well-known in electric breakdown phenomena in insulating fluids.

Deposition Mechanisms

In the development of a physical model of the deposition process, key points are the role of Debye shielding, the nature of the force overcoming the electrostatic repulsion of the charged particles, and the charge transfer step at the interface. It should be noted that the Debye length, particle-to-particle separation, and dielectric relaxation are local

parameters and during the course of the deposition these parameters will change.[23] The smallest particle diameter for which every toner particle will have a charge is approximately 20 mμ. This can be shown to be a practical limit based on the toner resistivity for usable toner concentrations. The question of this being the smallest particle diameter that can have a unit charge is not established in theory.[23,48,152]

Analytic treatments for direct development have considered the cases in which Debye shielding[3,95] was neglected and in which complete Debye shielding occurred. The former case leads to development times dependent on the mobilities of the charged species that approximate the dielectric relaxation time. The latter leads to a development time dependent on the concentration gradient and toner diffusion constant at the interface. Estimates between 100 and 200 seconds can be made with typical direct toners for a diffusion limited process.[23] The experimental results on direct toners suggest the development is initially mobility limited, followed by a diffusion-limited stage. The role of the photoconductor discharge on development rate has been considered.[152]

For reversal development, the development of discharged areas with toners having the same sign as the surface charge, several more factors must be considered in the deposition step. These are the decay of the surface charge needed to prevent toner deposition in the background, control of voltage variations in background regions, and ability of the toner to inject charge into the layer.[70,71,72,101] As noted above, the decay rate of the surface voltage determines the development time and image density. An electrical equivalent circuit for reversal development including these effects has been described.[71,72] On a local basis, any voltage variations in the background regions will give rise to local cell systems leading to a high background. This can be controlled by use of more uniform coatings, reversal toners with high threshold voltages, and toner particle size larger than the microdefects in the layer.[35,101,107] The background optical density can be as high as 0.25 for a toner with a threshold voltage below 1 volt/cm and a particle size less than 1 μm while for a toner with a threshold voltage greater than 50 V/cm and a particle size greater than 5 μm, the background optical density is less than 0.03.[101]

The deposition mechanism in liquid development has several similarities to electrophoretic deposition from nonaqueous media. Both the anodic and cathodic reactions must be considered. A comparison of the electrode reaction in direct and reversal development to electrophoretic deposition on a conducting substrate is given in Figs. 24 and 25. The following are some points to note:

(1) Reversal development with a bias electrode is the only complete analog of electrophoretic deposition.

(2) The assumption that toner deposition on a free charge on an insulator is the same as electrophoretic deposition on a conducting substrate is reasonable but not fully validated.

(3) Direct and reversal development without a bias electrode or ground plane are analogous if one assumes the counter ions behave as particles instead of discrete ions.

(4) The relative areas and fields above the electrostatic image play a significant role in development time, image quality, and solid-area fill-in. A knowledge of the kinetics of the individual electrode reactions is particularly important to prevent excessive polarization of an electrode reaction.

(5) The use of a ground plane in direct development provides a more uniform field and a less polarizable site for counter ion deposition. Both factors lead to solid-area development and shorter development times. Development electrodes are difficult to use, however, since toner buildup distorts the electrostatic image fields.

The role of the high fields on toner stability has been mentioned. Several theories for electrophoretic deposition have been proposed, none entirely satisfactory. A key point in each of the theories is the nature of the force overcoming the electrostatic repulsion of the charged particles as they approach and accumulate on the surface. There are two principal theories:

(1) Accumulation theory[9]—This is an electrical analogue of a sedimendation mechanism.

(2) Flocculation theory[9,1]—The principal feature of this mechanism is a local buildup of ions at the electrode surface to cause flocculation.

The principal feature of the accumulation theory is that the electric field overcomes the repulsion forces between the particles and permits the particles to agglomerate. This is, in effect, the forcing of the toner particles over the energy barrier in Fig. 26. Agglomeration can occur in a layer adjacent to the electrode if there can be direct deposition on the surface. The buildup of particle layers until the force is sufficient to cause adherence is similar to sedimentation. This theory predicts a dependence on deposition rate, applied voltage, and a critical time for initiation of deposition. A critical time has been noted in a number of references and they tend to support an agglomeration prior to deposition.[9,56] The factors affecting the "critical time" are not well-known. The threshold voltage required to initiate the deposition of

certain liquid toners is probably related to this phenomenon and apparently involves a critical field required to overcome the stabilizing repulsion forces.

The flocculation of colloids can be caused by increasing ion concentration which causes a reduction in size of the ionic atmosphere around the particles. This permits a closer approach of the particles. The flocculation mechanism is based on this buildup of ions formed locally at the electrode interface. In view of the high fields involved, field-assisted dissociation as a means of altering the toner environment cannot be ruled out.

5. Imaging Properties

The optical properties of electrophotographs can be described using techniques similar to those of wet chemical photography. The voltage drop per unit of exposure can be measured. A typical discharge curve is shown in Fig. 28. This is a unique property of electrophotographic systems where, unlike silver systems, the latent image can be measured before development. The amount of toner deposited per unit of voltage is shown in Fig. 28. The amount of toner is measured by its reflection optical density given by the logarithm of the ratio of light reflected from untoned areas to that reflected from the toned area. Finally, an H and D or response curve, can be constructed as shown in Fig. 28, representing image optical density versus exposure.

The S shaped photoresponse curve in Fig. 28 is typical for most electrophotographic systems. On the log exposure plot, there is an initial slow drop in voltage followed by a rapid fall. When the voltage has dropped to a low value, there is a long tail. A rapid drop in voltage and a nonlinear deposition of toner produces a contrasty image. Since high contrast is desirable in reproducing line drawings or office documents, this lack of continuous-tone is an advantage. To obtain good continuous-tone reproduction requires special coatings, photoconductors, and/or development systems.

The optical density of the electrophotographic copy depends on the toner. Powder development systems where a large mass of toner can be fused to the paper will give reflection optical densities of 1.4 to 1.6. Liquid systems where the excess toner and vehicle are removed by squeegeeing will typically give lower optical densities of 1.0 to 1.2.

Edge development, the lack of toner deposition in the middle of large solid areas, occurs because the high fields existing at the charge pattern discontinuity can attract toner faster than the lower fields in large areas. This may be overcome by breaking the large solid areas into

small subliminal dots by screening or by using special development electrodes.

Untoned spots in black areas or toned spots in white areas contribute to background and poor image quality. They are generally due to local breakdown of the electrophotographic layer or to layer defects. Powder toning tends to mask the white holes in a black background because the toner flows during the fixing step. Liquid toners, with their much higher resolution, show up these defects.

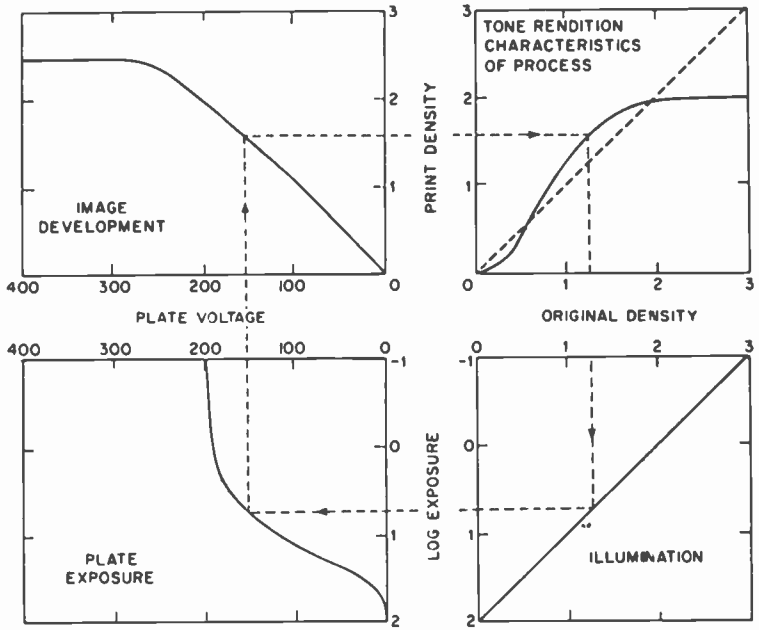

Fig. 28—Four-quadrant chart relating the various steps of the Xerographic process to show relationship of plate-to-print tonal characteristics for powder cloud development of Se plate (from Ref. [27]).

The resolution of the latent electrostatic image is generally limited by the exposure optics. If the image is developed with a two-component powder toner, the toner particle size will limit image resolution to about 10 line pairs per mm. With a one-component powder cloud developer, higher resolutions have been obtained. Liquid toners, with their much smaller size, can produce very high resolution. Images have been made by contact exposure giving 500 lines per mm for liquid development.

6. Applications

6.1 Office Copying

The most important application of electrophotography has been in the convenience or office copy field. In the past decade, this market has grown from a few million dollars to over a billion dollars a year in 1970. In 1960, about 3 million office copies were made primarily using chemical or thermal photographic techniques. In 1970, over 50 billion copies were made by electrophotography.

The use of the dry-powder-toner transfer system is expected to continue its present growth rate and to continue to be the major office copying technology. The most commonly used photosensitive material for this approach is selenium. Other photosensitive materials are also being used, such as a flexible web zinc oxide-binder master, other pigment-binder photoconductors, and organic photoconducting layers.

The direct Electrofax reproduction system using a zinc oxide-binder coating on paper comprises the other major copying technology. Although the coated paper has a different "feel" than ordinary bond, improved aesthetics have come through the development of improved base stock and coating methods, and these advances can be expected to continue. Both liquid and powder toners are used with the coated paper with liquid systems being the most popular.

6.2 Microfilm Printout

A major application of electrophotography is the production of full size, hard copy from microfilm. Direct imaging, toner transfer, and charge transfer systems are used or have been demonstrated. In this application, there is generally more light available than in copying opaque documents so that the restrictions on light sensitivity of photosensitive material can be relaxed.

A complication in this application arises from the fact that both positive and negative microfilm are used. The electrophotographic systems can handle this by changing from direct to reversal toner to produce a positive print irrespective of the sense of the original. This advantage is unique for electrophotography. Changing toner is not a trivial matter, however, and must generally be done by a serviceman. Certain types of insulating photoconductors can be charged positively or negatively, which also permits positive printing irrespective of the sense of the original.

6.3 Nonimpact Computer Printing

Although office copying has been the major user of electrophotography in the past decade, the growing use of computers where the information is in electronic form may lead to electrophotographic output printing. Today, most computer output is by impact printers varying in speed from the 10 character per second electric typewriter terminal to the 20 line per second high speed, multiple copy, chain or drum printer. These machines are noisy, limited in font flexibility, and have no graphic capability. A non-impact electrophotographic printer could solve many of the computer output printing problems.

There are a number of ways of building all electronic non-impact printers. Since the information is in electrical form, it would appear sensible to go directly to some type of purely electrical printing system. Such systems exist. They use pins or probes to charge insulating, coated paper. An electrostatic charge image is formed and toned in the conventional manner used in office copiers. The difficulties of such systems are the need to program and pulse many separate probes whose size and number is determined by the desired resolution of the image. The probes may be charged with an electron beam in a special cathode-ray tube having a line or matrix of insulating pins sealed into the faceplate. When the charge on the pins exceeds air breakdown, there is an electrical discharge between the external end of the pin and the insulating paper, producing an electrostatic latent image. Alternately, insulated pins can be switched at voltages of the order of 600 to 800 V which is enough to cause breakdown. These systems suffer from limited resolution due to the discrete size of the pins and from the cost of the high-voltage switching circuits. Finally, the printout is on coated paper which, while it is not photoconductive, still requires costly coating steps and is considerably more expensive than ordinary paper.

Optical systems using electrophotographic paper have several advantages for non-impact printers. The manufacture of phosphor-faceplate cathode-ray tubes is a mature technology. The tubes are cheap and readily available. Both lens systems to image the phosphor onto the photosensitive paper or lensless systems using fibre optic or thin-window faceplates are available. The resolution is determined by the electron-beam diameter. Separate forms flashing adds another dimension of flexibility. If coated paper is too expensive for high-volume applications, transfer processes are possible using a flexible web-master or a drum as in the office copiers.

6.4 Facsimile

Facsimile, defined here as the technique of creating an image line-by-line rather than character-by-character, is an old art. The printout

systems currently used are primarily electrolytic or impact on carbon ribbon. For telephone line speeds, these are adequate. For systems requiring higher writing speeds such as television multiplexed home facsimile, bandwidth compression systems with nonsynchronous line writing, and wide-bandwidth communication channels, electrophotographic systems can be used. Already several have been demonstrated and others described in the literature.

6.5 Color

Electrophotographic principles can be used to produce color pictures by sequentially imaging each color on the photosensive layer and depositing the appropriate color toner after each exposure. This technique has been used to make multicolor maps from 70 mm separation transparencies and is also used commercially for proofing photographic color separations before making printing plates. Research and development is now under way to use electrophotographic systems to make color pictures from slide transparencies. The main drawback is the time required to carry out the multiple steps of exposing and toning for each color. To overcome this drawback, systems have been described that use photoconducting toner particles to produce color images from a single exposure using electrostatic techniques.

6.6 Printing

Although the major impact of electrophotography has been in convenience copying and low-volume duplicating, there is a continuing effort to find ways to penetrate the 20 billion dollar printing industry. The transient masters with latent electrostatic images are limited to a few copies and charging and re-imaging are needed to produce large volumes of copy. On the other hand, it is possible to make a conventional printing plate electrophotographically. Such a system would be much faster than the presently used optical plate-making methods and, in the long run, may be much cheaper. These plates have the advantage that they may be directly coupled with the computer that is being used for page composition.

Offset electrophotographic plates for duplicating that are capable of several thousands of copies are now on the market. They presently use powder toners that limit their resolution to the point where they are only marginal in reproducing high-quality screened pictures, but high resolution liquid toning can be expected to overcome this limitation.

Letter-press or deep-etch plates have been made with Electrofax

layers on metal where the toner acts to cross-link the ZnO-binder coating. The untoned areas are washed away and the coating acts then as a resist for etching the printing pattern. This is of limited optical quality because of the use of powder toner, but development of improved high resolution liquid toners may eliminate this bottleneck.

7. Conclusions

Commercial electrophotography is only a decade old and in this short time has developed into a billion dollar business. The major use is in the office copying field but, with the information explosion predicted for the next decade, it is expected that electrophotography will play an even more important role in information dissemination. Soft displays such as the familiar cathode-ray tube and the microfilm reader will be used to present information to the consumer, but the printed word, the piece of paper, will still be his major source of reading. Electrophotography is expected to be one of the major means for producing this hard copy.

References:

[1] I. A. Akimov, et al, "External Photoeffect With Dyes Adsorbed on ZnO and the Mechanism of Spectral Sensitization," **Dokl. Akad, Nauk. SSSR Translation,** Vol. 172, p. 371, 1967.

[2] J. A. Amick, "A Volume-Charge Capacitor Model for ELECTROFAX Layers," **RCA Review,** Vol. 20, p. 770, 1959.

[3] I. V. Anfilov and V. M. Fridkin, "Theory of the Development of a Latent Electrostatic Image," **Zhur. Nauch. i Priklad. Fot. i Kinematog.,** Vol. 5, p. 367, 1960.

[4] R. Arneth and B. Lorenz, "Entladungsmechanismus und Gradation Elektrophotographischer Schichten," **Reprographie,** Vol. 3, p. 199, 1963.

[5] W. D. Bascom, et al, "Colloid Aspects of the Performance of Oil-Soluble Soaps as Lubricant Additives," Paper 18, Section II, Fifth World Petrol. Congress, 1959.

[6] G. L. Beyer, U.S. Patent No. 3,417,019, 1968.

[7] E. Berman, "The Itek RS Process," **Seminar on Novel Imaging Systems,** Soc. Phot. Sci. and Eng., p. 21, 1969.

[8] J. T. Bickmore, et al, "Configurational Studies on Cascade Development," **Phot. Sci. and Eng.,** Vol. 14, p. 42, 1970.

[9] J. B. Birks, "Electropheretic Deposition of Insulating Materials," **Progress in Dielectrics,** Vol. 1, New York: Wiley, 1959.

[10] N. W. Blake and C. C. Natale, British Patent No. 1,005,247, 1965.

[11] C. F. Carlson, U.S. Patent No. 2,297,691, 1942.

[12] C. F. Carlson, U.S. Patent No. 2,588,699, 1952.

[13] P. M. Cassiers and J. Van Engeland, "On the Mechanism of Powder Development in Electrophotography," **Phot. Sci. and Eng.,** Vol. 9, p. 273, 1965.

[14] D. W. Chapman and F. J. Stryker, "A Binder Type Plate for Charge Transfer Electrophotography," **Phot. Sci. and Eng.,** Vol. 11, p. 22, 1967.

[15] H. Chon and J. Pajares, "Hall Effect Studies of Oxygen Chemisorption on Zinc Oxide," **J. Catalysis,** Vol. 14, p. 257, 1969.

[16] C. J. Claus, "Electrophotographic Processes and Materials," **Image Technology,** p. 12, Feb./March 1969, p. 29, April/May 1969, p. 16, June/July 1969.

[17] A. B. Cohen, "Photopolymer Imaging Systems," **2nd Symp. on Unconvent. Phot. Systems,** Soc. Phot. Sci. and Eng., p. 122, 1967.

[18] R. B. Comizzoli and D. A. Ross, "Photosensitivity and Quantum Efficiency of Electrofax Coatings," **Phot. Sci. and Eng.,** Vol. 13, p. 265, 1969.

[19] R. B. Comizzoli, "Apparatus and Method for Measurement of Charge Density and Capacitance in Electrophotographic Materials," **Photo. Sci. and Eng.,** Vol. 14, p. 210, 1970.

[20] R. B. Comizzoli and H. Kiess, 3rd European Conf. on Problems in Electrophotography, Aug. 1971, Zurich (to be published).

[21] R. B. Comizzoli, "Quantum Efficiency and Photoconductivity in Dye Sensitized ZnO-Resin Binder Layers," **J. Appl. Phys.,** Vol. 41, p. 4148, 1970.

[22] L. J. M. Daguerre, "The Daguerrotype," **The Literary Gazette and Jour. of the Belles Lettres,** No. 1147, p. 28, 1839.

[23] J. A. Dahlquist and I. Brodie, "Electrophoretic Development of Electrostatic Charge Images from Collodial Suspensions of Carbon," **J. Appl. Phys.,** Vol. 40, p. 3020, 1969.

[24] K. Damm, et al, German Appl. Patent No. 1,157,916, 1961.

[25] G. F. Day, et al, "Electrophotographic and Electrostatic Printing on Dielectric-Coated Paper," **1970 IEEE Int. Conv. Digest,** N. Y., p. 44, 1970.

[26] G. F. Day and R. L. Jepsen, "Photoconductive Gain in Electrophotography," 23rd Ann. Conf. Soc. Phot. Sci. and Eng., 1970.

[27] J. H. Dessauer and H. E. Clark, **Xerography and Related Processes,** London: Focal Press, 1965, Chapter XII.

[28] D. K. Donald, "Electrostatic Contribution to Powder-Particle Adhesion," **J. Appl. Phys.,** Vol. 40, p. 3013, 1969.

[29] D. K. Donald and P. K. Watson, "The Influence of Electric Fields on Particle Adhesion in Xerographic Developer Mixtures," **Phot Sci. and Eng.,** Vol. 14, p. 36, 1970.

[30] S. J. Dudkowski, et al, "Spectral Sensitization of ZnO Thin Films With Organic Dyes," **J. Phys. Chem. Solids,** Vol. 28, p. 485, 1967.

[31] T. Elder, "Interactions Between the Corona Discharge and a Zinc Oxide Electrode," **J. Appl. Phys.,** Vol. 33, p. 2804, 1962.

[32] Faraday Society, "Coagulation and Flocculation," Disc. No. 18, London 1954.

[33] The Faraday Society, "Colloid Stability in Aqueous and Non-Aqueous Media," Faraday Soc. Disc. No. 42, London 1966.

[34] Fuji Photo Film Co., British Patent 1,085,939, 1964.

[35] D. L. Fauser and E. G. Bobalek, U.S. Patent No. 3,507,794, 1970.

[36] F. N. Fowkes, "The Interaction of Polar Molecules, Micelles, and Polymers in Non-Aqueous Media," **Solvent Properties of Surfactant Solutions,** New York: Dekker, 1967.

[37] R. A. Fotland, "Some Electrical Properties of Amorphous Selenium Films," **J. Appl. Phys.,** Vol. 31, p. 1558, 1960.

[38] J. Frenkel, "On Pre-Breakdown Phenomena in Insulators and Electronic Semi-Conductors," **Phys. Rev.,** Vol. 54, p. 647, 1938.

[39] V. M. Fridkin and I. S. Zhodudev, **Photoelectrets and the Electrophotographic Process,** Translation by the Consultants Bureau, New York 1960.

[40] J. Gaynor and J. Aftergut, "Photocharge Process," **Phot. Sci. and Eng.,** Vol. 1, p. 209, 1963.

[41] H. J. Gerritsen, et al, "Properties of Zinc Oxide with Ohmic and Blocking Contacts," **Helv. Phys. Acta.,** Vol. 30, p. 504, 1957.

[42] H. J. Gerritsen, et al, "Photoleitfahigkeit vin Zink Oxyd bei Ohmschen und Sperrenden Kontakten," **Helv. Phys. Acta.,** Vol. 30, p. 235, 1957.

[43] Gevaert Photo-Producten N.V., British Patent 1,020,504, December 29, 1960.

[44] E. C. Giaimo, "Thermoplastic Organic Photoconductive Recording Media—Electrophotographic Characteristics and Processing Techniques," **RCA Review,** Vol. 25, p. 692, 1964.

[45] E. C. Giaimo, U.S. Patent 2,922,883.

[46] H. G. Greig, U.S. Patent 3,117,884.

[47] H. C. Gillespie and H. Wielicki, "ELECTROFAX Specifications for Army 5-Color Map Reproducting Equipment," Final Report DA 44-009-AMC-1730(X) 1968.

[48] H. C. Gillespie, et al, "Continuous-Tone Electrophotography," Final Report Cont. No. DAAK 02-67-L-0176, 1968.

[49] H. G. Greig, "An Organic Photoconductive System," **RCA Review,** Vol.. 23, p. 413, 1962.

[50] H. G. Greig, U.S. Patent No. 3,052,539, 1962.

[51] H. G. Greig, U.S. Patent No. 3,076,722, 1963.

[52] H. G. Greig, U.S. Patent No. 3,053,688, 1962.

[53] H. G. Greig, U.S. Patent No. 2,874,063.

[54] S. G. Grenishin, et al, "Reciprocity in Electrophotography," **Zh. Nauch. i Prikład. Fot. i Kinematog.**, Vol. 12, p. 179, 1967.

[55] L. I. Grossweiner, "Sensitization of Photoconductive Effects in Zinc Oxide," **Photochem. Photobiol.**, Vol. 8, p. 411, 1968.

[56] C. P. Gutierrez, et al, "Electrophoretic Deposition and a Versatile Coating Method," **J. Electrochem. Soc.**, Vol. 109, p. 923, 1962.

[57] F. Gutman and L. E. Lyons, **Organic Semiconductors**, New York: Wiley, 1967.

[58] W. R. Harper, **Contact and Frictional Electrification**, London: Oxford Univ. Press, 1967.

[59] H. Hasebe and E. Inoue, "Effect of Adsorbed Oxygen and Water on the Photoconduction of Zinc Oxide," **J. Chem. Soc. Japan**, Pure Chem. Sect., Vol. 87, p. 332, 1966.

[60] K. Hauffe, "The Electrophotographic Properties of Zinc Oxide," **J. Phot. Sci.**, Vol. 10, p. 321, 1962.

[61] K. Hauffe and R. Stechemesser, "On the Mechanism of the Charging and Discharging of Zinc Oxide-Resin Layers in the Dark and Under Illumination," **Phot. Sci. and Eng.**, Vol. 11, p. 145, 1967.

[62] Y. Hayashi, "Sensitization in Photoconductance of Poly-N-Vinylcarbazole," **Bull. Chem. Soc. Japan**, Vol. 39, p. 1660, 1966.

[63] G. Heiland, "Die Elektrische Leitfahigkeit an der Oberflache von Zinkoxydkristallen," **Z. Physik**, Vol. 142, p. 415, 1955.

[64] C. Herring and M. H. Nichols, "Thermionic Emission," **Rev. Mod. Phys.**, Vol. 21, p. 185, 1949.

[65] P. S. H. Henry, "Generation of Static on Solid Insulators," **J. Text. Inst.**, Vol. 48, p. 5, 1957.

[66] H. Hoegl, "Photoelectric Effects in Polymers and Their Sensitization by Dopants," **J. Phys. Chem.**, Vol. 69, p. 755, 1965.

[67] D. C. Hoesterey, "Effect of Dielectric Breakdown on the Charging of ZnO Xerographic Layers," **J. Appl. Phys.**, Vol. 33, p. 992, 1962.

[68] M. F. Hoover and H. E. Carr, Performance-Structure Relationships of Electroconductive Polymers," **TAPPI**, Vol. 51, p. 552, 1968.

[69] W. C. Huebner, U.S. Patent No. 2,676,100, 1952.

[70] E. C. Hutter, "Relationships Between the Physical Properties of Electrofax Layers and Speckles in Reversal Liquid Toning," Preprints of Paper Summaries, 24th Annual Conf. Soc. Phot. Sci. and Eng., 1971.

[71] E. C. Hutter, "Physical Processes in Reversal Liquid Development of Electrofax Layers," **Phot. Sci. and Eng.**, to be published 1971.

[72] E. C. Hutter and E. C. Giaimo, "Charge Transfer in Electrofax Development by Reversal Liquid Toning," **Phot. Sci. and Eng.**, Vol. 14, p. 197, 1970.

[73] T. Iida and H. Nozaki, "Electrophotographic Properties of Titanium-Dioxide Resin Dispersion Layers," **Bull. Chem. Soc. Japan**, Vol. 42, p. 2820, 1969.

[74] E. Inoue and T. Yamaguchi, "The Hypersensitization of Photoconduction in Microcrystalline Zinc Oxide," **Bull. Chem. Soc. Japan**, Vol. 36, p. 1573, 1963.

[75] E. Inoue et al, "Hypersensitization of Photoconduction in Microcrystalline Zinc Oxide," **J. Phys. Chem.**, Vol. 69, p. 767, 1965.

[76] E. Inoue, "Electrophotographic Properties of Zinc Oxide Dispersed in Dielectric Resin," **Proc. Tech. Assn. Graphic Arts**, Vol. 14, p. 175, 1962.

[77] E. Inoue, et al, "Barrier Properties in Electrophotographic Zinc Oxide," **Applied Optics:** Supplement #3 on Electrophotography, p. 91, 1969.

[78] E. G. Johnson and B. W. Neher, U.S. Patent No. 3,010,883, 1961.

[79] H. Jonker, et al, "Physical Development Recording Systems I. General Survey and Photochemical Principles," **Phot. Sci. and Eng.**, Vol. 13, p. 1, 1969.

[80] H. Kallman and B. Rosenberg, "Persistent Internal Polarization," **Phys. Rev.**, Vol. 97, p. 1596, 1955.

[81] H. Kallman, U.S. Patent No. 2,845,348, 1952.

[82] S. Kaufman, "Effect of the Cation on Solubilization by Oil Soluble Sulfonates," **J. Colloid Interface Sci.**, Vol. 25, p. 401, 1967.

[83] S. Kaufman and C. R. Singleterry, "Effect of the Cation on Micelle Formation by Sulfonates in Benzene," **J. Colloid Sci.**, Vol. 12, p. 465, 1957.

[84] B. Kazan, et al, "Image Recording by Particle Orientation," **Proc. IEEE,** Vol. 56, p. 338, 1968.

[85] H. Kiess, "Investigation of the Electrophotographic Properties of ZnO Single Crystals," **Appl. Optics:** Supplement #3 on Electrophotography, p. 100, 1969.

[86] A. Kitahara and K. Kijiro, "Mechanism of Solubilization of Water by Oil-Soluble Surfactant Solutions I. Anionic Surfactants," **J. Colloid Interface Sci.,** Vol. 29, p. 48, 1969.

[87] A. Kitahara and K. Kijiro, "Mechanism of Solubilization of Water by Oil-Soluble Surfactant Solutions II. Cationic Surfactants," **J. Colloid Interface Sci.,** Vol. 29, p. 1, 1969.

[88] A. Kitahara, et al, "The Effect of Water on the Electrokinetic Potential and Stability of Suspensions in Non-Polar Media," **J. Colloid Interface Sci.,** Vol. 25, p. 490, 1967.

[89] O. C. Klein, "The Effect of Moisture and Type of Binder on Electrophotographic Behavior," **TAPPI,** Vol. 47, p. 145A, 1964.

[90] A. Klinkenberg and J. L. van der Minnie, **Electrostatics in the Petroleum Industry,** Amsterdam: Elsevier, 1958.

[91] H. Koelmans and J. Th. G. Overbeek, "Stability and Electrophoretic Deposition in Non-Aqueous Media," Disc. Faraday Soc., Vol. 18, p. 52, 1954.

[92] J. A. Kok, **Electrical Breakdown of Insulating Liquids,** New York: Interscience, 1959.

[93] H. Krupp, "Particle Adhesion Theory and Experiment," **Advan. Colloid Interface Sci.,** Vol. 1, p. 111, 1967.

[94] T. Kurita, "Photoelectric Properties of Microcrystalline Zinc Oxide Powder Layers With Adsorbed Monolayer of a Long Chain Fatty Acid," **Jap. J. Appl. Phys.,** Vol. 5, p. 977, 1966.

[95] T. Kurita, "An Aspect on the Mechanism of Liquid Development," **Denshi Shashin,** Vol. 3, p. 26, 1961.

[96] E. H. Land, "A New One-Step Photographic Process," **J. Opt. Soc. Amer.,** Vol. 37, p. 61, 1947.

[97] W. R. Lawton, "Recent Advances in Organic-Based Imaging Systems," Seminar on Novel Imaging Systems, Soc. Phot. Sci. and Eng., p. 63, 1969.

[98] R. M. Levy, U.S. Patent No. 3,419,888, 1968.

[99] K. E. Lewis and G. D. Parfitt, "Stability of Non-Aqueous Media, Pt. 3." **Trans. Faraday Soc.,** Vol. 62, p. 1652, 1966.

[100] H. Tung Li and P. J. Regensburger, "Photoinduced Discharge Characteristics of Amorphous Selenium Plates," **J. Appl. Phys.,** Vol. 34, p. 1730, 1963.

[101] G. S. Lozier, "Liquid Toners for Reversal Development of ELECTROFAX Layers," 23rd Ann. Conf., Soc. Phot. Sci. and Eng., 1970.

[102] G. S. Lozier, unpublished results.

[103] J. Lyklema, "Principles of the Stability of Lyophobic Colloidal Dispersions in Non-Aqueous Media," **Advan. Colloid Interface Sci.,** Vol. 2, p. 65, 1968.

[104] K. Makino and I. Sawato, French Patent No. 1,498,064, 1967.

[105] G. E. Mason and O. C. Klein, "Aqueous Electrophotographic Coating," **TAPPI,** Vol. 50, p. 101A, 1967.

[106] J. Matkan, U.S. Patent No. 3,259,581, 1966.

[107] J. Matkan and W. H. Lowe, U.S. Patent No. 3,362,907, 1968.

[108] J. N. Measday, "Review of Dye Sensitization in Solids," **SPSE News,** Vol. 10, p. 4, 1967.

[109] W. Mehl and N. E. Wolff, "Photoconductivity in Dispersed Organic Systems," **J. Phys. Chem. Solids,** Vol. 25, p. 1221, 1964.

[110] H. Meier, "Sensitization of Electrical Effects in Solids," **J. Phys. Chem.,** Vol. 69, p. 719, 1965.

[111] R. Menold, "Structure of Binder Layers Containing Particles," **Chemie-Ingenie Technik,** Vol. 41, p. 725, 1969.

[112] K. A. Metcalfe, "Liquid Developers for Xerography," **J. Sci Instr.,** Vol. 32, p. 74, 1955.

[113] K. A. Melcalfe and R. J. Wright, U.S. Patent No. 3,058,914, 1962.

[114] K. A. Melcalfe, et al, U.S. Patent No. 3,078,231, 1963; H. Greig, USP 3,058,688, 1962.

[115] K. A. Melcalfe and R. J. Wright, U.S. Patent No. 3,198,649, 1965.

[116] C. S. Miller and B. L. Clark, U.S. Patent No. 2,663,656, 1953.

[117] E. Mollwo, **Photoconductivity Conference,** Ed. by Breckenridge, et al, New York: Wiley, 1956.

[118] D. J. Montgomery, Static Electrification of Solids, in **Advances in Solid State Physics,** Vol. 9, New York: Academic Press, 1959.

[119] W. T. Morris, "Static Electrification of Polymers: A Review," **Plastics and Polymers,** Vol. 38, p. 41, 1970.

[120] G. R. Nelson and L. A. Carlson, U.S. Patent No. 3,347,670, 1963.

[121] S. M. Nelson and R. C. Pink, "Solutions of Metal Soaps in Organic Solvents. Part III," **J. Chem. Soc.,** p. 1744, 1952.

[122] E. J. Neugebauer, "Electrostatic Fields in Xerography," **Appl. Opt.,** Vol. 3, p. 385, 1964.

[123] F. H. Nicoll, "A New Surface Phenomenon in Thermoplastic Layers," **RCA Review,** Vol. 25, p. 209, 1964.

[124] R. T. Nieset, "The Basis of the Kalvar System of Photography," **J. Phot. Sci.,** Vol. 10, p. 188, 1962.

[125] J. McK. Nobbs, "The Effect of Water Vapour on the Photoconductivity of Zinc Oxide," **J. Phys. Chem. Solids,** Vol. 29, p. 439, 1968.

[126] H. Nozaki and T. Iida, "On the Study of TiO_2-ELECTROFAX Behavior," Reprographie II, IInd Int. Conf. Colonge, Helwich, Darmstadt, p. 63, 1969.

[127] K. Okamoto, et al, "Sensitization of the Photoconductivity of Poly (N-vinylcarbazole) With Copolymerized Dye Molecules," **Bull. Chem. Soc. Japan,** Vol. 41, p. 2563, 1968.

[128] D. M. Pai and S. W. Ing., Jr., "Photogeneration of Carriers in Vitreous Selenium," **Phys. Rev.,** Vol. 173, p. 729, 1968.

[129] G. D. Parfitt, **Dispersion of Powders in Liquids,** New York: American Elsevier, 1969, Chapters 2 and 3.

[130] E. F. Pickard and H. A. Pohl, **Dielectrophoresis and Electrophoretic Deposition,** New York: Electrochemical Soc., 1967, p. 65.

[131] N. Pilpel, "Properties of Organic Solutions of Heavy Metal Soap," **Chem. Rev.,** Vol. 62, p. 271, 1962.

[132] H. A. Pohl, **Organic Semiconducting Polymers,** Ed. by J. E. Katon, New York: Dekker, 1968.

[133] G. L. Pressman, "Photoelectric Electrostatic Printing," Seminar on Novel Imaging Systems, Soc. Phot. Sci. and Eng., p. 149, 1969.

[134] P. J. Regensberger, "Optical Sensitization of Charge Carrier Transport in poly (N-vinylcarbazole)," **Photochem. Photobiol.,** Vol. 8, p. 429, 1968.

[135] J. J. Robillard, "New Approaches in Photography," **Phot. Sci. and Eng.,** Vol. 8, p. 18, 1964.

[136] A. Rose, **Concepts in Photoconductivity and Allied Problems,** New York: Interscience Publishers, 1963.

[137] A. Rott, "A New Reversal Principle. Reversal Transference by Diffusion," **Sci. and Ind. Phot.,** Vol. 13, p. 151, 1942.

[138] W. Ruppel, et al, "An Approach to Intrinsic Zinc Oxide," **Helv. Phys. Acta.,** Vol. 30, p. 495, 1957.

[139] R. M. Schaffert, **Electrophotography,** London and New York: The Focal Press, 1965.

[140] R. M. Schaffert and C. D. Oughton, "Xerography: A New Principle of Photography and Graphic Reproduction," **J. Opt. Soc. Amer.,** Vol. 38, p. 991, 1948.

[141] R. M. Schaffert, "The Nature and Behavior of Electrostatic Images," **Phot. Sci. and Eng.,** Vol. 6, p. 197, 1962.

[142] R. M. Schaffert, "A New High-Sensitivity Organic Photoconductor for Electrophotography," **IBM Jour. of Research and Development,** Vol. 15, p. 75, 1971.

[143] R. E. Schrader and S. F. Kaisel, "Excitation of Zinc Oxide Phosphors by Low-Energy Electrons," **J. Opt. Soc. Amer.,** Vol. 44, p. 135, 1954.

[144] M. E. Scharfe and M. D. Tabak, "Bulk Space Charge and Transient Photoconductivity in Amorphous Selenium," **J. Appl. Phys.,** Vol. 40, p. 3230, 1969.

[145] F. A. Schwertz, in **Recent Advances in Selenium Physics,** New York: Pergamon Press, 1965.

[146] M. M. Shahin, "Nature of Charge Carriers in Negative Coronas," **Appl. Optics:** Supplement #3 on Electrophotography, p. 106, 1969.

[147] P. Selenyi, "Application of Electrography in Television," **Wireless Eng.,** Vol. 15, p. 303, 1938.

[148] V. E. Shashoua. "Static Electricity in Polymers I. Theory and Measurement," **J. Polymer Sci.,** Vol. 33, p. 65, 1958.

[149] M. D. Shattuck and U. Vahtra, U.S. Patent No. 3,484,237, 1969

[150] J. W. Shepard and B. L. Shely, U.S. Patent No. 3,152,903, 1964.

[151] M. Smith and A. J. Behringer, "Photoinduced Discharge Characteristics of Cadmium Sulfide Binder Layers in the Xerographic Mode," **J. Appl. Phys.,** Vol. 36, p. 3475, 1965.

[152] H. M. Stark and R. S. Menchel, "Kinetics of Electrophoretic Development of Electrostatic Charge Patterns," **J. Appl. Phys.**, Vol. 41, p. 2905, 1970.

[153] W. A. Sullivan and T. L. Thourson, "Studies on the Mechanisms of Cascade Development," **Phot. Sci. and Eng.**, Vol. 11, p. 115, 1967.

[154] R. K. Swank, "Surface Properties of II-VI Compounds," **Phys. Rev.**, Vol. 153, p. 844, 1967.

[155] M. D. Tabak and P. J. Warter, Jr., "Field-Controlled Photogeneration and Free-Carrier Transport in Amorphous Selenium Films," **Phys. Rev.**, Vol. 173, p. 899, 1968.

[156] M. D. Tabak, "Transient Photoconductivity in Amorphous Selenium Films," **Trans. Met. Soc. of A.I.M.E.**, Vol. 239, p. 330, 1967.

[157] D. D. Taft and S. C. Heidecker, "Electrophotographic Paper Binders," **TAPPI**, Vol. 49, p. 439, 1966.

[158] W. H. F. Talbot, "Photogenic Drawing," **The Athenaeum**, No. 589, p. 114, 1839.

[159] K. Tamaribuchi and M. L. Smith, "Charge Determining Species in Non-Aqueous Solvents," **J. Colloid Interface Sci.**, Vol. 22, p. 404, 1966.

[160] T. Tani and S. Kikuchi, "Spectral Sensitization in Photography and Electrophotography," Report Inst. Industrial Sci., Univ. Tokyo, Vol. 18, p. 51, 1968.

[161] A. Terenin and I. Akimov, "Some Experiments on the Photosensitization Mechanism of Semiconductors by Dyes," **J. Phys. Chem.**, Vol. 69, p. 730, 1965.

[162] V. D. Tughan and R. C. Pink, "Solutions of Metal Soaps in Organic Solvents Part II," **J. Chem. Soc.**, p. 1804, 1951.

[163] V. Tulagin, "Imaging Method Based on Photoelectrophoresis," **J. Opt. Soc. Amer.**, Vol. 59, p. 328, 1969.

[164] E. J. Verwey and J. Th. G. Overbeek, **Theory of the Stability of Lyophobic Colloids**, Amsterdam: Elsevier, 1948.

[165] J. Viscakas, et al, "Recombination in Selenium Electrophotographic Layers," **Appl. Optics:** Suppl. #3 on Electrophotography, p. 27, 1969.

[166] J. Viscakas and V. Gaidelis, "The Role of Intercrystalline Barriers in ZnO Electrophotographic Layers," Reprographie II, IInd Int. Conf. Cologne, Helwich Darmstadt, 1969.

[167] O. Von Bronk, British Patent No. 188,030, 1922.

[168] E. W. Wagner, British Patent No. 1,065,796, 1967.

[169] L. E. Walkup, U.S. Patent No. 2,777,957, 1957.

[170] L. E. Walkup, U.S. Patent No. 2,825,814, 1954.

[171] P. J. Warter, Jr., "Factors Determining Xerographic Photoreceptor Performance," **Appl. Optics:** Suppl. #3 on Electrophotography, p. 65, 1969.

[172] H. Watanabe, et al, "The Activation Energy for Oxygen Desorption from Zinc Oxide Surfaces," **Jap. J. Appl. Phys.**, Vol. 4, p. 945, 1965.

[173] J. W. Weigl, **Photographic Science**, Ed. by W. F. Berg, New York: Focal Press, 1963.

[174] R. D. Weiss, "Electrolytic Photography," **Phot. Sci. and Eng.**, Vol. 11, p. 287, 1967.

[175] P. H. Wersema, et al, "Calculation of the Electrophoretic Mobility of a Spherical Colloid Particle," **J. Colloid Interface Sci.**, Vol. 22, p. 78, 1966.

[176] H. Wielicki, private communication.

[177] N. E. Wolff, "A Photoconductive Thermoplastic Recording System," **RCA Review**, Vol. 25, p. 200, 1964.

[178] W. Yellin, et al, British Patent No. 1,016,072, 1966.

[179] W. C. York, U.S. Patent No. 3,135,695, 1964.

[180] C. J. Young and H. G. Grieg, "Electrofax: Direct Electrophotographic Printing on Paper," **RCA Review**, Vol. 15, p. 469, 1954.

[181] Anon., **Electronic News**, p. 68, February 16, 1970.

RCA Technical Papers First Quarter, 1972

January

"Birefringence of Cadmium Sulfide Single Crystals," T. E. Walsh, **J. Opt. Soc. Amer.**
"A Comparison of Two Transistor Models," R. B. Schilling and Coauthor, **IEEE Trans. GED**
"Extension of Unified Design Charts to Inverse Chebychev and Elliptic Filters," N. K. M. Chitre, C. M. Kudsia, and M. V. O'Donovan, **Microwave J.**
"A Fast Data-Acquisition System for a Time-Shared Computer," M. J. Schindler, **IEEE Trans. GMTT**
"Impedance Measurements of Microwave Lumped Elements from 1 to 12 GHz," R. E. DeBrecht, **IEEE Trans. GMTT**
"Semiconductor Surface Contamination Investigated by Radioactive Tracer Techniques," Part 1, W. Kern, **Solid State Tech.**
"Two-Stage Epitaxial Growth of GaAs EI Diodes on Spinel," I. Ladany and C. C. Wang, **J. Appl. Phys.** (Communications)
"Vapor Growth and Properties of ScAs and ScP," W. M. Yim, E. J. Stofko, and R. T. Smith, **J. Appl. Phys.** (Communications)
"Liquid-Crystal Domains in a Longitudinal Electric Field," R. Williams, **J. Chem. Phys.** (1 January)
"Voltage-Induced Tunneling Conduction in Granular Metals at Low Temperatures," P. Sheng and B. Abeles, **Phys. Rev. Letters** (3 January)
"Positive Linear Dispersion in the Velocity of Sound in He II," C. H. Anderson and E. S. Sabisky, **Phys. Rev. Letters** (10 January)
"Toward a Unified Theory of Urbach's Rule and Exponential Absorption Edges," J. D. Dow and D. Redfield, **Phys. Rev. B** (15 January)
"Feedback Current Switch Divides RF Inputs by 20," R. J. Turner, **Electronics** (Designer's Casebook) (January 17)
"Brillouin-Scattering Measurements on Silicon and Germanium," J. R. Sandercock, **Phys. Rev. Letters** (24 January)

February

"The Accuracy of Vehicle Location by Trilateration in a Dense Urban Environment," H. Staras and S. N. Honickman, **IEEE Trans. GVT**
"Antiparallel Operation of Multiple High-Efficiency Avalanche Diodes," H. Kawamoto, **IEEE J. Solid-State Circuits**
"An IC for AM Radio Applications," L. Baar, **IEEE Trans. GBTR**
"Large-Optical-Cavity (AlGa)As-GaAs Heterojunction Laser Diode: Threshold and Efficiency," H. Kressel, H. F. Lockwood, and F. Z. Hawrylo, **J. Appl. Phys.**
"The Measurement of Loudness," H. F. Olson, **Audio**

"A Method for Evaluation of Subsystem Alternate Designs," P. G. Goodwin, **IEEE Trans. GEM**

"Microphone Thermal Agitation Noise," H. F. Olson, **J. Acous. Soc. Amer.** (Part 1)

"Performance Evaluation of the Two-Inch Return-Beam Vidicon Three-Camera Subsystem," B. P. Miller, G. A. Beck, and J. M. Barletta, **J. SMPTE**

"Semiconductor Surface Contamination Investigated by Radioactive Tracer Techniques," Part 2, W. Kern, **Solid State Tech.**

"Study of He-Se Laser Performance," K. G. Hernqvist and D. C. Pultorak, **Rev. Sci. Instr.**

"Transistor Input Parameter Variations Indicating High-Gain Frequency Multiplication Properties," G. D. O'Clock, Jr., **Proc. IEEE** (Letters)

"Y_2O_3:Yb:Er—New Red-Emitting Infrared-Excited Phosphor," J. P. Wittke, I. Ladany, and P. N. Yocom, **J. Appl. Phys.**

"Reinterpretation of Wavelength-Modulated Absorption in $SrTiO_3$ without Coexisting Phases," D. Redfield and W .J. Burke, **Phys. Rev. Letters** (14 February)

"Solid State Imaging Emerges from Charge Transport," M. G. Kovac, W. S. Pike, F. V. Shallcross, and P. K. Weimer, **Electronics** (February 28)

March

"Adaptive Ferroelectric Transformers with Improved Temperature Characteristics," S. S. Perlman and J. H. McCusker, **IEEE Trans. GED** (Correspondence)

"Coupled-Wave Analysis of Holographic Storage in $LiNbO_3$," D. L. Staebler and J. J. Amodei, **J. Appl. Phys.**

"Dependence of Threshold Current Density and Efficiency on Fabry-Perot Cavity Parameters: Single Heterojunction (AlGa)As-GaAs Laser Diodes," M. Ettenberg and H. Kressel, **J. Appl. Phys.**

"Electrical Properties of Carbon-Doped Gallium Phosphide," D. P. Bortfeld, B. J. Curtis, and H. Meier, **J. Appl. Phys.**

"Erase-Mode Recording Characteristics of Photochromic CaF_2, $SrTiO_3$ and $CaTiO_3$ Crystals," R. C. Duncan, Jr. **RCA Review**

"High Contrast, High Sensitivity Cathodochromic Sodalite for Storage and Display Applications," B. W. Faughnan and I. Shidlovsky, **RCA Review**

"Holographic Information Storage," E. G. Ramberg, **RCA Review**

"Holographic Recording in Lithium Niobate," J. J .Amodei and D. L. Staebler, **RCA Review**

"Liquid Crystals for Electro-Optical Applications," J. A. Castellano, **RCA Review**

"Materials for Magneto-Optic Memories," R. W. Cohen and R. S. Mezrich, **RCA Review**

"Measurement of Circularly Polarized Broadcast Antennas," O. Ben-Dov, **IEEE Trans. GBC**

"Optical and Holographic Storage Properties of Transition Metal Doped Lithium Niobate," W. Phillips, J. J. Amodei, and D. L. Staebler, **RCA Review**

"Phase Holograms in Dichromated Gelatin," D. Meyerhofer, **RCA Review**

"Planning and Implementing Effective Engineering Meetings," L. Bulwer, **IEEE Trans. GPC**

"Possible Field-Assisted Infrared Photocathode," V. L. Dalal, **J. Appl. Phys.**

"Recording Considerations for RCA HoloTape," R. A. Bartolini, J. Bordogna, and D. Karlsons, **RCA Review**

"Recyclable Holographic Storage Media," J. Bordogna, S. A. Keneman, and J. J. Amodei, **RCA Review**

"Redundant Holograms," A. H. Firester, E. C. Fox, T. Gayeski, W. J. Hannan, and M. Lurie, **RCA Review**

"Role of Ionization Inhomogeneities in the S-Type Characteristic of Moderately Heavily Doped n-GaAs," P. D. Southgate, **J. Appl. Phys.**

"There is More to Typesetting than Setting Type," J. E. Justus, **IEEE Trans. GPC**

"Thermoplastic Media for Holographic Recording," T. L. Credelle and F. W. Spong, **RCA Review**

"Tunable Frequency Range and Mismatch Adjustment for Comb-Line Bandpass Filters," G. D. O'Clock, Jr., **IEEE Trans. GMTT** (Short Papers)

"Wavelength Dependent Distortion in Fraunhofer Holograms and Applications to RCA HoloTape," R. A. Bartolini, D. Karlsons, and M. Lurie, **RCA Review**

"Magnetic Transitions of Superconducting Thin Films and Foils. III. Pb, Sn, and In," G. D. Cody and R. E. Miller, **Phys. Rev. B** (1 March)

Patents Issued to RCA Inventors First Quarter, 1972

January

R. A. Bartolini and M. J. Lurie Partially Overlapping Hologram Motion Picture Record (3,632,869)
J. R. Burns and J. H. Scott, Jr. Epitaxial Semiconductor Device Having Adherent Bonding Pads (3,636,412)
V. W. Chen and H. Amemiya Operation of Field-Effect Transistor Circuits Having Substantial Distributed Capacitance (3,638,039)
R. Denning Contact System for Semiconductor Devices (3,632,436)
W. F. W. Dietz Triggering Circuit for CRT Deflection System Utilizing an SCR (3,638,067)
W. W. Evans Signal Seeking System for Radio Receivers with Tuning Indicating Circuitry for Controlling the Signal Seeking (3,632,864)
R. E. Flory and F. W. Spong System and Filter for Encoding Color Images Onto Black and White Film (3,637,925)
J. J. Hanak Magnetic Head Method (3,634,933)
J. R. Harford Noise Protected AGC Circuit with Amplitude Control of Flyback Pulses (3,634,620)
W. A. Helbig, Sr. and W. E. Woods Bowling Split Detector (3,637,211)
C. Y. Hsueh Interpulse Time Interval Detection Circuit (3,634,869)
H. B. Law and R. H. Lee Method of Producing a Color Kinescope (3,631,576)
P. A. Levine and S. Liu Compact, High-Power, High-Efficiency Silicon Avalance Diode L-Band Oscillator (3,638,141)
N. L. Lindburg and H. D. Woodland Assembly of Filamentary Display Devices (3,631,593)
G. E. Long, 3rd, D. W. Bartch, and F. D. Grove Lithium Silicate Glare-Reducing Coating and Method of Fabrication on a Glass Surface (3,635,751)
W. J. Maddox and M. R. Weingarten Photographic Process for Preparing a Screen Structure for a Cathode-Ray Tube (3,636,836)
W. L. Oates Hermetic High-Current Terminal for Electronic Devices (3,637,917)
R. L. Pryor Chopper Stabilized Amplifier (3,638,129)
T. Saeki Keyed Substrate Field Effect Transistor Frequency-Selective Circuits (3,637,935)
H. M. Scott and C. R. Corson Vector Generator (3,638,214)
S. A. Steckler Oscillator with Variable Reactive Current Frequency Control (3,636,475)
F. Sterzer Transferred Electron Amplifier with Oscillation Stabilization Circuit (3,636,461)
W. M. Stobbe Identifier Circuits for Color Bar Type Test Generators (3,634,612)
A. I. Stoller and W. H. Schip, Jr. Heat Seal of a Glass Member to Another Member (3,635,510)
J. A. Van Raalte and W. J. Gorkiewicz Color Correction of Prismatic Off-Axis Optical System (3,637,308)
J. J. Yorganjian Signal Detecting and Latching Circuit (3,634,876)
B. Zuk Storage Circuit (3,636,527)

February

R. A. Alleman and W. N. Henry Apparatus for Chemically Etching Surfaces (3,640,792)
J. P. Betz Variable Length Coding Method and Apparatus (3,643,019)
T. V. Bolger Electronic Editing Apparatus (3,646,260)
D. S. Bond Radio Postal System Acknowledgment Apparatus (3,641,432)
M. K. Brown Electron Beam Tube and Method of Adjusting the Electrode Spacing of an Electron Gun Therein (3,643,299)
J. B. Bucher Apparatus for Measuring Light Transmission of a Semitransparent Membrane (3,645,634)
W. R. Chiodi Toroidal Electromagnetic Deflection Yoke (3,643,192)
A. G. F. Dingwall Ratio-Compensated Resistors for Integrated Circuit (3,644,802)
R. D. DiStefano and E. A. James Selective Deposition of Metal (3,640,765)
W. V. Fitzgerald, Jr. High Frequency Semiconductor Device (3,641,398)
T. P. Fulton and H. Di Luca Encapsulated Magnetic Memory Element (3,640,767)
E. B. Gamble Logic Gate (3,641,362)
E. B. Gamble and R. H. Aires Logic Circuit which Turns On and Off Rapidly (3,641,368)
S. A. Graf Amplifier Using Bipolar and Field-Effect Transistors (3,644,838)
D. L. Greenaway and J. P. Russell Holographic Identification System (3,643,216)
K. G. Hernqvist Ion Discharge Tube Employing Cataphoretic Techniques (3,639,804)
N. Hovagimyan and R. N. Van Delft Solid-State Analog Cross-Point Matrix Having Bilateral Crosspoints (3,639,908)
K. Katagi Synchronization of Serial Memory (3,643,220)
H. C. Lee Integrated Buffer Circuits for Coupling Low-Output Impedance Driver to High-Input Impedance Load (3,639,787)
A. L. Limberg Sample-and-Hold Circuit (3,646,362)
A. L. Limberg and S. A. Steckler Protection Circuit (3,641,361)
A. Macovsky Non-Interacting Lens System for a Color Encoding Camera (3,641,255)
N. T. Mirkovic Brake Apparatus (3,638,881)
P. K. Mrozek Temperature Compensated Crystal Oscillator (3,641,461)
R. C. Owens Semiconductor Mounting Structure (3,641,474)
B. S. Perlman and T. E. Walsh Transferred Electron Amplifier (3,644,839)
R. J. Ryan Adhesion of Nonconducting and Conducting Materials (3,640,853)
R. S. Silver and E. Luedicke Image Storage System (3,646,590)
S. A. Steckler Sample-and-Hold Circuit (3,641,258)
S. A. Steckler Transistor Signal Translating Stage (3,641,448)
N. R. Stewart and D. R. Preslar Pulse-Type Circuit Element-Testing Method (3,643,156)
J. L. Vossen, Jr. Method of Metalizing Semiconductor Devices (3,640,811)
J. L. Vossen, Jr. and J. H. Ranfield Method of Making Electrical Contacts on the Surface of a Semiconductor Device (3,640,812)
C. P. Wen Gyromagnetic Isolator Wherein Even Mode Components are Converted to Odd Mode Components by Biased Ferrite (3,646,486)
D. J. Woywood Beam Control System (3,646,568)

March

J. J. Amodei Information Storage System Employing Optical Entry and Removal of Information (3,651,488)
G. E. Anderson Kinescope Bias Arrangement to Provide Both Constant Amplitude D.C. Restoration Pulses and Arc Discharge Protection (3,647,944)
H. Ball and H. L. Peterson Automatic Beam Focusing System (3,647,952)
D. M. Baugher and E. T. Hausman Multi-Circuit Hybrid Module and Method for Making (3,648,116)
H. R. Beelitz Gated Amplifier (3,651,421)
E. J. Boleky, III and J. R. Burns Fabrication of Semiconductor Devices (3,646,666)
R. J. Butler Color Phaser for Television Video Signals (3,647,965)
L. J. Byers and J. M. Keeth Dual Loop Receiver Tuning and Frequency Tracking System (3,652,938)
D. J. Carlson Electronically Tuned Ultra High Frequency Television Tuner (3,649,937)
K. K. N. Chang and H. J. Prager High Power Semiconductor Device Assembly (3,649,881)
A. G. F. Dingwall Apparatus for Increasing the Speed of Series Connected Transistors (3,651,342)

R. A. Dischert Television Camera Utilizing a Parellel Striped Color Encoding Filter (3,651,250)
J. B. George and S. E. Hilliker Electronically Tuned Ultra High Frequency Television Tuner with Frequency Tracking Tunable Resonant Circuits (3,651,409)
H. J. Gerritsen and W. J. Hanan Redundant, Speckle-Free Hologram Recording Apparatus (3,650,595)
J. J. Gibson Apparatus Permitting Reliable Selection of Transmitted Television Message Information (3,649,749)
J. J. Gibson Control Signal Generating Apparatus to Permit Reliable Selection of Transmitted Television Message Information (3,649,750)
S. A. Graf Reference Voltage Source (3,648,153)
W. J. Hannan Color Encoding System Utilizing Two Filters Alternately for Minimizing Effects of Misregistration and Image Pickup Device Lag (3,647,945)
L. A. Harwood Control System (3,647,940)
F. Z. Hawrylo Double Epitaxial Solution Regrowth Process and Device Made Thereby (3,649,382)
F. P. Heiman Method of Making High Area-Density Array Photomasks Having Matching Registry (3,647,438)
G. H. Heilmeier and J. E. Goldmacher Liquid Crystal Light Valve Containing a Mixture of Nematic and Cholesteric Materials in Which the Light Scattering Effect is Reduced when an Electric Field is Applied (3,650,603)
D. C. Herrmann and L. J. Bazin Feedback Clipper (3,651,339)
E. Hutto, Jr. and J. P. Mahoney Bowling Pin Detector (3,651,328)
D. W. Janz Peak Demodulator (3,651,419)
L. B. Juroff and L. M. Lunn Remote Controlled Television Tuner Motor Switching Circuit (3,648,135)
J. P. Keller and S. A. Graf AC Line Operation of Monolithic Circuit (3,649,887)
R. I. Klein and S. Caplan Liquid Crystal Display Device (3,647,280)
I. Ladany Liquid Phase Double Epitaxial Process for Manufacturing Light Emitting Gallium Phosphide Devices (3,647,579)
A. L. Limberg Electrical Circuit Providing Multiple V_{B_e} Bias Voltages (3,651,346)
A. L. Limberg Signal Translating Stage Providing Direct Voltage Translation Independent of Supplied Operating Potential (3,651,347)
A. L. Limberg Electrically Controlled Attenuation and Phase Shift Circuitry (3,649,847)
H. Notarius Dark Fosterite Ceramic Composition (3,649,309)
D. W. Peterson Combined VHF-UHF Dipole Antenna Array (3,653,056)
D. R. Purdy and W. E. Donnelly Fluid Cooled Apparatus for Testing Power Semiconductor Devices (3,648,167)
E. C. Ross Voltage Translation Circuit for MNOS Memory Array (3,649,848)
W. W. Siekanowicz Microwave Limiter that Suppresses Leading Edge Spike of Radio Frequency Signal (3,648,197)
B. K. Smith Process for Coating Flatlike Surfaces (3,652,323)
R. K. Waltner High Voltage Hold-Down Circuit (3,649,901)
J. P. Watson Multi-Electronic Transducer Element (3,648,279)
C. P. Wen Symmetrical Trough Waveguide Antenna Array (3,653,054)
E. J. Wittmann Synchronous Detector Control (3,651,418)

AUTHORS

Jacques M. Assour attended the Technion in Haifa, Israel, in 1955 where he completed two years of studies in the Electrical Engineering Department. In February 1958, he entered the Polytechnic Institute of Brooklyn where he received his degree of Bachelor of Electrical Engineering (cum laude) in 1960. Upon graduation he joined RCA Laboratories in Princeton, New Jersey where he worked on the design and synthesis of antenna radiation patterns. He received his M.S.E.E. degree in 1962 and his Ph.D. degree in electrophysics in 1965 from the Polytechnic Institute of Brooklyn. From 1961 to 1966 he was engaged in the study of crystalline organic semiconductors and specifically in the area of paramagnetic resonance. Since 1966, he has been working in the field of solid-state devices. In particular, he designed and fabricated silicon PIN microwave diodes, ultrafast silicon PIN photodetectors, photosensor arrays for computer applications, and microwave avalanche diodes.

Dr. Assour is a member of the honorary societies Eta Kappa Nu and Tau Beta Pi.

James E. Carnes received the B.S. degree from Pennsylvania State University, University Park, in 1961, and the M.A. and Ph.D. degrees in electrical engineering from Princeton University, Princeton, N. J., in 1967 and 1970, respectively. His Ph.D. dissertation was an investigation on photo-induced currents and charge transport in polyvinylcarbazole, an organic polymer. He was in the U. S. Navy from 1961 to 1965. During the summers of 1966 and 1967 he investigated metallic contacts and dc electroluminescence in strontium titanate at RCA Laboratories, David Sarnoff Research Center, Princeton, N. J., which he joined as a member of the technical staff in 1969. Since that time he has studied electrical breakdown, conduction, and interface properties of various insulating films on silicon and is currently involved in the investigation of charge-coupled devices.

Dr. Carnes is a member of the American Physical Society, Tau Beta Pi, Phi Kappa Phi, and IEEE.

Robert B. Comizzoli received a B.S. in Physics summa cum laude from Boston College in 1962. He attended Princeton University from 1962 to 1966, receiving the Ph.D. in Physics in 1967. His thesis work involved polarization effects in photoconductors. Since 1966, he has been at RCA Laboratories, Princeton, New Jersey. His research experience includes thermal neutron interactions with polarized nuclei, photoconductivity and transport in II-VI compounds, and electrophotography. He has studied the electrical and photoconductive properties of inorganic and organic electrophotographic materials, including dye-sensitization, and has developed new techniques for the investigation of charge distributions in electrophotographic layers. Presently he is engaged in reliability physics studies on silicon devices.

I. P. Csorba graduated from the Electrical Engineering Fundamentals at the Electrical Engineering Faculty of the Technical University of Budapest in 1952. In the same year he was admitted to the Communication Engineering Faculty, specializing in communication and electronics. In October, 1954, he received the Diplom Ingenieur Degree in Electrical and Communication Engineering. From 1955 to 1956 he worked as a research engineer at the War Technical Institute, Budapest. In December of 1956 he joined the research group of Rauland Corporation, Chicago, where he worked on electrostatic-type image converter tubes, television picture tubes, scan-converter tubes. From 1959 to 1961 he was with Motorola, Inc., Chicago, working primarily on electrostatic-type scan magnification. In November of 1961, he joined RCA as a member of the Photo and Image Tube Engineering Activity. Mr. Csorba has been active in the design and development of magnetic and electrostatic-type image tubes and recently has been engaged in product development work on high-speed light-shutter image tubes.

Norman Goldsmith received the B.A. degree with honors in Chemistry from Hunter College in 1959 and M.S. degree in Physical Chemistry from Stevens Institute of Technology in 1964. He joined RCA in 1959 working in the Solid-State Division at Somerville, N. J., on materials and process technology for silicon and gallium arsenide. His work in this capacity included epitaxial-growth materials purification, diffusion, vapor deposition, surface stabilization, clean oxide growth and the development of nondestructive measurement techniques. From 1967 to 1971 he was with Laser Diode Laboratories as executive vice president. He joined RCA Laboratories in 1971 where he is currently concerned with epitaxial growth studies for silicon power devices.

Mr. Goldsmith is a member of the American Chemical Society and the Electrochemical Society.

Eric F. Hockings received the B.Sc. in Chemistry from the University of London, England, in 1950. He served in the Army and then joined the research laboratories of the Electric and Musical Industries, Hayes, England. After working on photoemitting and photoconducting materials for two years, he entered Imperial College, London, and received the Ph.D. in Chemistry in 1957. Since that time, he has been with RCA Laboratories. Dr. Hockings has carried out research on thermoelectric semiconductors and on magnetic materials for recording media. Currently he is head of Glass and Organic Materials Research.

Walter F. Kosonocky received the B.S. and M.S. degrees in electrical engineering from Newark College of Engineering, Newark, N. J., in 1955 and 1957, respectively, and the Sc.D. degree in engineering from Columbia University, New York, N. Y. in 1965. Since June 1955 he has been employed at RCA Laboratories, Princeton, N. J., where he has conducted research on application of new phenomena and new devices for information processing systems. This work has included ferrite memory systems, parametric digital devices, tunnel-diode circuits, tunnel-dioce and transistor circuits, pattern-recognition systems, applications of lasers for digital systems (including a study of saturable absorbers for Q-switched lasers and semiconductor laser digital devices), optical hologram memory systems and page composition, optically controlled p-MOS circuits, and a liquid-crystal image converter. Presently he is working on the development and applications of charge-coupled devices.

Dr. Kosonocky is a member of Sigma Xi, Tau Beta Pi, Eta Kappa Nu, and a senior member of IEEE.

Gerald S. Lozier received the B.S., M.S., and Ph.D. degrees in chemistry from Western Reserve University, Cleveland, Ohio, in 1952, 1953, and 1956, respectively. From 1955 to 1959 he was a Member of the Technical Staff at RCA Laboratories, Princeton, N. J., where he did basic research on high-energy density batteries. In 1959 he transferred to the RCA Solid-State Division, first as a Group Leader and then as a Manager on the development of magnesium primary cells. In 1963 he joined the Thermoelectric Device Department of RCA, Harrison, N. J., where he developed novel bonding techniques for Si-Ge and InAs-GaAs thermoelectric devices. From 1966 to 1967 he was Manager of the Materials Research in the Thermoelectric Device Department. In 1967 he returned to RCA Laboratories, where he was engaged in basic research on liquid toners for electrophotography and electrode phenomena in liquid crystals. His present research is concerned with electroless plating.

Dr. Lozier is a fellow of the American Institute of Chemists and is a member of the American Chemical Society and the Electrochemical Society. He was co-recipient of an RCA Laboratories Achievement Award in 1957 for new battery systems.

L. J. Nicastro received the BA in Physics from La Salle College in 1953, the MS in Radiation Biology from the University of Rochester in 1956, and the Ph.D. in Physics from Temple University in 1970. Dr. Nicastro was an instructor in Chemistry and Physics at La Salle College, 1953-1954; a Physicist in Ballistics at the Frankford Arsenal, 1954-1955; and a Health Physicist at the Brookhaven National Laboratories during the summer of 1956. From 1956 to 1959, he worked in the Neutron Physics Section of the National Bureau of Standards on neutron spectrometry, measurements of neutron age, and the response of various scintillators to alpha particles. Since coming to RCA early in 1959, Dr. Nicastro has done experimental work in the areas of gaseous molecular frequency standards, laser radar, and measurement of plasma properties using lasers. Dr. Nicastro has been involved in experimental and analytical studies in the general area of display techniques, including modulation of light by means of magneto-optic rotators and electro-optic crystals, laser displays, and measurements of the negative resistance effect in cadmium selenide powders. Recently, Dr. Nicastro has been engaged in work on the development of liquid-crystal displays.

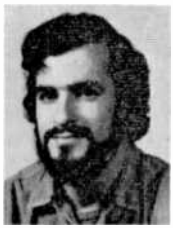

Peter E. Norris received his B.S. in electrical engineering from MIT in 1965. From 1965 to 1967 he attended graduate school at MIT and received both the M.S. and Engineer's degrees in 1967. During this period he was a member of the Laboratory for Insulation Research, working in the area of high resistivity semiconductors. In 1967 he attended the University of Colorado. He joined RCA Laboratories in 1968, working initially on large-screen television displays, photochromics, and radiation damage in MOS devices. Mr. Norris is currently with the Solid State Device Technology Group engaged in research on improved insulators for IC technology, and radiation resistant MOS integrated circuits. At present he is engaged in research on silicon aluminum oxide MIS devices and their associated technology. A joint effort with Dr. Karl Zaininger and Dr. K. Schlesier, also of RCA Laboratories, has recently established that this technology can result in a significant hardening of MOS devices in a radiation environment.

Elmer L. Offenbacher is Professor of Physics at Temple University in Philadelphia, Pa. He joined the Temple faculty after completing work for his Ph.D., at the University of Pennsylvania in 1951, on the Theory of the Directional Effects of Electric Breakdown in Ionic Crystals. He also taught an extension course in Solid State Physics at RCA in Camden, N. J. He has supervised a number of ph.D. theses from engineers at various RCA installations. He has worked in the field of Electron Spin Resonance and most recently on mechanical properties of single crystals of ice.

Jacques I. Pankove obtained his B.S. (1944) and M.S. (1948) degrees from the University of California. He received his doctorate from the University of Paris in 1960 for a study of infrared radiation and germanium. Since 1948, when he joined RCA Laboratories, he has made many contributions to the understanding, technology, and evolution of various semiconductor devices, including large-area photocells and transistors. He has worked in the field of superconductivity, studies of silicon carbide, and investigations of the optical properties of degenerate germanium and the electrical properties of tunnel diodes in germanium, as well as in superconductors and in thin oxide layers. Currently, he is concerned with the study of injection luminescence and laser action in gallium arsenic and other compounds.

James F. Reynolds received his B.E.E., M.E.E., and Ph.D. from Rensselaer Polytechnic Institute in 1964, 1965, and 1967, respectively. His doctoral thesis investigated methods of stabilizing gaseous magneto-plasmas by controlling the magnetic field geometry. His earlier graduate research was concerned with the use of microwave techniques for plasma diagnostics. Since joining the RCA Microwave Technology Center in 1967, Dr. Reynolds has been engaged in work on silicon and GaAs active microwave devices. In 1968, he received an RCA Laboratories Achievement Award for his research on transferred electron oscillators. His recent work has been concerned with the development of Trapatt diode sources for military and commercial systems. This work has included device, rf circuit, and pulse modulator development.

Dr. Reynolds is a member of Tau Beta Pi, Eta Kappa Nu, and an associate member of Sigma Xi.

John W. Robinson was graduated from Trenton Catholic Boy's High School and served in the U. S. Navy from 1949 to 1953. While in the Navy he became an Aviation Electronics Technician. Since 1965 he has periodically taught electronics for the U. S. Army at the Fort Dix Education Center. Mr. Robinson joined RCA Laboratories, Princeton, New Jersey, in 1954. Since that time he has worked on the crystal growth of elemental and compound semiconductors, the preparation of silicon-germanium alloys for thermoelectric applications, and the vapor phase growth and zone refining of various inter-metallic compounds. His recent work has been concerned with the preparation of chromium dioxide, and at present he is working on the preparation of other fine magnetic powders for recording applications.

Arye Rosen received the B.S.E.E. degree from Howard University in 1963, and the M.Sc.E. degree from Johns Hopkins University in 1965. He was an instructor at Johns Hopkins during the year 1963-64, and presently is enrolled in a Ph.D. program at Jefferson University. From 1964 to 1967, Mr. Rosen was concerned with systems design at General Telephone and Electronics International, and with antenna and circuit design at Channel Master, Inc., and American Electronic Laboratories, Inc. In 1967, Mr. Rosen joined the RCA Microwave Technology Center in Princeton, N. J., where he is presently engaged in the study and development of microwave circuits for solid-state microwave oscillators and amplifiers, including varactor multipliers, transistors, and Trapatt devices.

Mr. Rosen is a member of Tau Beta Pi, Sigma Xi, and the Association of Professional Engineers of British Columbia.

Donald A. Ross received the B.Eng. degree in electrical engineering from McGill University, Montreal, Que., Canada, in 1947, and both the M.Sc. and Ph.D. degrees in physics from Yale University, New Haven, Conn., in 1953 and 1957, respectively. Prior to attending Yale University he worked for the General Electric X-Ray Corporation where he did work on medical and industrial x-ray problems, and also for the High Voltage Engineering Corporation where he did work on the effects of radiation from Van de Graaff accelerators. He joined RCA Laboratories in 1958 when he was responsible for research with a 5-MW nuclear reactor. Since 1964 he has been responsible for electronic printing research concerned with novel methods for copying and printing by electrostatic or other electronic means.

Richard A. Sunshine received the B.S. degree (with Honor) in Physics from Stevens Institute of Technology in 1964, the M.A. degree from Princeton University in 1967, and the Ph.D. degree in Solid State Device Physics from Princeton University in January 1971. In 1964 he joined RCA Laboratories where he investigated ionic motion in thermally grown silicon-dioxide films. He received an RCA Laboratories Graduate Study Award for part-time study of Physics at Rutgers University from 1964-1966, and a Doctoral Study Award for full time study of Device Physics at Princeton in 1967. His Doctoral dissertation was primarily concerned with the development of new optical techniques for studying failure mechanisms in semiconductor devices, and the application of these techniques to the study of second breakdown in avalanching silicon-on-sapphire diodes. In addition, he has done theoretical work on Gunn domains, and on space-charge effects in avalanching junctions.

Dr. Sunshine is a member of Tau Beta Pi.